A study of magnetospheric boundary layers by Cluster

Ellen Osmundsen

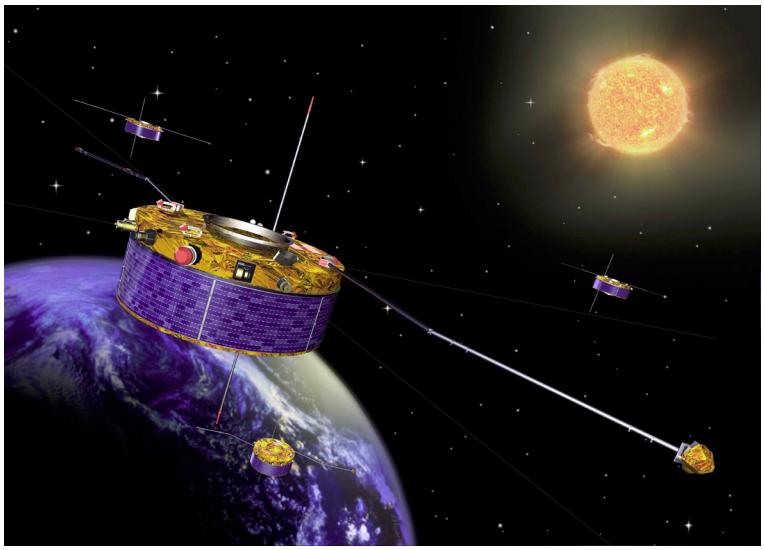

Thesis submitted for the degree of Candidata Scientarium
Department of Physics,
University of Oslo
May 2005

Picture on cover:
Artistic impression of the four Cluster satellites.
Taken from the ESA-Cluster web-page [2003]

Abstract

In this thesis, the spacecraft potential measured by the EFW instrument on Cluster has been used to map the plasma density distribution of the magnetosphere. A relation between the spacecraft potential and the plasma density has been established and three years of data have been binned to obtain a 3D image of the density distribution. Boundaries like the bow shock, the magnetopause, the plasmapause and the plasma sheet boundary layer (PSBL) are identifiable in this image.

The identification of the PSBL has been used to determine plasma sheet thicknesses. By assuming that the plasma sheet is symmetric about the neutral sheet and that the sheet position is known, the half thickness has been estimated for each PSBL crossing. A simplified method based on the dipole tilt angle has been used to determine the neutral sheet position relative to the GSM x-axis. On average the plasma sheet half thickness was found to be $4.73R_E$. There is, however a large spread in the data as the plasma sheet half thickness can take any values from $0R_E$ to $12R_E$.

A statistical comparison of IMF Bz and the plasma sheet thickness has given a positive correlation of about 0.5 which indicates a trend as expected. However, the poor correlation against parameters like solar wind pressure and the energy input (epsilon-parameter), and the large spread in data, may indicate that internal processes of the magnetosphere may govern the tail dynamics/reconnection. More work is needed to make this conclusive.

Acknowledgements

Time has come to thank everyone that have been important in helping me complete this work and the list of people that deserves attention is long.

First of all I want to thank my supervisors Arne Pedersen, Jøran Moen and Bjørn Lybekk for helping me through this thesis. Arne Pedersen with his long experience is like a never-ending well of knowledge about the Cluster satellites, their instrumentation and data analysis. Thank you for all discussions and valuable advises. Jøran Moen have been very important to me during the writing of this thesis, correcting my misunderstandings and providing good advices on improvements. Thanks for your support and encouragement. I also want to thank Bjørn Lybekk for all help with data acquisition and data handling.

Two other persons that have given me a lot of help, support and inspiration are Kjellmar Oksavik and Nicolai Østgaard. Thanks to Kjellmar for helping me getting started with my MatLab programming and for having supported and encouraged me all the way. Nicolai have been a source of inspirations and given me many good advises and ideas along the path.

A great thanks to Espen Trondsen for all computer help. Always helpful and always smiling. I believe the computers have a great respect for you because each time you just sat down in front of one it started working again.

Gaute Birkeli has also helped me a lot during the final stage of writing. Thanks for reading through and commenting my thesis. I also appreciated the many times you picked me up at the university late at night making sure I got home and had enough sleep to be able to continue working the next day.

Margit Dyrland have been a very good friend and I want to thank you for moral support and encouraging talks, serious discussions and social disturbances.

And not to forget all the students, both earlier and present and all the employees at the research group. Thank you all for discussions and support of both social and professional character. I also want to say thanks to my family and friend who have been very patient and supportive especially during the last two months when I have spent most of my time working with this thesis.

Data for this thesis are mostly collected at the Coordinated Data Analysis web (CDA-web) and through the Cluster Science Data System web-page. Thanks to the prime investigators on the Cluster instruments and CDA-web for providing data from the respective instruments on-board the Cluster satellites. Solar wind data have been collected form the ACE-web-page. Thanks to the ACE SWEPAM and MAG instrument teams and the ACE Science Center for providing the ACE data. Geomagnetic activity indexes have been found at the Kyoto World Data Centre for geomagnetism (WDC).

Ellen Osmundsen, May 2005

Contents

Chapter 1

Introduction

In the early ages, when people saw the aurora in the night sky they might have started wondering what it was and where it came from. They did not have instruments nor knowledge to do any closer studies of the phenomena and the human fantasy gave rise to many myths and stories about the aurora. But the human search for the truth has never ended.

The idea of a coupling between the aurora, the Earth's magnetic field, and the Sun was born only 130 year ago. During these years a lot of instruments have been developed to better understand how the Sun interacts with the Earth. Today it is considered a fact that solar particles enter the Earth's magnetic field and are guided down to the atmosphere, creating auroras. The effects from these solar particles as seen on the Earth, have been thoroughly investigated by ground based instruments. From the beginning of the nineteenth century a large network of geomagnetic observatories have made continuos measurements of the Earth's magnetic field. Later, optical instruments and radars have been used extensively in the auroral research.

From measurements made on the Earth, scientists could only study the processes in the magnetosphere indirectly. They needed direct in-situ measurements to better understand the complex processes leading to the beautiful auroras. This was first possible when the first satellite was launched, by the Russians in 1957. Since then, a large number of satellites have been investigating the near Earth environment and also visited the distant magnetic tail.

When scientists in general want to test their theories they make a controlled experiment. Space physicists do not have this opportunity since the system that is subject to a study is influenced by the Sun which can not be controlled. The only possibility is to find measurements that are taken when certain conditions are present. In addition the Earth magnetic field is so large that it is almost impossible to have a simultaneous measurement of the whole system. The result is that many studies focus on explaining just small parts of a process or a phenomena, giving rise to many theories that may contradict eachother.

One task that have caught interest among space scientists for a long time is to develop a theory for how the solar wind affects the Earth's magnetic field also called the magnetosphere. A way to better understand this coupling is to study the movement of magnetospheric boundaries. The boundaries can be recognized by the variations in particle density and energy on each side of the boundary. By using satellite measurements the position of these boundaries relative to the Earth can be found.

In the year 2000, the European Space Agency (ESA) launched four satellites to investigate the Earth's magnetic environment and study the relation between the Sun and the magnetosphere. These four satellites are named Cluster since they orbit together around the Earth and operate as a cluster of satellites. In this thesis particle measurements from Cluster will be used to identify boundaries and to study some of their features.

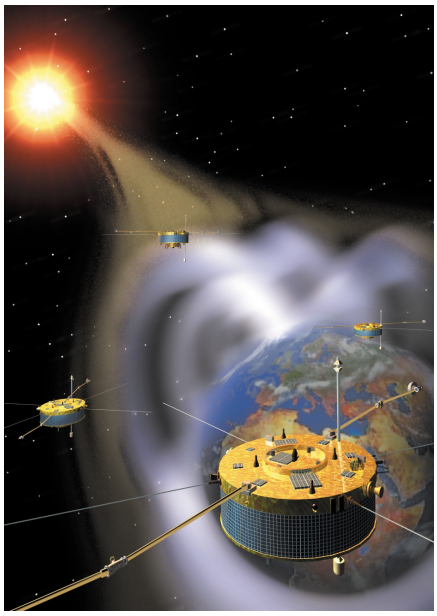

Figur 1.1: *The four Cluster satellites investigating the Sun-Earth interaction. From [Spaceflight Now, 2005]*

First, the Cluster data will be used to find a statistical density distribution in the magnetosphere. From this study many of the magnetospheric boundaries can be recognized. From this statistical overview a method for identifying the boundary between the plasma sheet and the lobe will be established. The method makes use of the differences in the plasma density in the two different regions. This together with the development of a useful coordinate system will then be used to find the thickness of the plasma sheet. Finally solar wind conditions will be compared with the plasma sheet thickness in order to find direct or indirect connections.

Chapter 2

Space physics

2. 1. General plasma physics

2. 1.1. Plasma definition

A plasma is defined as "*a quasineutral gas of charged and neutral particles which exhibits collective behavior*" [Chen,1984]. "Quasineutral" means that the net charge is almost zero but there are still electromagnetic forces acting on individual particles. Particles in the plasma tend to move together influenced by the same magnetic forces, they exhibit "collective behavior". Plasma can be described both in terms of fluid theory and single particle motion. In this thesis the fluid description will be used.

Only 2% of the Earth's atmosphere is ionized, but still 99% of the known matter in the universe is believed to be in a plasma state. The degree of ionization in a gas is related to the gas temperature through the Saha equation [Chen,1984]. The temperature on Earth is not high enough for plasma to exist. If a neutral gas is heated the temperature and number of ionized particles will increase. The gas is said to reach a fourth state of matter, plasma [Chen, 1984]. With a high degree of ionization, a plasma generally have a very high conductivity. In highly conductive plasma the resistivity is low and the ionized particles can move freely around without colliding. It is the magnetic field that control the collective behavior of collisionless plasma.

2. 1.2. Frozen in flux

Plasma in space can be described by ideal magnetohydrodynamic (MHD) theory were the conductivity is assumed to be infinite. ohm's law for a plasma is given as

$$\vec{J} = \sigma(\vec{E} + \vec{v} \times \vec{B}) \qquad (2.1)$$

where $\vec{J}$ is the current density, σ is the conductivity, $\vec{E}$ is the electric field, $\vec{B}$ is the magnetic field and $\vec{v}$ is the plasma velocity. In the case of super conductive plasma, the term $\vec{E} + \vec{v} \times \vec{B}$ in Equation 2.1 has to be zero in order to get a finite current. This results in a drift velocity, v_E given by

$$\vec{v_E} = \frac{\vec{E} \times \vec{B}}{B^2}. \qquad (2.2)$$

Plasma will convect with this drift velocity as long as ideal MHD is valid.

When ideal MHD is valid it can be shown that the net flux through a surface will not change even if the surface change location and shape [Pécseli, 2001]. This means that a magnetic field line can move along with the surrounding plasma and can be recognized

by the plasma it is frozen into. Taking the curl on each side of ohm's law (Equation 2.1) gives

$$\frac{1}{\sigma}\nabla\times\vec{J} = \nabla\times\vec{E} + \nabla\times(\vec{v}\times\vec{B}) \qquad (2.3)$$

In ideal MHD the electric field is assumed to be constant in time since the high conductivity will immediately shortcircut all charge separations in the plasma. This means that there is no current caused by a time varying electric field and the amperes law is reduced to

$$\nabla\times\vec{B} = \mu_o\vec{J} \qquad (2.4)$$

Applying this reduced amperes law and faraday's law, in Equation 2.3 results in

$$-\frac{1}{\sigma\mu_o}\nabla\times(\nabla\times\vec{B}) = -\frac{\partial B}{\partial t} + \nabla\times(\vec{v}\times\vec{B}) \qquad (2.5)$$

where μ_0 is the magnetic permeability. Using that $\nabla\times\vec{B} = \nabla(\nabla\bullet\vec{B}) - \nabla^2\vec{B}$ together with gauss law saying that $\nabla\bullet\vec{B} = 0$ transforms Equation 2.5 into

$$\frac{\partial B}{\partial t} = \nabla\times(\vec{v}\times\vec{B}) + \frac{\nabla^2 B}{\mu_0\sigma} \qquad (2.6)$$

The first term on the right side of Equation 2.6 relates to convection of plasma and field lines with v_E drift. The last term describes a diffusion process and is inversely related to the conductivity of the plasma. This means that under normal conditions when plasma has large conductivity, the convection will be responsible for the particle transport and ideal MHD theory is valid. [Priest,1995]

Reynolds number, R_m, is the ratio between the convection term and the diffusion term and is given as

$$R_m = \mu_0\sigma v L, \qquad (2.7)$$

where L is the characteristic scale length for change in fields and flows in the plasma. A large R_m means that the convection term is greater than the diffusion term and plasma drifts with a speed perpendicular to the electric and magnetic field. A small R_m due to small conductivity or small scale lengths means that ideal MHD breaks down. The diffusion process takes over the particle transport. [Priest,1995]

2. 1.3. Reconnection

During a reconnection the magnetic field lines are no longer frozen to the plasma and the condition for ideal MHD breaks down. Reconnection is a process where antiparallel magnetic field lines couple and reconfigure themselves. Magnetic energy is converted to kinetic energy of particles and bulk flows.

According to Ampere's law, two plasma populations threaded by oppositely directed magnetic fields must be separated by a current sheet (see Equation 2.4). An increase in the current means a thinning of the current sheet leading the two plasma populations closer to eachother. When a local area gets thinner the plasma can no longer stay collisionless, the resistivity rises, and ideal MHD is no longer valid. The current between the two populations can no longer separate the magnetic field lines and the scale length is small enough to create a diffusion area (See Figure 2.1). Magnetic flux convects into the

diffusion area where the field lines annihilates and reconfigure. As the diffusion process starts, the current sheet thickness will increase. The balance between the diffusion rate and the convection of field lines and plasma into the diffusion region will therefore define the current sheet thickness. [Hughes,1995]

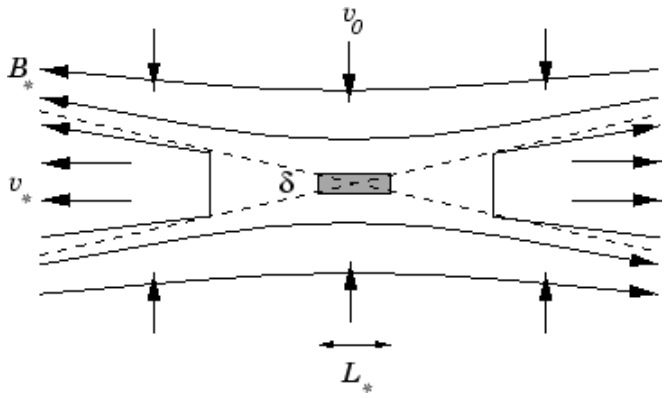

Figur 2.1: *A schematic drawing of a reconnection area made by Richard Fitzpatrick, [2002]*

After a reconnection newly coupled field lines are strongly curved. This gives rise to a strong magnetic tension force which is transferred into kinetic particle energy and causing high speed jets of particles away from the reconnection area.

2. 2. The Sun

In the Sun's core the high temperature makes it possible for the fusion processes to occur. Two hydrogen atoms merge and form a helium atom. The mass of the newly formed helium atom is less than the mass of the two hydrogen atoms and the remaining mass is transformed into energy. The energy released in the core is radiated out towards the surface by photons. Photons do not travel far before being absorbed and re-emitted and the energy is transported by random walk through the radiative zone. Going further out from the core, the temperature drops with an increasing gradient. At a point the temperature becomes so low that the radiation process is no longer efficient to transport energy and convection takes over. A convection process needs a high temperature gradient in order to be efficient and can therefore not take place in the radiative zone. In the convection zone heated plasma rises up towards the photosphere. As it reach regions with lower temperature it cools off and "falls" down again. Convection is the main process for transporting energy out from the radiative zone up to the photosphere. The different zones are shown in Figure 2.2.

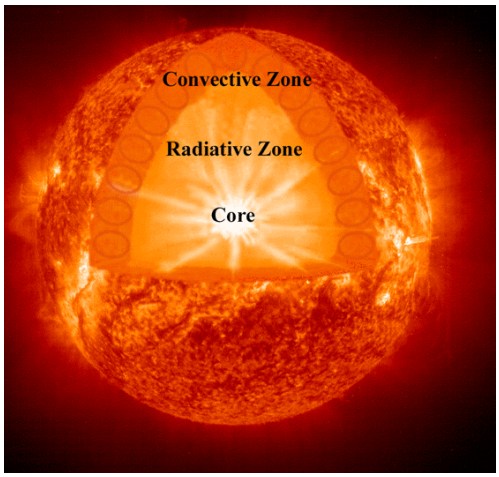

Figur 2.2: *A cut through the Sun showing the tree major zones of the Sun's interior. Picture of the Sun is taken from SOHO -EIT 340. [SOHO web-page]*

The photosphere is located outside the convection zone. The characteristic temperature in this region causes atoms to emit light in the visible part of the spectrum. Outside this sphere is the chromosphere and the corona. Moving outward from the chromosphere, a radical drop in the gas density is observed and at the same time the temperature rises to more than 10^6 K. Despite the high temperature, the low particle density results in a very low total energy density in this area.

2. 2.1. The Sun's magnetic field

The Sun's magnetic field starts out as a dipole like field with two poles. Every 22 year the Sun's magnetic field switches polarity. In addition a differential drift velocity of the plasma in the Sun's surface causes the magnetic field to wrap around the Sun. During the 11 year solar cycle the magnetic wrapping reaches a maximum after 5-6 years and return to a minimum at the end of the period.

As the magnetic field is twisted, the convection in the photosphere causes disturbances and tangles in the concentrated magnetic field. Areas with high magnetic disturbances can make magnetic loops break through the photosphere up to the corona. Hot plasma is accelerated along the field lines and leave a cooler area in the photosphere. These cooler areas are recognized as sunspots. The number of sunspots reaches a maximum at the same time as the magnetic field is most wrapped. [Freedmann, 2001]

The magnetic field lines going out from the Sun and back towards the Sun are separated by a heliospheric current sheet, HCS. Since the magnetic axis of the Sun is not perpendicular to the ecliptic, the current sheet will flip over and under the ecliptic as the Sun rotates [Smith, 2001]. This wavy configuration is carried out in space by the solar wind (described below). The rotation of the Sun also causes the magnetic field lines directed out in space, to form a spiral. This was first proposed by Parker [1958] and is now known as the Parker spiral. The Parker spiral makes the wavy current sheet that rotates around the Sun look like a ballerina skirt as illustrated in Figure 2.3. As seen in

the upper illustration in Figure 2.3 the Earth encounter different orientation of the solar magnetic field.

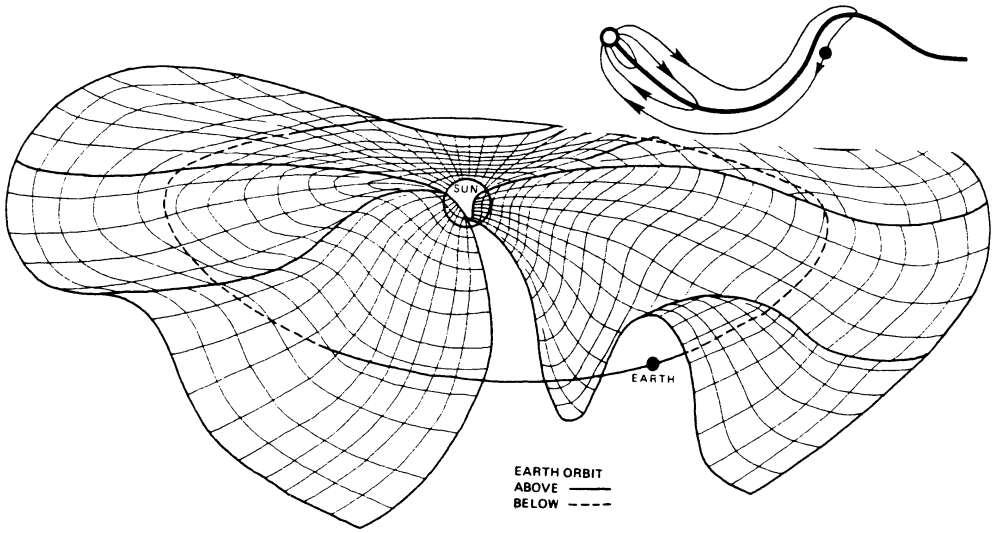

Figur 2.3: *The ballerina skirt of the Sun. As the dipole axis is not aligned with the rotation axis, the current sheet will wobble. In addition the Parker spiral makes it rotate like a skirt changing the magnetic field direction seen from Earth. [Brekke, 1997].*

2. 2.2. The solar wind

The corona is the outermost layer of the Sun and is considered to be the source of the solar wind. Photos taken of the Sun at different wavelengths reveal bright magnetic loops and darker spots. The loops indicate ionized gas flowing along magnetic field lines. Darker areas correspond to coronal holes and scientists believe these are magnetic field lines expanding out in space instead of going in loops [Zeilik and Gregory, 1998]. Hot gases are trapped inside the loops but can escape from the corona holes (see Figure 2.4).

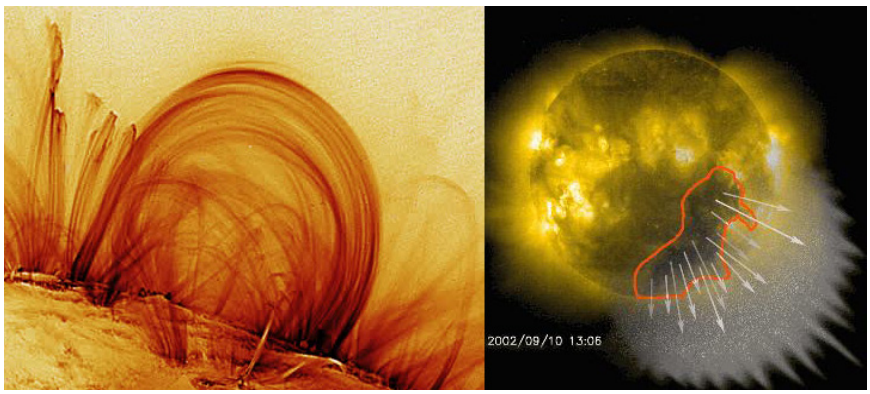

Figur 2.4: *Particles moving along a magnetic loop with closed field lines are trapped in the corona (left). Particles with high enough energy are free to escape in a coronal hole with "open" magnetic flux lines (right). Left: [Lang, 2003], Right [SOHO: pick of the week,2002]*

Because of the high temperature in the corona, the expanding gas has large kinetic energy and the Sun's gravitational attraction is insufficient to hold it back. This relatively calm and continuos particle flow makes up the solar wind and consists mostly of electrons, protons and alpha particles. When the solar wind reaches the Earth it has an average speed at around 400 km/s and the density is about 1-10 cm^{-3}.

Plasma in the solar wind is "frozen" to the magnetic field lines, bringing the solar magnetic field out in space. The magnetic field transported by the solar wind is called the interplanetary magnetic field (IMF).

2. 2.3. Magnetic clouds

In contrast to the steady, continuos solar wind the Sun also has some large violent eruptions. During active periods, flares and coronal mass ejections (CMEs) can occur at the Sun.

A flare is an explosive eruption on the Sun resulting in release of a large amount of energy and particles. In addition to high energy particles, increased electromagnetic radiation with a broad wavelength spectrum is observed. Flares are often connected to active areas on the Sun, i.e. sunspot groups containing high magnetic field intensity. The magnetic field in these areas can store energy by being twisted and compressed. A magnetic disturbance could release this energy and result in a solar flare. Scientists are not sure about the cause of solar flares, but it is agreement that a reconnection process is involved. Magnetic loops are stretched and pinched off by reconnection as shown in Figure 2.5. [Carroll,1996]

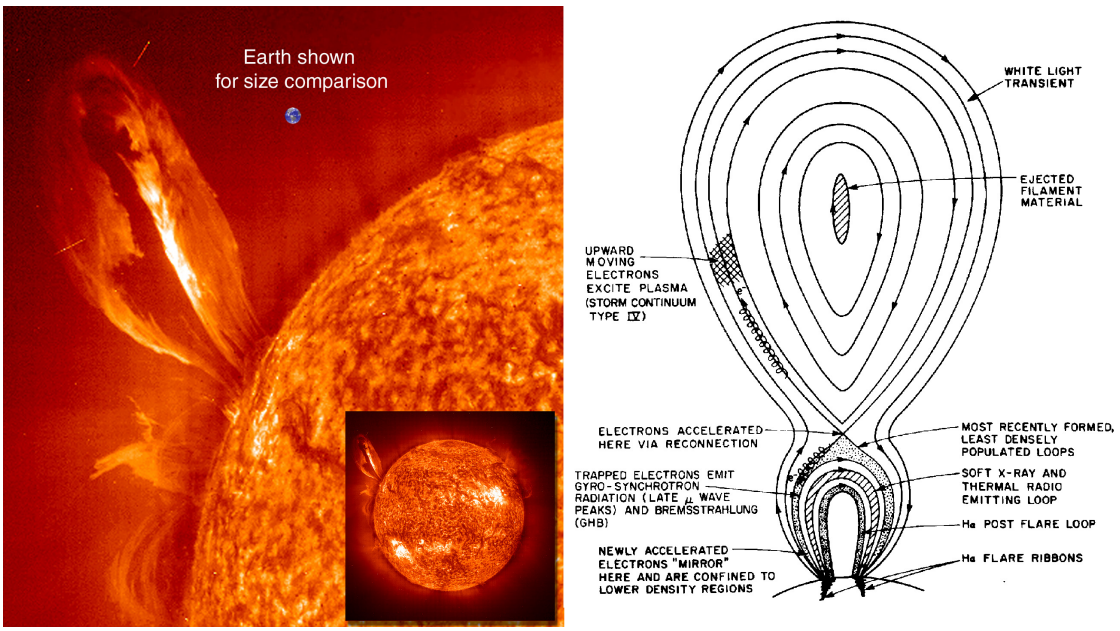

Figur 2.5: *A solar flare erupts on the Sun (right). The schematic configuration leading to a solar flare (left). Taken from (left) SHOHO web-page and (right) [Carroll and Ostlie, 1996]*

Considering the huge amount of energy released by flares they are still just dwarfs compared to a CME. It is not known how the two phenomena relate but it has been

observed a connection between the fastest moving CMEs and flares. It is believed that CMEs form in a similar way as flares. They seem, however, to be formed between different active areas on the surface. These large eruptions are ejected by a reconnection, leaving the Sun with a speed higher than 1000 km/s. As they travel through space, expanding in size, a shock wave is traveling in front. As it hits the Earth, the speed and magnetic field strength have decreased but are still larger than in the steady solar wind. The much denser shock front also exerts a large pressure on the magnetosphere causing disturbances in the Earth magnetic field. [Manchester et al., 2004]

2. 3. The Magnetosphere

The Earth with it's magnetic field stands up like an obstacle in the solar wind, just like a stone in a river. A "wall" is formed where the water hits the stone because the water is slowed down and has to go around the stone. Just behind the stone the water runs very slowly followed by turbulent flow and wake effects. The same effects are found by applying magneto hydrodynamic theory on the sun-earth system. The first version of this model was suggested by Chapman and Ferraro in 1930 and has later been modified to the theory used today.

Distances in this thesis will often be described in number of Earth radii (R_E), where $1R_E$ equals 6378km.

2. 3.1. The shape

When the solar wind arrives at the Earth the magnetic field is compressed to reach an equilibrium between the solar wind dynamic pressure and the magnetospheric field pressure from the Earth magnetic field [Walker and Russell, 1995]. The dynamic pressure of the solar wind is given as

$$P_{sw} = Nm_p V^2 \tag{2.8}$$

where the magnitude of the solar wind velocity, V, the particle density, N and the proton mass, m_p is included. The magnetic pressure is given as

$$P_m = \frac{B^2}{2\mu_0} \tag{2.9}$$

where B is the magnetic field strength and μ_0 is the magnetic permeability. As explained by Faraday's law of induction the deformation of the magnetic field induces a current to resist the change. The boundary between the solar wind and the Earth magnetic field referred to as the magnetopause, carries this induced current. The magnetic field on the earth side of the magnetopause is strengthened by the induced current and the field outside the boundary is weakened. Because of this the magnetic field, B in Equation 2.9 will have a contribution from the induced magnetic field in addition to the steady dipole like field contribution.

The distance between the Earth and the magnetopause, L_{mp} is given as

$$L_{mp} = 107{,}4(n_{sw}v_{sw}^2)^{-\frac{1}{6}} \tag{2.10}$$

where n_{sw} is the solar wind density and v_{sw} is the solar wind velocity. The number 107.4 has been determined empirically. A change in the solar wind pressure will change the

distance between this boundary and the Earth and also cause a change in the current density in the magnetopause.

The magnetopause boundary typically forms at around $8R_E$ to $10R_E$ upstream from the Earth, but in cases of extreme solar wind pressure the magnetopause can come all the way into $5R_E$. Lower solar wind pressure can make it stretch out to about $13R_E$. The thickness of this sheet has been found to vary from 200 km to 1800 km [Berchem and Russell, 1982]. A four-spacecraft study with the Cluster satellites [Haaland et al., 2004] resulted in a thinner boundary on average. The variance in the data is however larger than in the study of Berchem and Russell.

In front of the magnetopause the solar wind is slowed down from supersonic to subsonic speed. The deceleration is caused by the shock front that appears when the solar wind hits the Earth and flows around. This bowshock is a few earth radii ahead of the magnetopause [Walker and Russell, 1995].

2. 3.2. Solar wind - magnetopause interaction

At the beginning of the 1960s, Dungey proposed that the solar wind IMF interacts with the Earth magnetic field [Dungey, 1961]. He argued that a reconnection process could take place at the subsolar point of the magnetosphere if the IMF is antiparallell with the Earth's magnetic field. In 1973, Cowley suggested that only a component of the IMF has to be antiparallell with the Earth magnetic field lines [Cowley, 1973]. Later several studies have provided empirical evidence in support of Cowley's theory of a component reconnection. A component reconnection also allows reconnection to take place on the tail lobe and on the flanks of the magnetopause.

Earlier in this chapter the magnetic reconnection have been described in a general case. After a reconnection on the dayside of the magnetopause, magnetic flux is connected to the IMF and the Earth magnetic field is said to be open. This means that the field line is not connected to the opposite pole on Earth any more and is instead connected with the Solar magnetic field. Because of the solar wind, the newly opened field lines are convected over the polar areas, adding up magnetic flux in the nightside. This flux transport gives rise to a stretched tail on the nightside.

During a reconnection process when the Earth magnetic field is opened, solar wind plasma can enter the magnetosphere. The epsilon parameter

$$\varepsilon = vB^2 \sin\left(\frac{\theta}{2}\right)^4 l_0^2 \qquad (2.11)$$

provides a measure of how much energy that is transferred into the magnetosphere from the solar wind during a reconnection [Akasofu, 1981].

This parameter takes into account the size of the reconnection area (l_0), the direction of the magnetic field (θ), magnitude (B) of the IMF and the solar wind speed (v). θ is called the clock angle. The clock angle is defined as

$$\theta = arc\tan\left(\frac{|B_Y|}{B_Z}\right) \qquad (2.12)$$

for B_Z positive and

$$\theta = 180 - arc\tan\left(\left|\frac{B_Y}{B_Z}\right|\right) \qquad (2.13)$$

for B_z negative. B_y and B_z are the y- and z-component of the IMF respectively. This angle goes from 0^o (due north along the z-axis) to 180^o and is always positive. The reconnection area, l_0 is empirically determined and assumed to be $7R_E$ (Østgard et al., 2002).

2. 3.3. Geomagnetic tail

On the night side the magnetic field is stretched in anti-sunward direction with magnetic field lines going towards Earth at the northern hemisphere and away from Earth in the southern hemisphere. The stretch in the tail causes the field lines to be nearly anti-parallel and a current sheet is necessary to separate the northern form the southern hemisphere. The tail length has not been exactly measured, but it can sometimes stretches out beyond $1000R_E$ in the anti-sunward direction.

Earlier measurements of a disturbed dipole field on the nightside were believed to be an evidence for large-scale ring currents in the magnetosphere. The existence of the geomagnetic tail was first proposed by Heppner et al. [1963]. Later, Norman F. Ness [1965] claimed the existence of a neutral sheet, across which the tail magnetic field changes direction from sunward to anti-sunward. The magnetic field has a minimal strength (neutral) at the neutral sheet. This was consistent with Dungey's theory suggesting a build-up of tail flux caused by reconnection on the dayside. These theories are commonly accepted today.

It is not only the magnetopause that is affected by the solar wind pressure, but also the tail cross-section [Coroniti and Kennel, 1972]. The tail flux, ϕ_T in one lobe is given by half the tail magnetic field strength multiplied by the tail cross-section,

$$\phi_T = \frac{\pi R_T^{\,2}}{2} B_T \qquad (2.14)$$

where R_T is the tail radius and B_T is the magnetic field strength in the tail. B_T is found by considering an equilibrium between the vertical component of both the magnetic pressure and the solar wind pressure at the boundary between the solar wind and the tail lobe. As the magnetic field strength decreases with increasing distance from Earth, the tail radius has to increase for the magnetic flux to remain constant [Hughes, 1995].

2. 4. Magnetospheric boundary layers

Magnetospheric boundary regions form due to interaction between solar wind IMF and the Earth magnetic field. If there is a rotation in the magnetic field across two populations of magnetized plasma, they must be interspaced with a current sheet. This is the case at the subsolar magnetopause when the IMF is southward, and on the lobes if the IMF is northward. This is also the case when the Earths magnetic field is stretched into a tail on the nightside, where the neutral sheet separates oppositely directed field lines in the tail. The current density which controls the boundary thickness is affected by the solar wind conditions. Other boundaries are affected by the solar wind more indirectly. All the boundary layers contain gradients in plasma density or particle energy. The different regions between the magnetospheric boundaries can be identified by their characteristic parameters. Figure 2.6 shows a sketch with the different boundary regions

of the Earth magnetic field; solar wind, bowshock, magnetopause, magnetosheath, tail lobe, plasmasheet, plasmasphere and cusp.

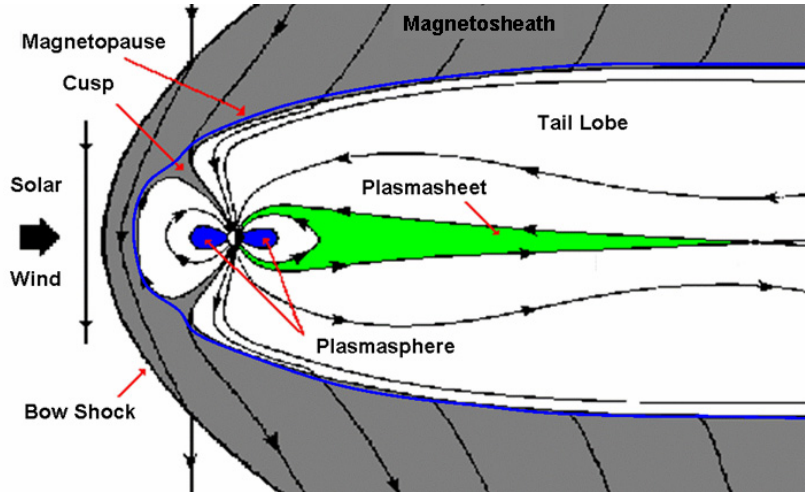

Figur 2.6: *Schematics of the different regions in the magnetosphere. [NASA's Cosmicopia]*

The solar wind plasma is characterized by high kinetic particle energy and a plasma density of about 5 cm^{-3}. Particles are slowed down at the bowshock, causing them to gather up. This results in a higher plasma density and a drop in the particle energy to about 0,1 keV in the magnetosheath. As the outermost boundary of the magnetosphere, the magnetopause is characterized by a low particle density and relatively cold plasma. Plasma in the tail lobes is very tenuous, so tenuous that scientists are having trouble measuring an exact density for this region. The particle energies in this area are also low compared to the other areas in the magnetosphere. In the central tail the densities get higher. The plasma sheet has a density from 0,05 to 0,5 cm^{-3} and energies typically between 2 and 20keV. A smaller population of electrons and ions with energies above approximately 20 keV can also be observed. In this region there is a big difference in the ion and electron energy. Ions can have energies up to 7 times higher than the electrons. The reason for this is not completely understood. Earthward of the plasma sheet is the plasmasphere which contains relatively cold but very dense plasma. Table 2.1 summaries the densities and energies of the different regions mentioned.

Plasma region	Density, cm^{-3}	Ion energy	Electron energy
Plasmasphere	100	1 eV	1 eV
Plasmasheet	0.05 - 0.5	2 - 20 keV	0.3 -3 keV
Tail lobes	0.001 - 0.1	100 eV	100 eV
Magnetosheath	10 -100	100 eV	30 eV
Magnetopause	0.1 - 1	100 eV	100 eV
Solar wind	1 -10	1 keV	10 eV

Table 2.1: *Typical densities and particle energies for different regions in the magnetosphere*

2. 4.1. Plasma sheet

In general the plasma density in the tail is low, but in the plasma sheet it can rise up to 0.5 cm^{-3}. The plasma sheet is often divided into two parts; the plasma sheet boundary layer (PSBL) and the central plasma sheet. The PSBL is a thin boundary between the tenuous tail lobes and the much denser central plasma sheet. The lobe is on open field lines while the plasmasheet is on closed field lines. At the centre of the stretched tail, there is a current sheet boundary separating sunwards directed fields in the northern hemisphere and antisunward directed field in the southern hemisphere. This boundary is commonly referred to as the neutral sheet or the tail current sheet. The current density determines the thickness of this current sheet and thereby also the plasma sheet thickness. As the tail stretches more and more at the beginning of a substorm, the current density increase and the plasma sheet gets thinner. During substorms high-speed earthward flows are observed in this layer. Substorms and their processes will be described later.

2. 4.2. IMF B_y dependence

Statistical studies [e.g., Hammond,1994; Kaufmann,2001] show that the plasma sheet is thicker on the flanks than close to the midnight sector (see Figure 2.7a). In addition several studies have showed a strong IMF dependency on the configuration. During periods with a strong IMF B_y component, the tail tends to twist towards dawn while B_y is positive (see Figure 2.7c) and towards dusk while B_y is negative (see Figure 2.7b) [Owen,1995]. This can give a large variation in the plasma sheet orientation as can be seen in the figure.

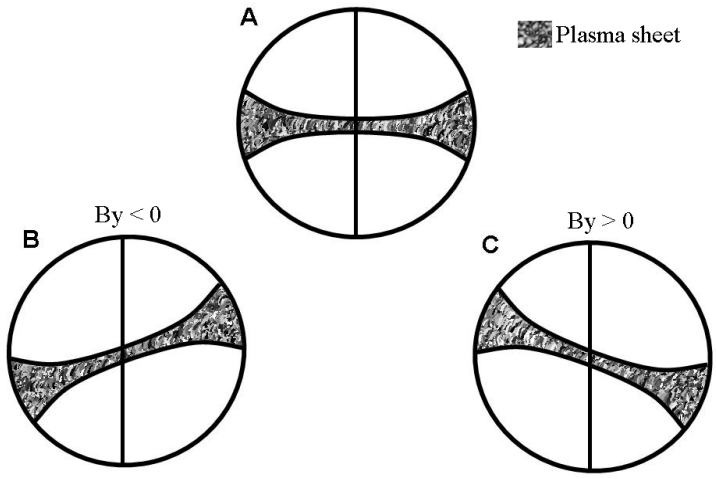

Figur 2.7: *Plasma sheet position and configuration seen from the tail. During strong IMF* B_y*, the tail is twisted towards the dawn/dusk.*

2. 5. Storm and substorm effects on the magnetotail

2. 5.1. Magnetic storm

A magnetic storm is characterized by large geomagnetic activity which causes intensification of the ring current. During such activations in the tail, huge amounts of particles and energy are transferred from the solar wind into the magnetosphere. The

largest storms are often related to CME's on the Sun. When a CME hits the Earth, the magnetopause is compressed and an increase in the magnetic field at the Earth's surface can be observed. During the evolution of a substorm the ring current increases to a maximum and then decreases slowly back to normal values again. The magnetic field increase is often referred to as a sudden storm commencement (SSC). The period of increase of the ring current is called the growth phase and the slow return to normal values is referred to as the recovery phase. [McPherron,1995]

2. 5.2. Substorm models

Substorms involve large disturbances in the geomagnetic tail and should be considered when looking at the tail configuration. Scientists still debate the triggering mechanism of a substorm and which processes that come first. Different models have been developed and two of the most common models will be described in brief.

The Near-Earth Neutral Line (NENL) model:
This model suggests that a long period of southward IMF B_z followed by a northward turning triggers a substorm. During the period of a negative B_z component, the tail builds up energy and magnetic flux. As the flux and particle density increase, the condition for a reconnection area in the tail is present. The reconnection process begins near (relative to the distant x-line) the Earth at about $20R_E$ - $30R_E$, causing ejections of plasma towards Earth and dipolarization of the magnetic field. The model explains the formation of plasmoids observed in the distant tail and consider cross tail current disruption and substorm current wedge to be a secondary result. [Baker et al., 1996]

The Cross-field Current Instability (CCI) model:
By tracing the auroral onset from the Earth along field lines one can see that the substorm onset has to occur closer to the Earth than the NENL-model describes (at about $15R_E$). Some scientists believe that plasma in the neutral sheet, close to geosynchronous orbit, becomes unstable and cause a disruption in the tail current, giving rise to a substorm current wedge and to field aligned currents [Lui et al., 1996]. Later auroral arcs expand northward corresponding to a tailward expansion of the substorm. This is not explained further in this theory. A reconnection in the tail is only a secondary process and is not needed to explain the substorm process in this model.

There are also some other models, but they are mainly just versions of the two explained above and will not be described closer in this work.

2. 5.3. Current sheet thinning and oscillations

During several studies an increase in the tail current and a thinning of the current sheet in association with substorm growth phase has been observed [Asano et al., 2004; Mitchell et al.,1990; Nakamura et al.,2002; Pulkkinen et al.,1994; Sanny et al.,1994; Sergeev et al.,1993]. It is believed that a thinning of the current sheet has effect on plasma instabilities that lead to reconnection and current disruption processes in the tail. [Sergeev et al.,1993]

There has also been observed high frequency oscillations of the current sheet with an amplitude of 1-2 R_E and a frequency of 0.1Hz [Sergeev et al.,2004]. These phenomena have been known for many years, but has not been subject to a closer research until recently. The reason is that there has not been any satellites available to investigate rapid

oscillations like this. Cluster, with 4 spacecrafts and a high time resolution, was designed to investigate small scale oscillations with high frequencies.

2. 5.4. AE-index

Ground based magnetometers under the auroral oval measure the changes in the Earth magnetic field caused by the auroral electrojets in the ionosphere. The measured disturbances are used to create two indexes, AU and AL. AU is defined as the maximum positive disturbances and AL consist of the minimum negative disturbance. The difference between AU and AL is defined as the AE-index. This is a substorm index that is sensitive to the auroral electrojets which is coupled to the diversion of the tail current.

Earlier studies have looked at relations between the AE-index and solar wind conditions. Arnoldy [1971] found a connection between the integral over B_z south and the index. Murayama and Hakamada [1975] found a correlation between AL and the solar wind clock angle.

2. 6. Geomagnetic tail configurations

Different processes cause changes in the configuration of the magnetotail. In this section the tail configuration and dynamic changes of the magnetic field.

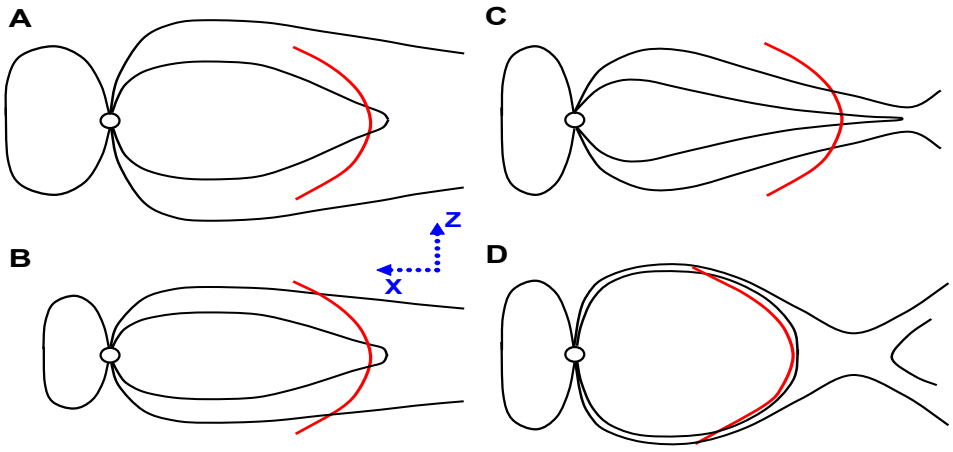

Figur 2.8: *Different tail configuration. The plasma sheet on closed field lines will be thicker closer to Earth. Cluster path showed in red.*

The plasma sheet thickness is in general dependent on the radial distance from the Earth but is also affected by geomagnetic activity caused by the solar wind.

In a quiet period with little magnetic activity (small AE-index and low solar wind pressure) the tail will only be influenced by the steady solar wind. The tail is still stretched compared to a dipole (see Figure 2.8a). As a satellite in a polar orbit goes through the tail the plasma sheet thickness can be measured. The plasma sheet thickness will appear to be thinner at apogee than closer to the Earth.

During a substorm growth phase the tail will get thinner, as shown in Figure 2.8c. The satellite will observe a thinner plasma sheet than in a quiet period because of current sheet thinning. During tail reconnection, the satellite will see a similar configuration if passing earthward of the x-line. (Chances of a satellite crossing straight through the reconnection area are very small).

Another possibility is that the satellite crosses the plasma sheet after a period with dipolarization. This is possible if the reconnection area in the tail is far from the path of the satellite. In this case the satellite will only cross the plasma sheet close to Earth and observe large thicknesses.(See Figure 2.8d)

During periods with high solar wind pressure the geomagnetic tail will look much like the case in Figure 2.8b. The configuration is similar to the one in Figure 2.8a, but the satellite will in this case encounter a thinner plasma sheet. This configuration is caused by solar wind pressure which acts on the tail lobe, compressing the total tail cross-section.

The tail is very dynamic and may reconfigure many times during each satellite passage. The configurations mentioned above will be in a constant change and rapid variations between the different configurations may occur.

2. 7. Introductory statistics

Some statistical terms will be used later in this thesis and they will be described in this chapter. The following information is taken from Moore and McCabe [1999].

In order to use statistical analysis the data have to consist of random variables meaning that they are not picked by preferences. Another criterion is that the data set has to consist of independent variables. This is to ensure that the probability of measuring a certain value does not change during the experiment. If these two criteria are not met, the statistical analysis will not provide reliable results.

2. 7.1. The mean and median

In a set of data, the mean value is the average value of all the measurements and indicates the “true” value of the data. The mean, $\bar{x}$, value is found by dividing the sum of all the measurements, x_i, by the number of measurements, N

$$\frac{\Sigma_i x_i}{N} = \bar{x}. \qquad (2.15)$$

Another way to find an average value for the data set is to calculate the median. This parameter is the middle measurement in the data set. The median is found by first sorting the data by values in ascending order and then choosing the value in the center position. The mean value is very sensitive to a few extreme values deviating largely from the other measurements. The median on the other hand is almost untouched by such extremes.

2. 7.2. Variation and standard deviation

The difference between the maximum and minimum measured values tells something about the variation in the data set. This variation gives an idea of how good the mean value is to represent the data set. If there is a large variation in the data, it means that more measurements are needed in order to calculate a correct mean value. The standard deviation given in Equation 2.16 is a measurement of the variability in the data set.

$$\sigma = \sqrt{\frac{1}{N-1}\sum_i (x_i - \bar{x})^2} \qquad (2.16)$$

N is the number of measurements, x_i is the measured values and $\bar{x}$ is the mean value of the data set. The computation of the standard deviation uses the deviation of the measurements from their mean value. This gives a good estimate of the spread of the data. The standard deviation is used to indicate the uncertainty in the mean value and can also be used to limit the range of acceptable measurements.

2. 7.3. Probability distributions and confidence interval

Statistical analysis makes use of probability calculations. A probability distribution function describes the probability that a random variable x takes on a certain value in an experiment. The most used probability distribution function is the normal distribution (see Figure 2.9). A normal distribution is always normalized so that the area under the function equals one or 100%. This equals the probability of getting one of the values in the distribution. The shaded area in Figure 2.9 corresponds to 95% of the area under the distribution function. This means that there is a 95% probability of finding the true value of μ inside this interval called the confidence interval. The shaded area is found by taking the integral over the probability distribution function, P(x) between -a and a.

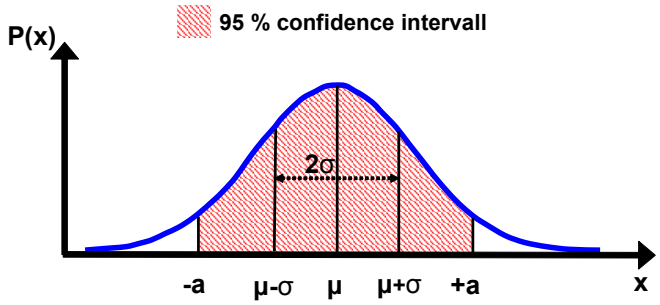

Figur 2.9: *Normal probability distribution function with mean,* μ and standard deviation, σ. *The shaded area indicates a 95% confidence interval*

2. 7.4. Data correlation

Comparing two sets of data is often done to see if the data have a linear relationship through e.g. a classical least-square fitting. The correlation coefficient is a measure of the direction and strength of the linear relationship between two sets of parameters. A correlation coefficient of 1 or -1 indicates that the two sets of data have a perfect linear correspondence. On the other hand, if the coefficient is 0 it means that there is no linear dependence between them. In cases where the correlation coefficient is zero the data may however be correlated but not linearly.

There is a probability that the calculated correlation coefficient is found by random chance and that the true correlation is zero. If this probability is outside the confidence interval (i.e. have a value that lies outside the shaded area in Figure 2.9), the calculated correlation is considered to be significant. Before the correlation coefficient is calculated the level of significance should be decided.

2. 7.5. Regression

If there is a linear relation between the two data sets, a regression line can be found. This is the best fit straight line to expressing linear relation between the two data sets. The slope of the line is related to the correlation coefficient and the standard deviations for the two parameters. The interception point is found by the use of the two mean values.

Chapter 3

Cluster II

3. 1. The mission

As a part of ESA's Solar Terrestrial Programme, the most important mission for the Cluster satellites is to investigate the interaction between the solar wind and the magnetospheric plasma. With four satellites, Cluster is designed to provide accurate measurements of three-dimensional and time-varying phenomena. It is also possible to distinguish spatial and temporal variations for the first time.

The original idea was that Cluster, together with the Solar Heliospheric Observatory (SOHO), were going to investigate the relation between the Sun and the Earth's environment. The history turned out somewhat different from the plan when the first launch of Cluster failed. [Escoubet et al.,1997] A new Cluster project came to life and the operation lifetime for Cluster II started in February 2001. It was supposed to end in 2002, but after that the mission has been extended twice. First the mission was extended until December 2005 and it has recently been prolonged until 2009.

3. 1.1. Launch and orbit

In 1986, ESA selected the Cluster mission to be a part of ESA's Solar Terrestrial Science Programme (STSP). Ten years later, in June 1996, the first Ariane-5 launch vehicle was supposed to launch the 4 satellites into orbit, but just after takeoff a failure of the rocket guidance system made it necessary to command destruction of the rocket. The explosion led to a short mission for Cluster (37 seconds) (see Figure 3.1).

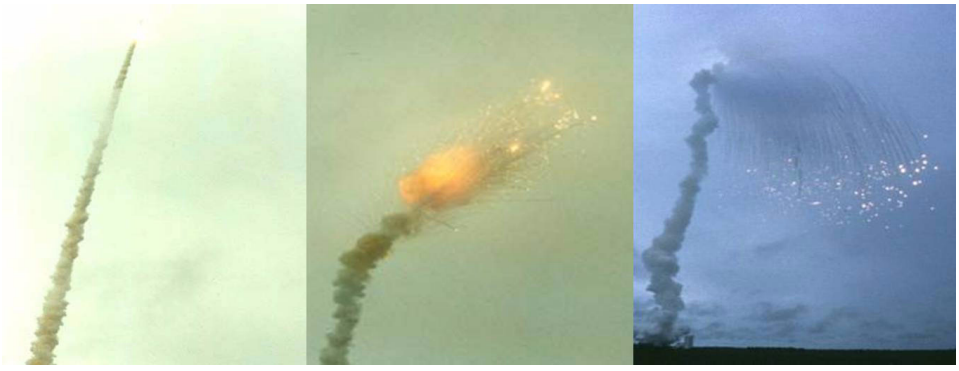

Figur 3.1: *Launch of the first Cluster satellites in 1996. The whole project went up in smoke. Taken from [CLUSTER II - Project team, 2000]*

The investigators hoped to save some instruments from the debris from the spacecraft, but the satellites were totally destroyed. Shortly after, the Cluster-team was granted money to build a new satellite based on the test instruments and spare parts left over

from the original mission. A new satellite rose from the ashes and was named Phoenix, after a bird in a greek myth (See "Apendix B"). One problem was that only one satellite would be insufficient to cover the scientific goals set for the first mission. The potential scientific achievements were so important that in April 1997, ESA decided to build three more satellites. This time the Cluster-II satellites were successfully launched in pairs, by two Russian Soyuz rockets, one in July 2000 and one in August 2000. [Cluster-II Project Team, 2000]

The satellites were launched into an ecliptic polar orbit with apogee at 19.6 R_E and perigee at 4 R_E [Escoubet et al.,1997]. The line of apsides is around the ecliptic plane. Since the orbital plane is fixed in space, the Earth rotation around the sun causes the magnetosphere to sweep through the plane of orbit. With an orbit period of 57 hours a 360^o view of the magnetosphere can be achieved during one year (see Figure 3.2).

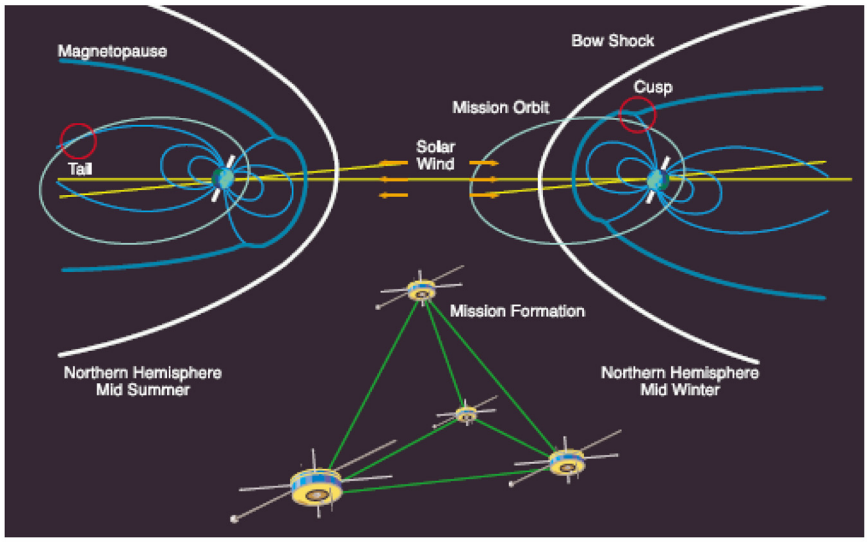

Figur 3.2: *The Cluster orbit throughout the year. The Earth's rotation around the sun causes the Cluster satellites to enter the solar wind and high cusp areas in the winter and the magnetotail during the summer. [ESA-Cluster]*

The polar orbit makes it is possible to study the cusp and the polar areas, as well as getting information about the direct entry of solar wind particles in the polar cusp. This orbit also allows studies of the earth magnetotail, cutting through the magnetospheric boundaries instead of floating between them like many previous satellite missions.

In orbit around Earth, the four Cluster satellites form a tetrahedron. Because of orbital dynamics the distance between the satellites will not be constant. At one point in the orbit the satellites may be equally distanced and in other parts of the orbit they may follow each other like a string of pearls [Escoubet et al.,2001]. The formation is adjusted periodically so that the best tetrahedron formation is achieved as regions of special interest are crossed. During spring the formation is optimized when the satellites cross the two cusp areas. In the autumn the tetrahedron formation is optimized at apogee when Cluster crosses the neutral sheet.

The distance between the satellites can also be changed by mission operators and is optimized in order for the distance to match the scale length of the plasma phenomena under investigation [Escoubet et al.,2001]. During 2001 the distance between the satellites varied between 200km to 2000km during one orbit. In 2002 this was changed to vary between 100km to 1-3R_E. In 2003 the variation in the distance between the satellites was decreased again with a smallest distance of 200km.

3. 1.2. Scientific goals

The Cluster satellites have been constructed to investigate the interaction between the solar wind and the magnetosphere and will be the most detailed investigation ever made of this interaction. So far, the possibilities the four spacecrafts have given have not been fully exploited and scientist have just recently started to make use of the multi-spacecraft capabilities. By using four spacecraft a magnetospheric structure changing in both space and time can be observed.

With one spacecraft, the normal to a boundary passing the satellite can be found using minimum variance analysis of the magnetic field. With four measurements on the same boundary, the direction of propagation and shape of the structure can be determined. Four point measurements can also be used to calculate the current density around the spacecrafts. The difference between the measurements of the magnetic field on each spacecraft makes it possible to calculate the curl $\vec{B}$, and thus $\vec{J}$ [Escoubet, 2000]. This knowledge can be important when studying current layers existing in many of the magnetospheric boundaries.

Orbiting the Earth the Cluster satellites are visiting key regions like the cusp and the magnetotail. They also cross through the magnetopause collecting valuable information of particle flows in the auroral zones. [Escoubet et al., 2000]

As mentioned earlier scientists have the possibility to change the distance between the four spacecraft. The possibility to have a small distance between the space crafts makes the Cluster satellites well suited for studying small-scale structures in the magnetospheric environment. During large separations structures of larger scales can be investigated.

3. 2. Instruments on Cluster II

The four Cluster satellites are identical and each satellite have 11 instruments on-board. Together the satellites are capable of measuring parameters like electric and magnetic field, plasma density and plasma waves. The instruments are constructed to measure rapid changes in time and have a relatively good time resolution compared with earlier missions. The different instruments are listed in Table 3.1. Instruments used in this thesis are described in more detail below.

Table 3.1: The 11 instruments on Cluster.

Instrument	Acronym
Fluxgate magnetometer	FGM
Spatio-temporal analysis of field fluctuation experiment	STAFF
Electric field and wave experiment	EFW
Waves of high frequency and sounder for probing of electron density by relaxation	WHISPER
Wide band data	WBD
Digital wave processing experiment	DWP
Electron drift instrument	EDI
Active spacecraft potential control	ASPOC
Cluster ion spectrometry	CIS
Plasma electron and current experiment	PEACE
Research with adaptive particle imaging detectors	RAPID

3. 2.1. FGM

Similar to many other space missions Cluster also has an instrument to monitor the magnetic field. The instrument is a tri-axial fluxgate magnetometer which measures the magnetic field along the Cluster orbit. One sensor is placed on a boom at a distance of 5.2 m from the spacecraft in order to minimize the magnetic disturbances created by the spacecraft. The other sensor is placed 1.5 m inboard of the first sensor. [Balogh et al., 1997] The instrument can take high time-resolution measurements with up to 67 samples per second.

A fluxgate magnetometer relies upon the theory of induction. When a satellite orbits in the magnetosphere, the magnetic field will change in time and cause induction of currents in a ring core sensor. The amplitude of the induced current is propositional to the change in the magnetic field. The magnetic field vectors are calculated using knowledge about the satellite position and it's orientation. [McPherron, 1995]

This instrument is important for measuring current densities in the magnetospheric boundaries, using Ampere's law and 4 point measurements of the magnetic field. Data can also be used to investigate magnetic waves and retrieve particle information based on particle motion around field lines. In this thesis FGM data will be used to identify neutral sheet crossings.

3. 2.2. EFW

This instrument is designed to measure electric fields and density fluctuations with a very high time resolution. The instrument consists of four spherical sensors located at the end of four 50 meter long wire booms. These sensors are in the spacecraft spin plane and are able to do up to 36 000 measurements per second. The main idea behind the

instrument is to measure potential differences in the spin plane in order to determine the electric field components in this plane.

Measurements of the spacecraft potential can be used to determine the electron density in the plasma. As the spacecrafts are exposed to direct sunlight, the photoelectric effect builds up charges on the surface. The equilibrium potential varies with the plasma density and it is possible to determine the density by measuring the spacecraft potential. This will be explained further in [Gustafsson et al., 1997].

An advantage with this experiment is the high time resolution and the fact that it can make good measurements even in low density plasma (down to 10^{-2} cm^{-3}). As will be explained closer in “Chapter 4” , the measurements do not give an exact value for the density, but gives a very good estimate of the change in density. This makes this instrument well suited for detecting boundary passages.

3. 2.3. WHISPER

The main purpose of this instrument is to measure the plasma density in the range 0.2-80 cm^{-3} with a time resolution of 28 sec. With a fast fourier transform (FFT) calculation, the instrument can also be used to investigate plasma waves. The instrument consists of a relaxation sounder that works the same way as a classical radar. A radio wave transmitter sends out a signal at a frequency, f, during a time, T. This signal will be affected by the frequency of the surrounding plasma. By increasing the outgoing signal in steps, the resonance frequency can be found. The resonance frequency equals the plasma frequency and thus the plasma density can be calculated. The time resolution is relatively low compared with the EFW experiment. [Décréau et al., 1997]

3. 2.4. CIS

CIS measures the ion density and velocity and provide data with a high time resolution of 4s (the spacecraft spin period). CIS consists of two parts; the Hot Ion Analyzer (HIA) and the Ion Composition and Distribution Function Analyzer (CODIF). The two instruments have three spherical elements; an inner hemisphere, an outer hemisphere with a circular opening and a small circular top cap over the opening in the outer hemisphere. With a potential difference between the inner and outer hemisphere, charged particles are guided down into the detector and counted. The CODIF is a highly sensitive mass-resolving spectrometer creating a 3D velocity distribution function for the major ion species in the energy range from the spacecraft potential to 40keV. The HIA instruments also measure a 3D velocity distribution but does only measure high energy ions and are not able to distinguish between the different ion species. Both instruments have a 360^{o} field of view. [Réme et al.,1997]

Chapter 4

Magnetospheric boundaries

When a satellite traverses magnetospheric boundaries, these can be identified as gradients in the density profile. In this chapter, the spacecraft potential will be used to calculate a plasma density distribution in the magnetosphere. This density distribution will provide an image of the different boundary layers.

The plasma density is derived from the potential difference between the spacecraft and the surrounding plasma. This potential difference will be referred to as the spacecraft potential in the following text while the real potential of the satellite will be referred to as the satellite potential.

4. 1. Objectives

Escoubet et al. [1997] have mapped magnetospheric boundary layers using data from ISEE-1 satellite. Based on spacecraft potential measurements from 1977 to 1984 they calculated an average density distribution for the magnetosphere that clearly visualizes the boundaries. In order to create the density distributions, the magnetosphere were divided into bins which the data were sorted into. The density distributions were then divided into geomagnetically active and non-active periods using the AE-index. They found that the magnetosphere were more compressed during high magnetic activity. A thicker and denser plasma sheet was also observed at midnight during high activity.

The orbit of ISEE-1 satellite had a small inclination relative to the ecliptic, and therefore explored the magnetosphere at low latitudes, and at relatively small distances from the neutral sheet in the magnetotail. Cluster, in an eccentric polar orbit makes it possible to get a view of the boundaries at higher latitudes, like the plasma sheet boundary layer and the cusp. As the Cluster satellites have been in orbit since 2001 there now exists 4 years of data. Calculating an average value for all the measurements made at the same spatial position provides a statistical image of the density distribution in the magnetosphere.

4. 2. Plasma density

Pre-processed data with a time resolution of one minute have been collected from the Coordinated Data Analysis Web (CDA-web: http://cdaweb.gsfc.nasa.gov/). The spacecraft potential with corresponding spacecraft position has also been collected from this web-based database.

4. 2.1. Converting potential to densities

The EFW instrument makes use of the photoelectric effect to derive the spacecraft potential. This potential is later used to calculate the plasma density. Emission of photoelectrons (I_{phos}) will tend to drive the spacecraft to a positive potential. In a tenuous plasma a large number of the photo emitted electrons will return to the spacecraft. The current of electrons that are emitted into the surrounding space (I_{phs}) will be balanced by a current of ambient electrons attracted to the positive satellite from the surrounding plasma (I_{es}). In a denser plasma the currents will balance at a lower spacecraft potential. The relation between the different currents is shown in Figure 4.1.

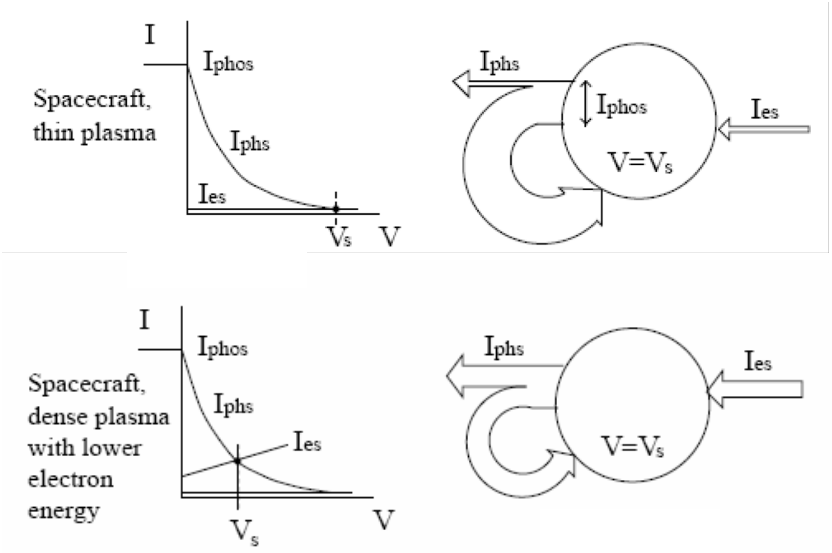

Figure 4.1: *Schematic illustration of the current balance of the spacecraft. Vs is the spacecraft potential. From [Pedersen et al, 2001]*

In order to obtain a value for the potential that also corresponds to the plasma density, the background plasma potential has to be subtracted from the measured satellite potential. The probe potential is kept close to the plasma potential by adding electrons through a bias-current. This prevents the probe from reaching a high positive potential. The probe potential is close to the surrounding plasma potential when the ambient electron current decreases toward zero. [Pedersen et al., 2001]

The relation between the spacecraft potential and the plasma density is given as

$$N = 200e^{-\left(\frac{(V_s - V_p)}{0,9}\right)} + 100e^{-\left(\frac{(V_s - V_p)}{2,1}\right)} + 2e^{-\left(\frac{(V_s - V_p)}{12}\right)} \qquad (4.1)$$

where Vs and Vp is the satellite potential and the probe potential, respectively. The equation describes the plasma density in number of particles per cubic centimeter. This equation is empirically deduced by calibrating the spacecraft potential with other instruments on-board Cluster (CIS, PEACE, ASPOC, EDI and WHISPER). The relationship has not been published yet and some more calibration is needed. Still the equation gives a relatively good description of the density in the other magnetospheric regions such as the magnetopause, plasma sphere, and tail lobe. [Arne Pedersen, private communication]

The EFW experiment is good for identifying changes in the density and is useful when boundary layers are to be identified by the density variation. Other particle experiments, measuring plasma density on the Cluster spacecrafts (i.e. WHISPER, CIS) will acquire very few counts in a tenuous plasma and their measurements will not be reliable in such plasma populations. An other problem is that the spacecraft often reaches a high positive potential in very tenuous plasma. This high potential will affect the density measurements made by other instruments. A high positive potential will attract electrons, shield out ions and will result in too high or too low density measurement. [Pedersen et al., 2001]

4. 2.2. Comparing with other density measurements

The plasma density from March 16th, 2001 have been calculated from the spacecraft potential. This data is then compared with density measurements from WHISPER and CIS. In Figure 4.2a the density derived from the EFW instrument is compared with density measurements from WHISPER. At the same time as the EFW instrument measures a drop in the density, at about 18:00 UT and 22:00 UT, there is large variations in the WHISPER measurements. Simultaneously, the quality controlling variable, derived from WHISPER data is close to zero, indicating that the data is not reliable in this time period [Daly,2002]. This control variable is plotted in Figure 4.3. For the rest of the period shown in Figure 4.2a, the WHISPER measurements correspond well with the EFW experiment.

The EFW data have also been compared with data from CIS (see Figure 4.2b). The figure shows that the CIS instrument in general produces somewhat lower values for the plasma density than the EFW instrument. Between 12:00 UT and 18:00 UT, however the two instruments seem to deliver the same results. During the two periods with a strong decrease in the plasma density, the two curves follow each other rather well except for the very lowest plasma densities. Between 21:00 UT and 24:00 UT the difference between the two measurements is significant. In a tenuous plasma the spacecraft goes to a highly positive potential. Positively charged particles will not reach the spacecraft unless they have very high energies. This dip correspond to a tail lobe passage (explained below) where the particle energy is very low and CIS will therefore underestimate the plasma density [Torkar et al.,2001]. The largest difference between the EFW and CIS data is almost a factor of 10. In some tenuous plasma regions the EFW instrument provides the only possibility to get information on the plasma densities

a

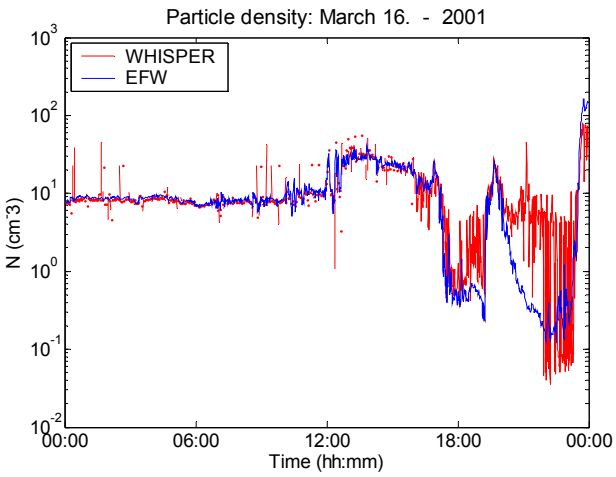

b

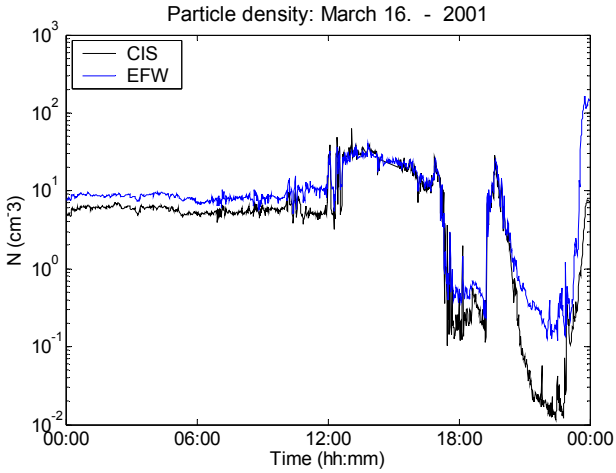

Figure 4.2: *Plasma density deduced from the spacecraft potential is compared with plasma densities measured with two other instruments on Cluster, Whisper (a) and CIS (b).*

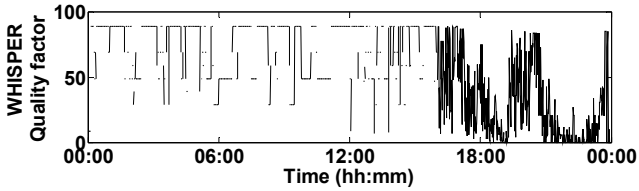

Figure 4.3: *The quality factor from WHISPER. When the quality factor is zero the data are not reliable.*

4. 2.3. Density along the orbit

Figure 4.4 displays electron density variations along the Cluster orbit on March 16th 2001. This is from the same day as the data shown in Figure 4.2. The characteristic densities listed in Table 2.1 will be used to define some of the boundaries that are crossed by the satellite during this orbit.

In part 1 of the satellite path from x = 19 R_E to x = 13R_E in Figure 4.4., the satellite experience a plasma density of about 10cm^{-3} indicating that the satellite is situated in the solar wind. Later on the spacecraft enters a region with significantly denser plasma (2). This density of about 30cm^{-3} corresponds to magnetosheath plasma. After going through the magnetosheath, Cluster crosses the magnetopause and enters the much colder and thinner plasma on closed field lines inside the magnetosphere. Cluster then enters the cusp (3) which has a density close to the density found in the magnetosheath. After crossing the cusp, the satellite moves through the tenuous lobe and ends up in the dense plasmasphere (4) with characteristic densities at 100cm^{-3}. This lobe crossing corresponds to the large drop in the density curve at about 22:00 in Figure 4.2.

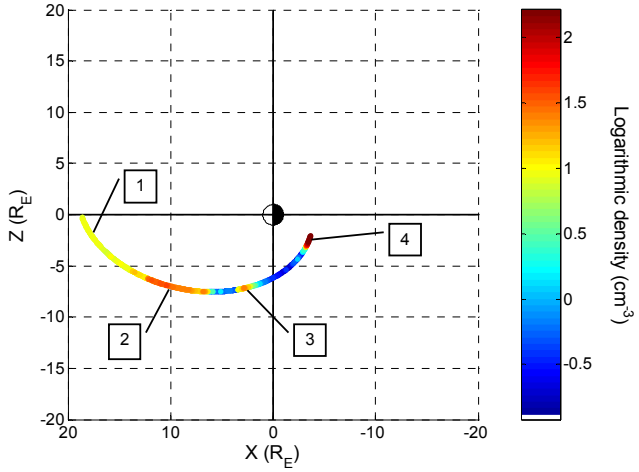

Figure 4.4: *Cluster orbit 16. Mars 2001. The plasma density showed in colors is plotted along the path. The satellite is first in the solar wind (1), enters the magnetosheath (2), passes through the cusp (3) and finally enters the plasmasphere (4)*

4. 3. Boxing

The spacecraft potential have been converted into plasma densities the data are ready to be sorted into bins.

4. 3.1. Bins

Cluster orbits a volume of about 40R_E in x- and y-direction, times 20R_E in the z-direction. This volume are divided into bins and three different bin-sizes have been tried:

i) Cubes with size of 1R_E resulting in 40 bins in each direction
ii) Cubes with size of 0.67R_E resulting in 60 bins in each direction
iii) Cubes with size of 0.57R_E resulting in 70 bins in each direction

Before deciding which bin-size to use, it is necessary to consider how long distance the satellite travels between two measurements. If the bin-size is smaller than this distance, it can result in empty bins. Cluster have highest speed near perigee (close to earth) reaching a maximum speed at about 5 km/s. Taking into account the maximum speed and the time resolution used, of one minute, the minimum bin-size can be calculated. With the given parameters the bins can be no smaller than $0.047R_E$ (=> 300km) in order to have at least one measurement in each box. Increasing the distance between each data point means that larger bins are needed in order to have sufficient number of measurements in each bin.

The number of elements in a statistical distribution is important. An average value is an estimate of the correct value of the measurement. If there is a large variance in the data, a higher number of measurements is needed to get a good estimate of the correct value. A lower limit for the number of measurements in each bin is set to 20 hits. Values in bins with fewer hits are considered to be unreliable.

The maximum and minimum number of hits in each bin after collecting three years of data, is shown in Table 4.1. According to the results presented in this table there is not a big difference between the 60x60x60 bins and the 70x70x70 bins. Dividing the magnetosphere into 40x40x40 bins is the only choice that can guarantee that all bins contain enough measurements to give a statistically reliable result (i.e. more than 20 hits).

# bins	max # hits/bin	min # hits/bin
40x40x40	106	21
60x60x60	71	14
70x70x70	60	12

Table 4.1: *Maximum and minimum number of measurements in each bin*

The spatial resolution will also have an affect on the number of hits in each bin. The Cluster satellites have an elliptical orbit around Earth. After one orbit the next orbit will be shifted about $0.75R_E$ westward because of the earth orbit around the sun. The distance between the two orbits will be larger at apogee than at perigee. If the bins are smaller than the largest distance between two orbits, several bins can end up with few or no measurements.

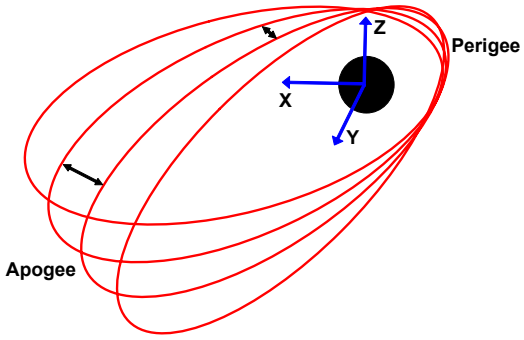

Figure 4.5: *Example of 4 Cluster orbits. The distance between two orbits is larger at apogee than at perigee.*

After taking these considerations into account, the best choice of bin-size will be the largest one. It is on the other hand, also important to keep the bin-size as small as possible in order to resolve distinct boundaries in the final image. Considering these arguments, the matrix of 60x60x60 bins was selected, i.e. $0.67R_E$ resolution.

The number of measurements in each bin has been calculated using the first three years of available data. This resulted in 746 118 measurements. These data are displayed as 2D images in Figure 4.6. The number of hits have been summed over the third axis, which is not shown in the images. Figure 4.6 shows that there are just a few bins with less than 20 hits.

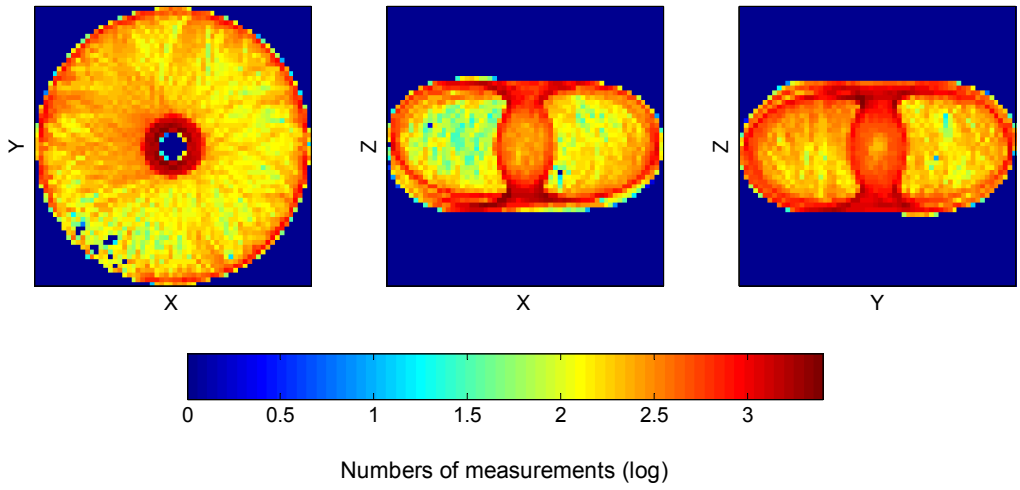

Figure 4.6: *The magnetosphere were divided into 60x60x60 bins. The figures shows the number of hits in each bin averaged over the third axis*

The Cluster satellites do not cover all the magnetospheric regions. A torus shaped sphere laying symmetrically around the Earth, with the rotational axis perpendicular to the orbit

plane, is never visited by Cluster. The two images on the right in Figure 4.6 shows two D-shaped areas with fewer counts. This corresponds to the donut-shaped sphere having no data. The values in these bins relate to measurements made near the magnetopause and the magnetosheath regions outside of this empty sphere.

4. 3.2. Statistical analysis

After collecting spacecraft potential data for the time period 2001 - 2003, the data are sorted into bins. For each bin, an average value is calculated. This results in a 3D-matrix consisting of average values of spacecraft potentials. The potential is then converted into plasma density by the relation given in Equation 4.1. To visualize the data, 2D images are shown in Figure 4.7 with data averaged over the third dimension. A logarithmic scale is used for the density in order to make the boundaries sharper and more distinct.

4. 4. Identifying boundaries

Several boundaries in the magnetosphere can be recognized in Figure 4.7 by considering the characteristic plasma density in the different regions which are listed in Table 2.1. In order to guide the eye, the statistical position of the bow shock and the magnetopause is superimposed on Figure 4.7a and c. The bow shock is drawn at $x = 15R_E$. This is the statistically average position of the bow shock found by Peredo et al. [1995]. An earlier statistical study done by Sibeck et al. [1991] have found the average position of the magnetopause to be at about $x = 10R_E$.

4. 4.1. Bowshock and magnetopause

In Figure 4.7a the yellow and bright red crescent shaped area to the left corresponds to the solar wind. Closer to the Earth is the magnetosheath. The boundary between the solar wind and the magnetosheath is not very obvious in the picture but a density gradient in negative x direction is visible. At the bow shock the solar wind plasma velocity starts to decrease. As the plasma passes through the magnetosheath the velocity decrees gradually.

The plasma in the magnetosheath reaches a density of about $20cm^{-3}$ just in front of the magnetopause. The magnetopause is the yellow parabolic shaped area in Figure 4.7a situated at about $7R_E$ upstream from Earth. This is a little closer than the statistical position calculated by Sibeck et al. [1997]. The reason for this is that many measurements of the magnetosphere are made at high latitudes. Since the Cluster satellites are in a polar orbit, the magnetopause is not crossed in the equatorial plane but with an elevation above or below it. When projecting the magnetopause crossing down to the ecliptic the magnetopause is mapped at a x-position that is closer to the Earth than the radial distance. By using the x-position of the magnetopause found above ($x = 7R_E$) and assuming that Cluster crosses the magnetopause at about $z = 7R_E$, the radial distance from the Earth to the magnetopause will be about $10R_E$ (i.e. $\sqrt{[(7R_E)^2 + (7R_E)^2]}$).

a

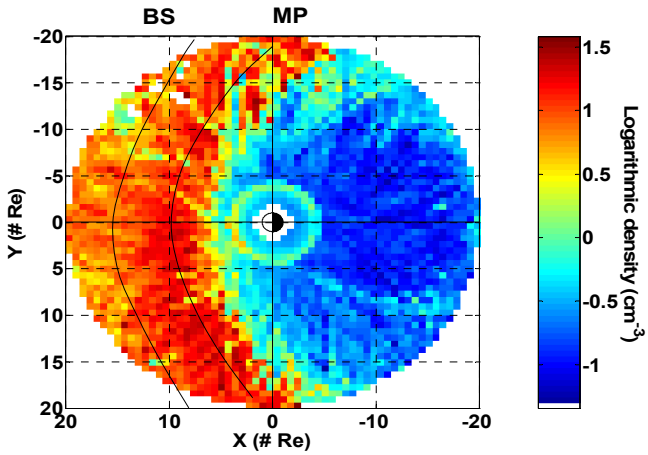

b

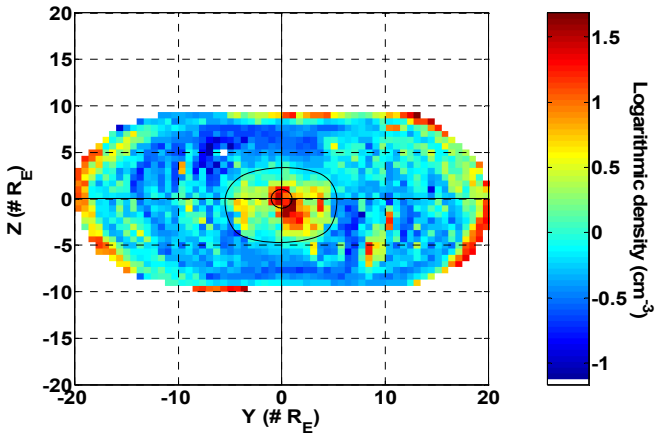

c

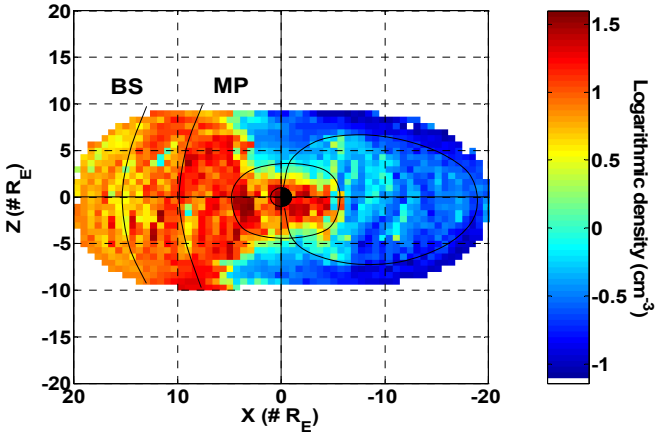

Figure 4.7: *Density distribution measured by the EFW instrument on Cluster. Magnetospheric boundary layers are defined in section 4. 4. The statistical position of the bow shock, (BS) and the magnetopause (MP) is marked. The plasmasphere is encircled in the centre of picture b and c.*

4. 4.2. Plasmasphere

In Figure 4.7c the plasmasphere can be seen as a dense elliptical sphere around the Earth. The dayside boundary is not easily spotted because the position overlaps with magnetopause densities. A thin line is drawn along the boundary to help visualize the shape. The plasmasphere is somewhat compressed in the z-direction and stretches out to about $5R_E$ on the night side. A higher density can be seen on the dayside of the plasmasphere. The plasmasphere can also be seen in Figure 4.7a as a circle between $3R_E$ and $5R_E$ with a higher density in the dayside.

The higher density in the dayside plasmasphere is consistent with the findings of Laakso et al.[2002]. They concluded that the density is higher on the dayside than in other areas in the plasmasphere during quiet periods. However, they do not offer any explanation to this observation. During active periods they find that the density is more evenly distributed between day- and night- side. The source of plasmaspheric particles are believed to come from heated ionospheric particles that are flowing up along field lines into the plasmasphere [Wolf, 1995]. On the dayside the ionospheric particles are heated by the sun, causing more particles to enter the plasmasphere on the dayside. This can explain the difference in the density between the day- and night- side. During active periods these particles drift out towards the magnetopause and the distribution is evened out.

The plasmasphere can also be seen in the middle of Figure 4.7b as a dense area around the Earth. The figure shows that the plasmasphere is larger and have a higher density on the dusk side. The particles in the inner plasmasphere are so close to the Earth that they are affected by the Earth rotation [Wolf, 1995]. The plasma convection and the particle co-rotation cause particles to gather up on the dusk side, increasing both the size and density in the plasmasphere.

4. 4.3. Plasma sheet

It is not possible to see the plasma sheet in Figure 4.7a, but in Figure 4.7c there is a weak signature in the tail shown as turquoise. The dark blue bins in this figure correspond to the tenuous tail lobes.

Looking at the tail from behind (along positive x-axis towards the Sun) the plasma sheet can be seen in Figure 4.8 as a sheet separating the northern lobe from the southern lobe. The shape with thicker plasma sheet on the tail flanks and a thinner sheet in the midnight sector, is consistent with results from earlier studies (i.e. [Kaufmann, 2001]).

In Figure 4.8 the plasma sheet looks slightly tilted towards dawn which according to Owen et al. [1995] would be expected if IMF B_y is mostly positive during this period. Figure 4.10 shows the distribution of the IMF components during the actual period (2001 to 2003). The figure shows that the B_y component is evenly distributed around zero with highest occurrence at ± 3 nT. Hence, the B_y component cannot explain the tilt of the plasma sheet, as there is no skewness in the distribution. Another more likely explanation could be the annual variation of the tilt of the Earth rotation axis relative to the ecliptic. When averaging the data over three years the annual rotation of the earth should be evened out. But since Cluster orbits the tail only during mid-summer and early autumn the tail data contains a preferred direction on the rotation axis and the plasma

sheet will therefore appear tilted in a GSE (geocentric solar ecliptic) coordinate system (described in “Chapter 5”).

.

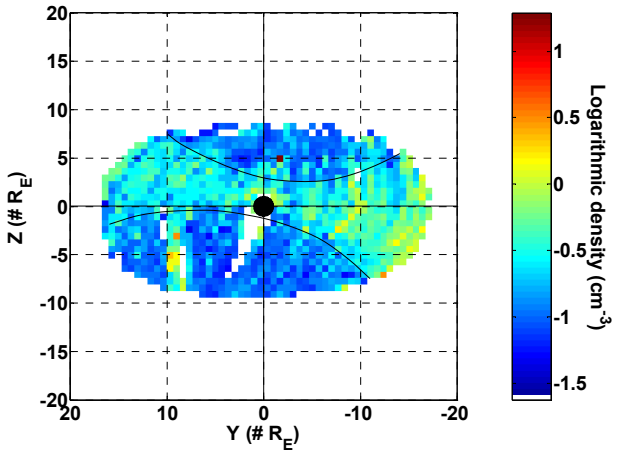

Figure 4.8: *The density distribution and the Earth viewed from the tail in the yz-plane. The plasma sheet is recognized as the turquoise and yellow biconcave shape crossing the magnetosphere with a tenuous lobe above it and below it. A slightly higher density in the magnetopause can bee seen in the dawn region at the right.*

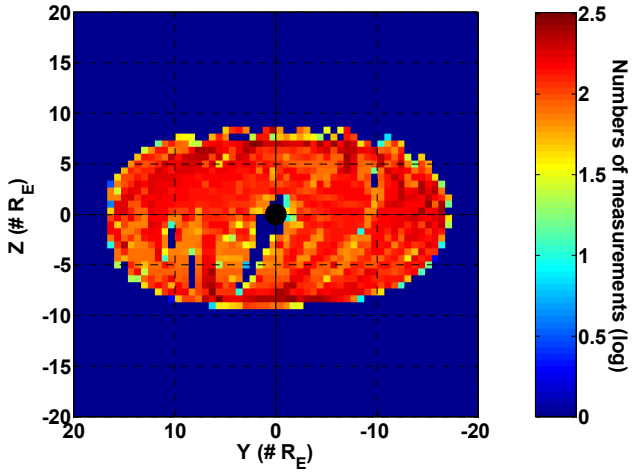

Figure 4.9: *This figure has the same view angle and axis as Figure 4.8, but the colorbar shows number of measurements instead of plasma density.*

In Figure 4.8 the data have been averaged between x = -10R_E and x = -20R_E. Leaving out all measurements made along a positive x-axis results in a plot showing only tail measurements. In addition, when looking for the plasma sheet the measurements made in the plasmasphere will only disturb the picture. Since the plasma sheet is located behind the plasmasphere at about 5-7 R_E in negative x-direction, the data between x = 0R_E and x = -10R_E are also left out in order to be sure no plasmasphere measurements are included. When leaving out more than half of the data set, the number of measurements

in each bin is lowered significantly. The plot in Figure 4.9 shows the number of measurements in each bin for the plot in Figure 4.8. Except from some empty bins, most of the bins have about 100 measurements each.

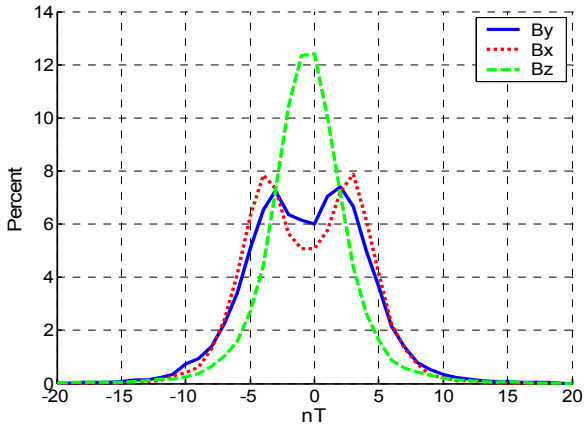

Figure 4.10: *Distribution of the IMF components for the period from 2001 to 2003.*

The high density spot in the south at the dusk side (at about y = 10, z = -5) in Figure 4.8 addresses to a tail passage around midnight between September 30th and October 1st in 2002. During this event Cluster encounters a big change in the tail magnetic field at the time of the event. The B_x and B_y component measured by Cluster change direction by 180 degrees. There is also a large enhancement of the B_z value. These changes appear about 11 hours after Cluster crossed the neutral sheet the first time and last for about three hours before magnetic field data return to normal values. The magnetic pressure is larger than the dynamic particle pressure in the solar wind at this time and may be the reason for this very unusual event. The IMF also has a strong positively B_z and a strong negative B_y component. Even though this event happens during one orbit only, it has strong effect on the statistical data.

In Figure 4.8 there are also two single bins with unusually high density. The one just above the big spot (y = $8R_E$ z = $-3R_E$) corresponds to the same orbit just a few hours earlier. The other dark red spot at y = $-3R_E$, z = $5R_E$ corresponds to orbit 338. At this day the spacecraft potential suddenly increased with about 30V and stayed almost constant at 2,7eV between 10:30 and 13:40. This looks like a false potential. A comparison between this data and data from the EFW instrument on the three other satellites, indicates that the EFW instrument on spacecraft one was not in the appropriate mode of operation at that time.

4. 4.4. Cusp

The Cluster orbit is specially suited for looking at the cusp. Many of the earlier satellite missions have been in equatorial orbits or have had polar orbits closer to the Earth. Figure 4.11 shows a cross-section of the magnetosphere in the xy-plane between 6 and 7 R_E along the GSE z-axis. Looking from right to the left in this figure, the satellite first encounters the tenuous lobe, enters the cusp and after going through the dayside magnetosphere it ends up in the solar wind. The cusp can be seen in yellow at about

$x = 5R_E$ and $y = 3R_E$. The passage in the dayside magnetopause (to the left of the cusp) includes some measurements from the magnetopause (red) and thus the boundary between the cusp and the solar wind is not very clear. The cusp and solar wind measurements are made in a season (spring) when the Earth's rotational axis is tilted towards dusk. Because Cluster orbits over the poles, is will not enter the cusp and the magnetosphere at this z-position on the dawn side during spring time. The spiral-like shape of the data is due to the Earth's rotation during one year.

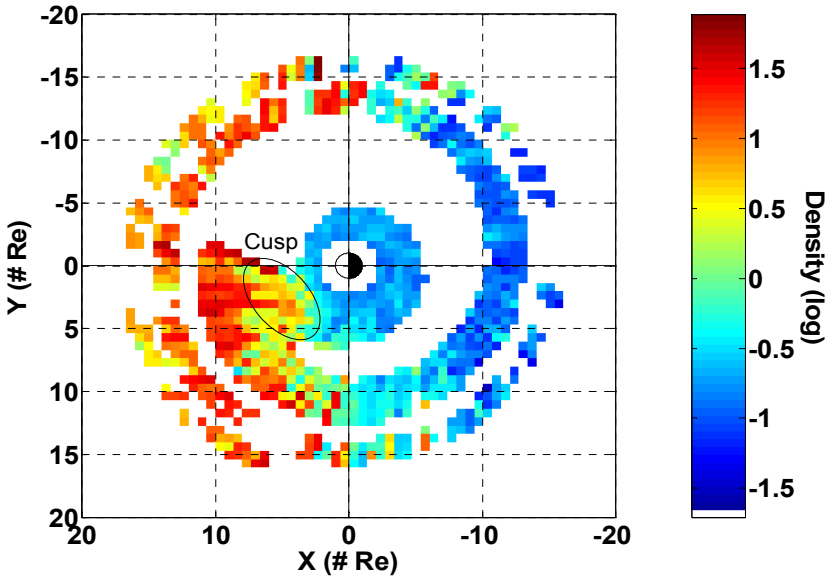

Figure 4.11: *A cross-section of the magnetosphere between $z = 6R_E$ and $z = 7R_E$*

4. 5. Comparing with geomagnetic activity

Escoubet et al.[1997] compared the shape and position of the magnetospheric boundary layers with the AE-index. They had seven years of data and could easily divide the data set up in two parts; active and non-active periods. In this study there is only two and a half years of data available. This is insufficient for a further subdivision of the data set. For this reason no comparison with the AE-index or with solar wind data is carried out.

4. 6. Summary

In this chapter the spacecraft potential measured by the EFW instrument has been used to calculate the plasma density in the magnetosphere. These data have then been used to define the different boundaries in the magnetosphere. One minute resolution data were sorted into bins with size $0{,}67R_E x 0{,}67R_E x 0{,}67R_E$. This resulted in a 3D density distribution which were used to identify the magnetospheric boundaries.

Many of the magnetospheric regions have been identified. The magnetopause was found at about $7R_E$ projected into the ecliptic plane. This resulted in a radial distance at about $10R_E$. The bow shock was harder to identify but was statistically positioned at a radial distance of $15R_E$. Closer to Earth, the plasmasphere have been easily identified as a

doughnut shaped sphere. It was also observed a higher density in both the dayside and the dusk side. The plasma sheet was a little more difficult to point out. By leaving out data from measurements taken on the dayside and in the plasmasphere, the plasma sheet can be observed. Seen from the tail, the plasma sheet has a biconcave shape. Since the measurements in the tail have only been taken during late summer / autumn the plasma sheet was a little tilted towards dawn because of the Earth's rotation around the Sun. The cusp has also been identified in a cross section image of the magnetosphere. Because of seasonal variations caused by the Earth's rotation about the sun, the cusp can only be seen on the dusk side.

In this chapter the plasma density was used to identify several boundary layers in the magnetosphere. The next chapters describe a method that makes use of the differences in the plasma energy and density between magnetospheric regions. This will be used to find the thickness of the plasma sheet.

Chapter 5

Coordinate system

Estimating the plasma sheet thickness is not a straight forward issue. During active periods the tail is very dynamic and the shape and position of the plasma sheet undergoes rapid changes. Hence, Cluster encounters many boundary crossings during one tail passage. If the tail configuration had been stable during a satellite passage through it, the plasma sheet thickness could easily have been found by using the satellite coordinates at encounter and exit of the PSBL. Unfortunately, this is not the case and a method based on some assumptions has to be used.

The plasma sheet is often assumed to be symmetric about the neutral sheet and this will be used to find the half thickness of the plasma sheet. Given that the neutral sheet position is known when Cluster crosses the PSBL, the distance between the satellite position and the neutral sheet represent the half thickness of the plasma sheet. A method to identify the neutral sheet position needs to be established. The configuration and position of the neutral sheet are strongly dependent on the tilt angle between the geomagnetic equator and the ecliptic. Several studies (e.g. Hammond et al. [1994] and Li and Xu [2000]) have earlier pointed out the importance of the dipole tilt influence on the magnetotail boundaries.

5. 1. About Coordinate systems

Studying phenomena close to the Earth makes it meaningful to use coordinates that are centered at the Earth. There are several geocentric systems, but since the Earth magnetic field is strongly affected by the solar wind, one of the axis should be in the solar direction. Two of the most frequently used coordinate systems in space physics are the Geocentric Solar Ecliptic (GSE) and Geocentric Solar Magnetic (GSM) coordinate system.

5. 1.1. Geocentric Solar Ecliptic, GSE

The coordinates of Cluster are usually given in the GSE coordinate system. In this system the x-axis is directed towards the Sun and the z-axis is perpendicular to the ecliptic plane. The y-axis is perpendicular to both the x- and the z- axes. This coordinate system is often used to display satellite trajectories and solar wind measurements.

5. 1.2. Dipole tilt - diurnal and annual variation in the GSE system

The Earth rotational axis is tilted by 23.5^{o} from the z-axis in the GSE system. In addition the magnetic dipole axis of the Earth has a tilt of 11.5^{o} relative to the Earth rotation axis. In GSE coordinates the dipole axis has both a diurnal and annual variation.

The diurnal variation of the dipole axis is caused by the Earth's rotation about its own axis (see Figure 5.1). The red dotted line in the figure is the rotational axis and the blue

thin line is the dipole axis. In the GSE system the movement of the dipole axis can be described as a cone. This will cause a variation in both the GSE yz-plane and the xz-plane.

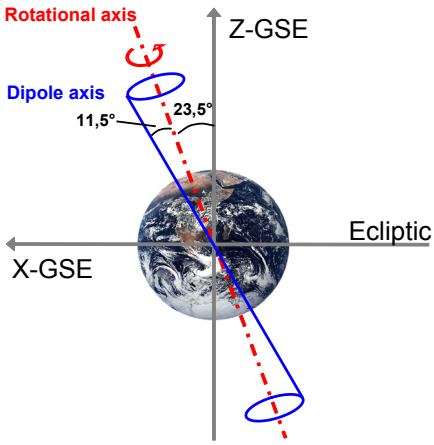

Figur 5.1: *As the Earth rotates the dipole axis makes a cone around the rotation axis, causing diurnal variations in the neutral sheet position with respect to GSE*

There will also be an annual change in the dipole axis projection into the GSE system. When the Earth orbits the Sun, the rotational axis describes a cone around the GSE z-axis leading to a annual variation in the dipole axis position in the GSE coordinate system. This is illustrated for the GSE xz-plane in Figure 5.2. The dipole axis position will vary between the two blue lines during one day and will also have an angular change relative to the GSE z-axis during one year.

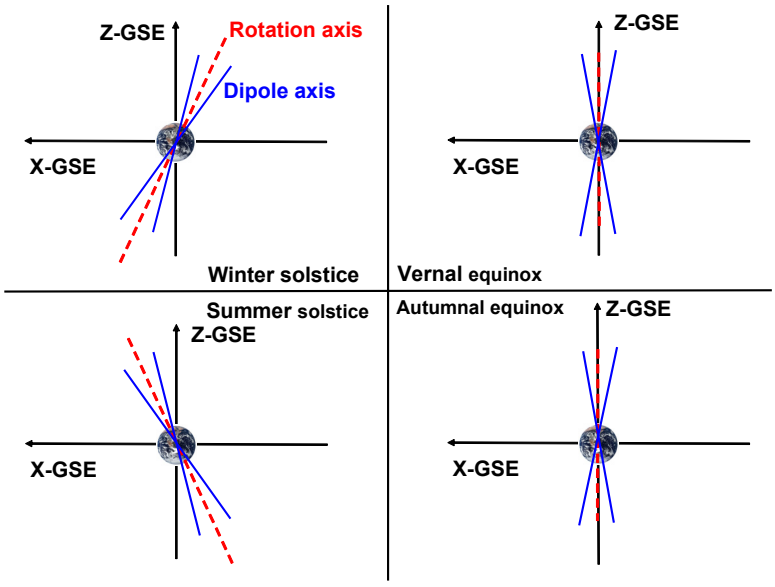

Figur 5.2: *The variation of the dipole axis in the GSE xz-plane*

As can be seen in Figure 5.2, the variation of the dipole axis relative to the GSE z-axis will be at a maximum during summer and winter solstice and at a minimum during the two equinoxes. There are also similar variations in the GSE yz-plane.

5. 1.3. Geocentric Solar Magnetic, GSM

The GSM coordinate system has the same x-axis as the GSE coordinate system but the GSM y-axis is perpendicular to the Earth's dipole axis. This eliminates the variation in the GSE yz-plane. It means that the GSM z-axis is parallel to the projection of the Earth's dipole axis in the GSE yz-plane and that the y-axis is in the magnetic equatorial plane (see Figure 5.3). The GSM coordinate system was first proposed by Ness [1965] and has been widely used to describe magnetospheric boundaries and regions.

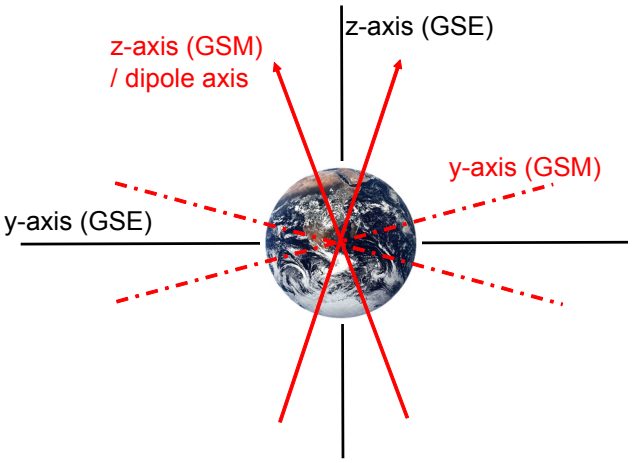

Figur 5.3: *The relationship between the GSE and the GSM coordinate system.*

Hapgood [1992] has developed a guide for space physics coordinate transformation using general theory for rotation of coordinate systems. A matlab code implementing these formulas has been developed to transform GSE-values into GSM coordinates (see "Appendix A")

5. 1.4. Solar Dipole, SD

Variations in the GSE yz-plane are taken into account by using GSM coordinates. The variation in the GSE xz-plane is, however, not corrected for. In order to include the variation of the dipole axis in the GSM xz-plane a coordinate system where the neutral sheet lies in the xy-plane is used. This system is called the solar dipolar coordinate system (SD). In GSM xz-plane the neutral sheet will have a motion parallel to the GSM z-axis. Because of the diurnal variation in the dipole tilt angle the neutral sheet will have a similar diurnal variation in the change of distance relative to the GSM x-axis. The new axes will be parallel to the GSM axes but with a displacement along the z-axis (Z_N) relative to the diurnal and annual variation of the dipole axis in the GSM xz-plane (see Figure 5.4). The SD z-axis equals the GSM z-axis when the dipole tilt angle is zero.

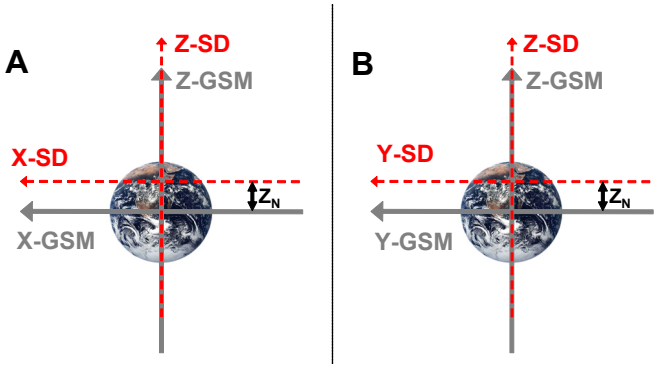

Figur 5.4: *The variation of the SD system in the GSM system. Z_N can be both positive or negative corresponding to a SD xy-plane above or below the GSM xy-plane respectively.*

This coordinate system is called the solar dipole (SD) system. In these coordinates the neutral sheet will always lie in the xy-plane and when a satellite crosses the PSBL the satellite SD z-position will give the half thickness of the plasma sheet.

In order to use these coordinates a relation between the variation in the dipole axis and the neutral sheet position has to be established. This will be discussed below.

5. 2. Neutral sheet position

5. 2.1. The neutral sheet hinge point

Knowing the configuration of the neutral sheet is important for finding its position. Close to the Earth the neutral sheet is considered to be in the plane of the magnetic equator. With increasing distance from Earth the effect of the solar wind gets stronger. At a point the solar wind flow will control the neutral sheet and it is bent away from the magnetic equator and becomes almost parallel to the tail GSM x-axis. The distance from the Earth to the bend point where the neutral sheet no longer follows the magnetic equator is called the distance to the hinge point (D_H)

The idea that the neutral sheet has a hinge point was first proposed by Murayama [1966]. Later several studies have tried to find the distance to this hinge point (e.g., Russel and Broady,1967; Fairfield,1980; Dandouras,1988; Tsyganenko et al.,1998; Tsyganenko and Fairfield, 2004). In the early magnetic field models developed by Tsyganenko, a method for determining the neutral sheet position above the GSM xy-plane was used. This method has been further developed, and now contains dependency on solar wind parameters [Tsyganenko and Fairfield, 2004]. Equation 5.1 is taken from [Tsyganenko and Fairfield, 2004] and gives the height, Z_N, of the neutral sheet above the ecliptic.

$$Z_N = -X\tan\psi^* - \left(G_0 + G_1\frac{X}{10}\right)\left(\frac{|Y|}{15}\right)^3 \sin\psi + S\frac{|X|}{10}\frac{Y}{15}\frac{B_y}{5} \qquad (5.1)$$

Z_N can be calculated for every x and y position in the tail. ψ is the dipole tilt angle, ψ^* is the "effective" tilt angle (see next paragraph) and B_y is the IMF y-component. X, Y

and B_y are normalized with characteristic values. The coefficients G_o, G_1 and S are empirically determined and then corrected for solar wind pressure and IMF conditions.

The "effective" tilt angle equals the dipole tilt angle at the surface of the Earth and decreases as the distance from the Earth increases. Between Earth and the hinge point, the "effective" tilt angle is close to the dipole tilt angle. Beyond this point, the "effective" tilt angle will decrease more rapidly with distance, resulting in a nearly constant height above the GSM xy-plane. The radial distance to the hinge point, R_H have been empirically determined from minimum error analysis [Tsyganenko and Fairfield, 2004].

The first term in Equation 5.1 is related to the dipole tilt effect on the neutral sheet position. The last two terms in this equation are due to a wrapping effect (concave shape) in the GSM yz-plane and a twist effect around the tail axis caused by the IMF B_y component respectively. Since the two last terms have largest effect for large y-positions, they will for simplicity not be taken into consideration in this study. The data that will be used in this thesis therefor have to be concentrated around midnight MLT to limit the effects that occur at large y-positions. Leaving out the last two terms gives:

$$Z_N = -X\tan\psi^* \qquad (5.2)$$

Assuming a constant height between the neutral sheet and the GSM xy-plane beyond the hinge point, it will be enough to calculate the height above the GSM xy-plane, Z_N, at x = D_H. Since the neutral sheet follows the magnetic equator up to this point, the "effective" tilt angle can be replaced with the dipole tilt angle, θ. The x-position of the hinge point is negative and the term, '-x' in Equation 5.1 can be expressed as D_H. This gives a new equation:

$$Z_N = D_H\tan\theta \qquad (5.3)$$

where the parameters in the equation are illustrated in Figure 5.5.

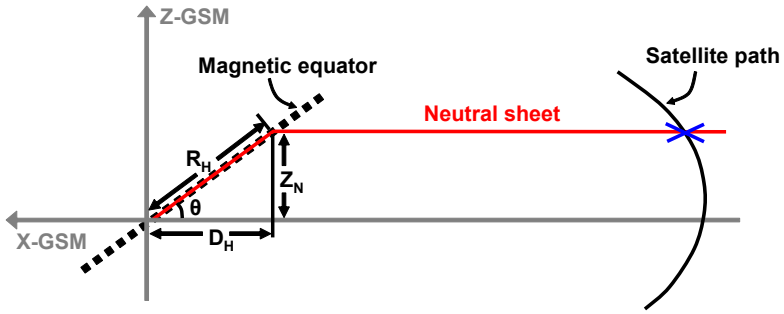

Figur 5.5: *A sketch showing the relation between the dipole tilt, θ, the height of the neutral sheet above the ecliptic, Z_N, and the x-component of the hinging distance, D_H.*

Tsyganenko and Fairfield [2004] have used the radial distance to the hinge point, R_H. This parameter was made dependent on solar wind pressure, P and IMF z-component, B_z. They have also used the characteristic values P_o = 2nPa and B_{zo} = 5nT to normalize P and B_z respectively. Setting P = P_o and B_z = B_{zo} gives a R_H value of $8.75R_E$. Decomposing R_H with a dipole tilt angle of 35 degrees (maximum angle) this results in a x-position of $7.17R_E$. With a zero dipole tilt angle the x-position equals the R_H value. In

this study D_H is referred to as the hinging distance (the x-component of R_H). An average value of D_H will later be used to determine the neutral sheet z-position each time Cluster encounters the PSBL.

An approximation for the distance, D_H, can be found by using Equation 5.3. The height of the neutral sheet above the ecliptic is measured by satellite passages, assuming that the neutral sheet follows a straight line from the hinge point to the satellite passage (the blue cross in Figure 5.5). When the satellite crosses the neutral sheet, the z-position is measured in GSE coordinates and transformed into GSM coordinates. The Z_N-value equals the GSM z-value of the neutral sheet crossing. The assumption that the neutral sheet follows a straight line may not be correct, but gives a good approximation in most cases. Tsyganenko et al. [1998] have found that the distance between the neutral sheet and the ecliptic is nearly constant up to x ~ $100R_E$. Since the Cluster orbit never exceeds x = $-20R_E$ this assumption will be used.

5. 2.2. Neutral sheet passages

In order to identify a neutral sheet passage, the x-component of the Earth's magnetic field is used. The neutral sheet is defined as the plane where the B_x component change polarity. When Cluster passes through the tail (from positive to negative GSE-z) the B_x will change sign from positive to negative. Figure 5.6 shows a clear neutral sheet passage at
05:00 UT on September 22. - 2001, indicated by an arrow in the top panel. The red, dotted line in the figure shows where B_x is zero. In this case the neutral sheet is crossed close to the xy-plane at x = $-18.4R_E$, y = $5.9R_E$, and z = $0.7R_E$.

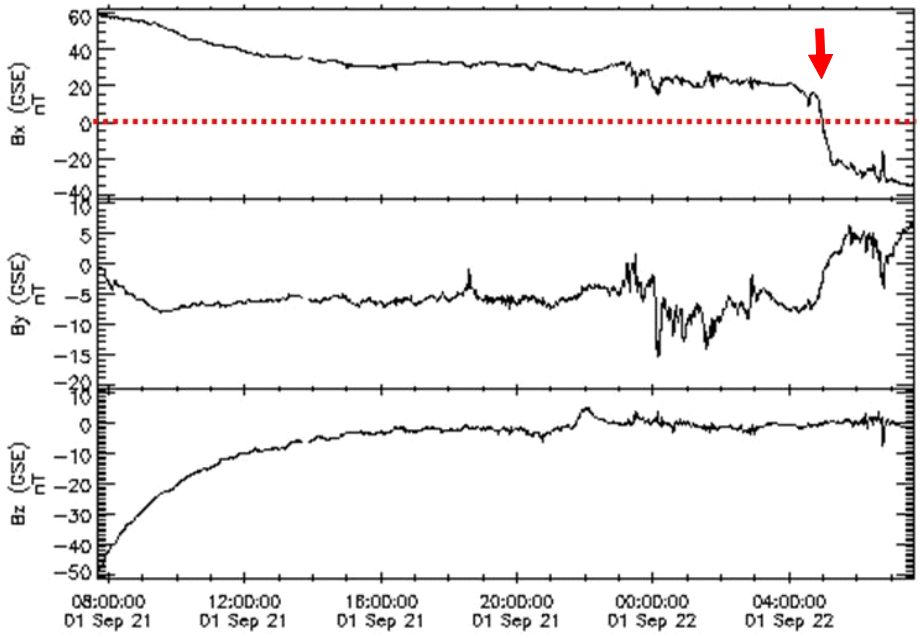

Figur 5.6: *Earth magnetic field measured by Cluster. A tail crossing September 21. - 2001. One clear passage through the neutral sheet can bee seen at about 05:00 (UT). (Image provided by CDA-web)*

Figure 5.6 shows an example of a well defined neutral sheet crossing. Other days the passage is more complex such as demonstrated in Figure 5.7. Here the tail is disturbed, and the neutral sheet moved back and forth over the satellite. In order to define passages on disturbed days like this, two criteria are set; a change in the B_x has to last for minimum 5 minutes or have an amplitude, ΔB_X greater than 15nT. With these criteria the tail passage in Figure 5.7 has 15 neutral sheet crossings (see vertical lines) between 16:30 UT on October 1 - 2003 and 03:30 UT on October 2. - 2003. The criteria mentioned above also block out rapid tail flapping and oscillations which are not relevant for this study. The latter will be discussed closer in the next chapter.

On the day shown in Figure 5.7, Cluster first encounters the neutral sheet at about x = -15.8R_E, y = 5.1R_E and z = 3.7R_E. In the time between 16:30 and 20:00 the satellite stay close to the neutral sheet. Since Cluster moves about 4km in the z direction during this time period, the neutral sheet has to move with the satellite at almost the same velocity. The same seems to happen between 02:00 and 03:30. The last neutral sheet entry appears at x = -16.7R_E, y = 8.9R_E, z = -2.7R_E. In the time period between 20:00 and 02:00, the neutral sheet appears to move rapidly up and down in the z-direction. This flapping occurs when Cluster is between -16.2R_E and -16.9R_E in the x-direction, 6.7R_E and 8.5R_E in the y-direction, 1.7R_E and -1.5R_E in the z-direction.

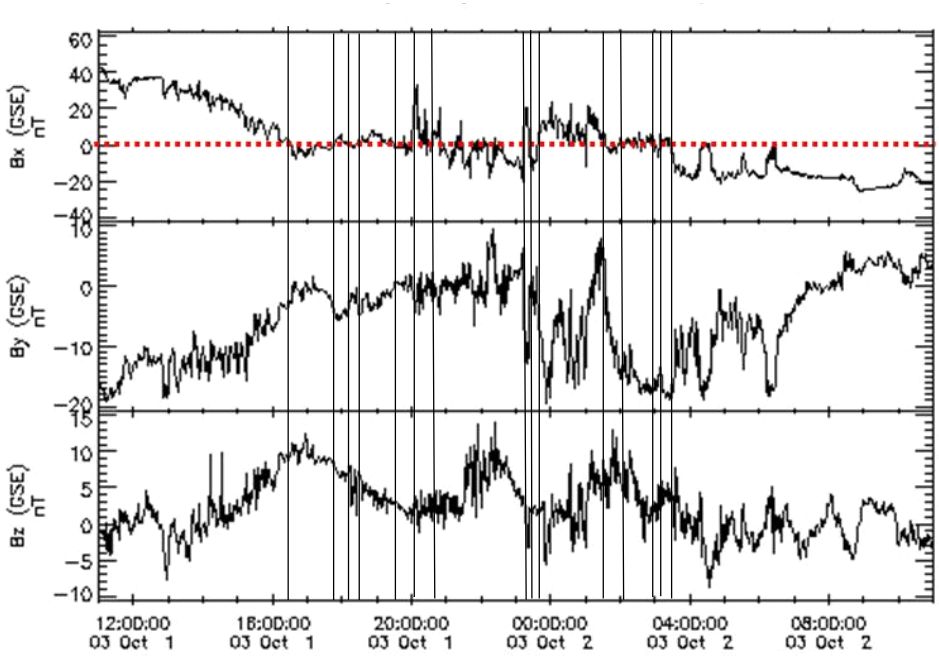

Figur 5.7: *Earth magnetic field measured by Cluster. A tail crossing October 2.-3. - 2003. 15 crossings through the neutral sheet can be observed during this tail passage. (Image provided by CDA-web)*

5. 2.3. Hinge distance, D_H

Cluster orbit the tail during late summer / autumn. In this study the data set is limited to measurements made between ±15 degrees from midnight MLT. This results in a maximum y-position of ±5 R_E at x = -19 R_E. With this limit, data from August and September can be used. Collecting data from 2001 to 2004 results in 69 tail passages.

Some of the tail passages do not have continuos data. Leaving those out results in 55 tail passages. During these 55 tail passages, Cluster encounters 146 neutral sheet crossings.

The z-position of the satellites and the corresponding dipole tilt angle are found for each neutral sheet crossing. These parameters are then used to calculate the hinging x-position for each crossing. Figure 5.8 shows a normalized distribution of the hinge distance and tells how often a certain distance appears in the data set. The mean value of D_H is $9.93R_E$ and the median is $7.0R_E$. The difference between these values is caused by some extremely high D_H-values.

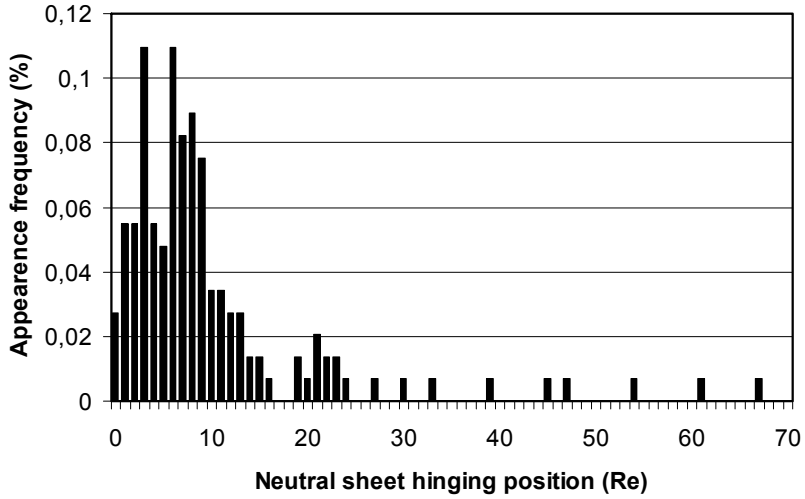

Figur 5.8: *Occurrences of calculated neutral sheet hinge point positions along the x-axis. Median value at 7Re*

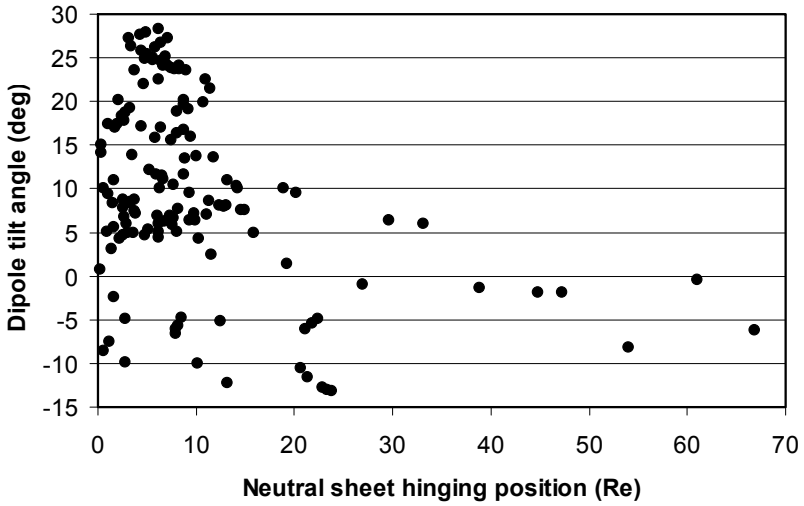

Figur 5.9: *The dipole tilt angle compared to the neutral sheet hinging distance. Except for some large values in the position of the hinge point for small angles, the positions are well distributed over the different angles.*

In Figure 5.9 the hinge distance is compared with the dipole tilt angle. The figure shows that D_H-values up to $19R_E$ occur at all angles but distances $>30R_E$ only occur for small dipole tilt angles. The geometry used to calculate the distance to the hinge point will in some cases not be correct. The largest hinge distances indicate that Cluster crosses the neutral sheet closer to Earth than the position of the hinge point and presented geometry is not correct for this measurements. The high z-values in Figure 5.8 are considered to be outliers because they correspond to small angles and are only confirmed by one measurement. The median value of D_H is not strongly dependent on the large values since there are so few of them but the mean value will be strongly affected. For this reason the median is probably giving the most correct picture of the hinge point distribution and will be used instead of the mean value in the following study.

The median value for the hinge distance in the x-direction is $7.0R_E$. Decomposing the R_H values from Tsyganenko and Fairfield [2004] gives a value between $7.17R_E$ and $8.75R_E$. These values are calculated using the solar wind parameters mentioned above and may be different under other solar wind conditions. For this choice of solar wind parameters, the D_H value in this study is consistent with the findings of Tsyganenko and Fairfield.

One data point is removed from the data set. At this point the D_H-distance reaches 1291 R_E and have a dipole tilt angle at 0.01 degrees. This is as close you get a straight line and no hinge point exist.

Near apogee, Cluster moves at a speed close to 1km/s. With a data time resolution of 1 minute, this gives a general error of $0{,}05R_E$ or 240km. This is an acceptable error compared to the distances discussed above. The total error of the measurements in this study is $1R_E$ and will be discussed later.

5. 3. Method evaluation

To control the method, the neutral sheet positions are calculated on background of the dipole tilt angle and the median value of the neutral sheet hinge point. Figure 5.10 shows the difference between the measured and calculated values. Out of 146 values, 11 has a variance larger than $2R_E$ and 28 lies between $1R_E$ and $2R_E$. The remaining 107 calculations (73% of the data) are within the tolerance of $1R_E$ set for this work.

The calculations that deviate most from the measured values are from early August or late September. This means that the measurements were taken at the largest y-positions allowed in this work. The wrapping effect and the twisting effect mentioned in section 5. 2.1 have larger effect on measurements made at large y-positions. This has not been corrected for. This can be the reason why some of the calculations result in such large deviations.

The twisting effect is controlled by the IMF B_y component. Owen et al. [1995] observed an average tail tilt angle of about 25^o from expected position in the yz-plane. At $x = -19R_E$ and with an angle of 30^o from midnight MLT (meaning that $y = 5\ R_E$ at this x-position) this IMF B_y-effect can cause up to $2.3R_E$ difference from the expected neutral sheet position. The wrapping effect is not that important and can only contribute with $0.7R_E$ deviation at this location.

Orbit 348, between September 30th. and October 1st. causes the largest deviation between the measured and calculated neutral sheet position with a deviation of nearly $7R_E$. This is the same event that caused the high density spot in Figure 4.8, discussed in the previous chapter. Days with extreme events like this makes the statistical analysis difficult and can lead to false conclusions. Thus data from orbits containing the largest variances (orbit 326, 348, 502, 637) circled out in Figure 5.10 will not be used in the further study because of the uncertainty related to them.

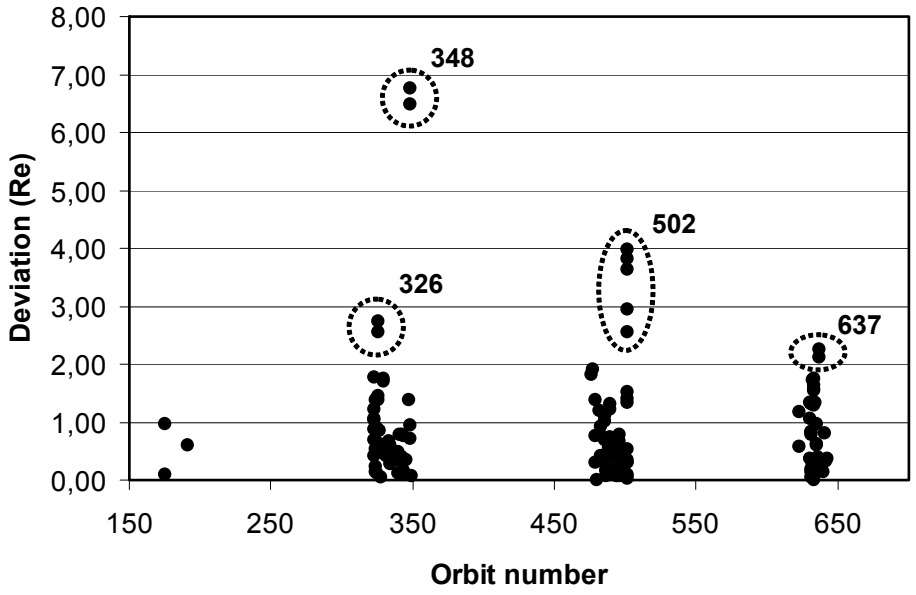

Figur 5.10: *Comparing measured neutral sheet position with calculated position 73% of the data falls within the standard error in this work. This gives good support for the use of this method to calculate the neutral sheet position.*

5. 4. Summary

The neutral sheet position for each crossing of the PSBL was needed in order to find the plasma sheet thickness. Diurnal and annual variations in the dipole tilt angle causes big changes in the neutral sheet position relative to the Earth.

In the GSM system the dipole tilt variation in the GSE yz-plane was eliminated but the diurnal and annual changes in the GSE xz-plane have not been corrected for. In this chapter a method for defining the variation of the neutral sheet position relative to the variation of the dipole tilt angle in the GSE xz-plane has been discussed. The x-component of the hinging distance and the dipole tilt angle have been used to define the neutral sheet position. The distance, Z_N from the GSM xy-plane to the neutral sheet was then used to make a transformation between the GSM and SD coordinate system.

The dipole tilt angle has been used to find the x-distance, D_H to the neutral sheet hinge point. The median of D_H was found to be $7.0 \pm 0.05 R_E$ and was derived from calculations of 146 neutral sheet passages between 2001 and 2004. This is an acceptable

value for the hinge point without too high influence from the high values at small dipole tilt angles. At such small angles, the neutral sheet was close to a straight line and a hinge point does not exist. Compared with the findings of Tsyganenko and Fairfield a hinge distance of $7.0R_E$ is a good estimate.

When the calculated position of the neutral sheet was compared with the measured values, 73% of all the data had a difference less than $1R_E$. Data from orbits with extreme variation caused by tail twisting will not be considered in the further study.

Chapter 6

Plasmasheet thickness

6. 1. Background and objectives

An earlier study aimed to determine the plasma sheet thickness have been carried out with data from Geotail, which has an equatorial orbit. Kaufmann et al.[2001] have used data from 1995 to 1997 to do a statistical mapping of the plasmasheet thickness. They assumed that the plasma sheet is symmetric about the neutral sheet and developed a method to find the natural sheet position relative to the spacecraft. The β-parameter, defined as the particle pressure divided by the magnetic pressure, was used to indicate the satellite distance from the neutral sheet. Ampere's law was then used together with measurements of the magnetic field strength and the tail current density to convert the β-values into z-values. The result gave a half thickness between $2.5R_E$ and $5R_E$ in the midnight tail and on the flanks respectively. The measurements were taken between $10R_E$ and $30R_E$ in the negative x-direction. This method will not be applied in this thesis but the results of the plasma sheet half thickness will be compared with the results from Kaufmann et al.

One of the biggest challenges when determining the plasmasheet thickness is that the tail is not a stable configuration. As Kaufmann et al.[2001] express it: "... neutral sheet is twisted, wrapped and frequently flaps in the z-direction...". This makes it difficult to find out whether a boundary crossing is caused by a change in the plasmasheet thickness or if it is just a flapping motion. A flapping motion can change the neutral sheet position by $1\text{-}2R_E$ within 10 minutes [Kaufmann et al. 2001]. Recently Sergeev et al. [2004] have used Cluster data to do a statistical study of current sheet oscillations. In this study they suggest that a flapping motion in the neutral sheet is caused by waves in the GSM xy-plane that are emitted from the central part of the tail and propagate towards the tail flanks.

Even though this flapping motion can displace the neutral sheet significantly the motion will not be corrected for in this thesis. The reason is that there are no good theories to apply in order to determine when it occurs or to predict the motion. The flapping causes an error in the calculated plasma sheet half thickness of about $0.5R_E$ to $1R_E$. A worst-case situation with an error of $1R_E$ will be assumed in this thesis.

The Cluster orbit covers regions of the magnetosphere at high latitudes where no other spacecraft has operated previously. This makes it possible to sample the crossings of the PSBL at different distances and latitudes. In the late summer and autumn Cluster will always see the plasma sheet near apogee. Before and after apogee, when Cluster is located at larger distances from the neutral sheet, it is possible to observe the number of

PSBL crossings and build up a statistical picture of the number of crossings at different distances and latitudes.

This picture does not take into account tail flapping or wave phenomena near the PSBL. Nevertheless, the procedure gives a new view of the variability of the plasma sheet as will be demonstrated in this chapter. Attempts will also be made to relate this variability with solar wind conditions and dependency of geomagnetic disturbances.

6. 2. Plasma sheet crossings

Depending on the tail conditions, the Cluster satellites encounter the boundary between the plasma sheet and the lobe several times during one tail passage. On some days the time between the first and last crossing can be more than 24 hours. Other days it will only take a few hours to cross the plasma sheet. As mentioned earlier the plasma sheet thickness will be calculated each time Cluster cross the PSBL. By the use of the SD coordinate system the satellite z-position is given relative to the neutral sheet. Since the plasma sheet is assumed to be symmetric about the neutral sheet, the z-position of the satellite in SD coordinates gives the plasma sheet half thickness when the boundary is crossed.

Cluster's orbit makes the satellites cross straight through the plasma sheet and should be ideal for determining the plasma sheet thickness. Using knowledge about the plasma density and energy in the tail lobe and the plasma sheet (see "Chapter 2"), each crossing of the boundary can be timed and positioned.

Density measurements from the EFW instruments in the plasma sheet have large variations which makes it a little more difficult to determine when the satellite crosses the PSBL. The energy flux across the PSBL does on the other hand, provide a very clear identification of the boundary. Data from the CIS instrument on Cluster 3 are used to identify the satellite entries into the plasma sheet. The energy flux calculated from these data have higher values while the satellite is located in the plasma sheet than in the lobe. This provides a clear indication on whether the satellite is inside or outside. In Figure 6.1, the green color indicate that the satellite encounters higher energy fluxes inside the plasma sheet. Dark blue or black indicate that the satellite is in the tenuous plasma of the lobes and outside the plasma sheet.

Figure 6.1a shows an example of a tail passage with many boundary crossings, all marked with red arrows. The multiple crossings indicate that the tail configuration is changing rapidly and that the plasma sheet thickness varies in time. In another example, Cluster 3 only encounters two clear passages as seen in Figure 6.1b. A day like this can be explained in two ways. One possibility is that it is a very calm day with little variation in the tail configuration. Another explanation can be that the variations are outside the view of Cluster. The crossing of the neutral sheet is indicated with a red dotted line in the figure.

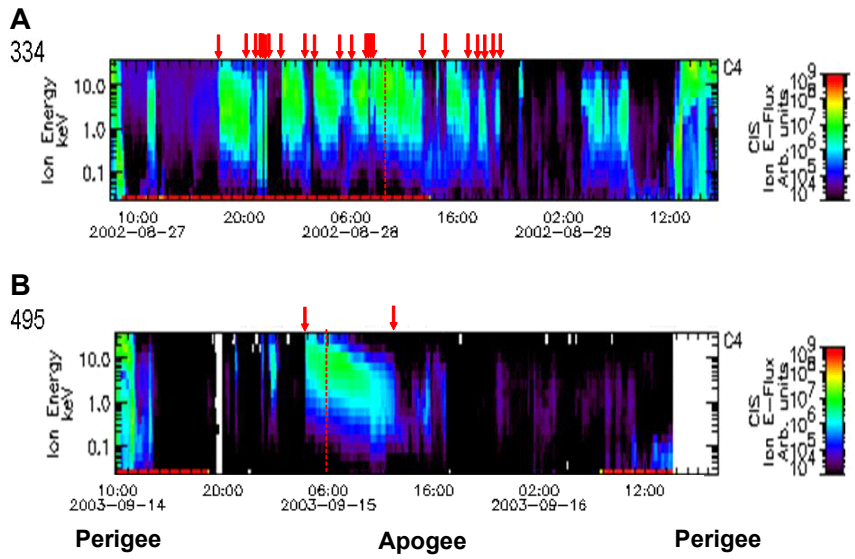

Figur 6.1: *A: CIS data from Cluster orbit 334 with 24 crossings.*
B: CIS data from Cluster orbit 495. This passage have just two crossings.
Plots taken from Cluster Science Data system [CSDS-web]

The thickness of the plasma sheet can only be determined at the time the PSBL is crossed by the satellite. When Cluster 3 is inside the plasma sheet, the half thickness is larger than the distance between the spacecraft and the neutral sheet. If Cluster 3 is in the lobe, the PSBL has to be closer to the neutral sheet than the spacecraft is.

Since Cluster orbits the tail during autumn, data have been collected from all orbits between August and October from 2001, 2002, 2003 and 2004. For some tail passages data are missing and the passages have been excluded from the study (many from 2001). Left are 69 tail passages with 976 plasma sheet crossings. In last chapter, there were some orbits that resulted in a large deviation between the measured and the calculated values for the neutral sheet position. Leaving out the data from these orbits, 921 boundary crossings remain.

The time resolution of the data used is 5 minutes. With a spacecraft speed at about 4km/s near apogee this results in an error of $0.2R_E$ in the position of the plasma sheet crossings. This is well within the $1R_E$ which is the assumed error of this work.

6. 3. Calculating the half thickness

For each boundary crossing ΔZ (Figure 5.4) is calculated in order to transform the satellite coordinates. The dipole tilt angle and the neutral sheet hinge point found in the previous chapter are used to calculate the displacement between the coordinate systems. ΔZ is subtracted from the GSM z-position of the satellite, giving the plasma sheet half thickness. The mean value for the plasma sheet thickness is found to be $4.73R_E$. This value is a little high compared with the findings of Kaufmann et al. [2001] which find a half thickness at the flanks of $5R_E$. The measurements in this study are taken closer to

midnight MLT, and should therefore be closer to $2.5R_E$ according to Kaufmann. The higher value obtained can be explained by the differences between the orbits of the satellites. Cluster can only measure the plasma sheet thickness along its orbit. This means that the PSBL will only be crossed at high z-values when the satellites are close to the Earth. Further out the plasma sheet will be crossed at smaller z-values and result in the sampling of a thinner plasma sheet. This does not mean that the plasma sheet can never be thin close to the Earth, but because of its orbit Cluster will not have measurements in these regions. The best measurement of the plasma sheet thickness will be between x = $-15R_E$ to $19R_E$. The reason for this is that the Cluster satellites move mainly in the z-direction at these distances from Earth. Geotail which orbit close to the equatorial plane will encounter regions closer to Earth when it is closer to the neutral sheet than Cluster satellites. The fact that the satellites take measurements at different distance from the neutral sheet can explain the difference in the average value.

In Figure 6.2 the plasma sheet half thickness is compared with the x-position where the measurement was taken. The figure shows that plasma sheet half thickness smaller than $2R_E$ can only occur from x = $-12R_E$ and out to x = $-19R_E$. Between $-16R_E$ and $-19R_E$ the measured plasma sheet half thickness can take almost all values from zero to $8R_E$. Later the data will be divided into categories depending on the x-position which the measurement was taken at. Measurements made closer to Earth than x = $-15R_E$ will not be included.

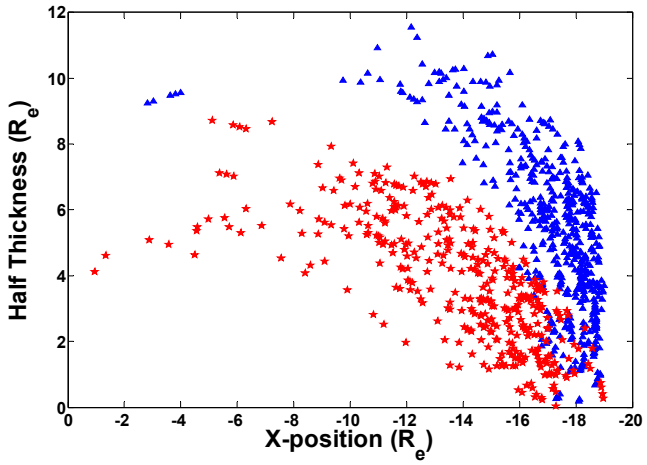

Figur 6.2: *The half thickness of the plasma sheet compared with the distance from earth where it was measured.*

There are two populations of data in the figure. The blue triangles correspond to the measurements made below the neutral sheet (south) and the red stars indicate the measurements made above the neutral sheet (north). The blue population shows larger thickness than the red measurements for all x-positions.The mean thickness for the southern population is $5.4R_E$ while the mean value for the northern part is $3.2R_E$. It appears as if the plasma sheet is thicker below the neutral sheet, but this can be explained by the Cluster orbit.

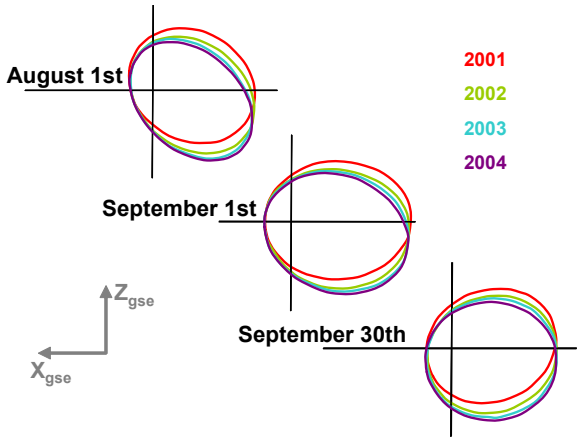

Figur 6.3: *Clusters orbit in the GSE xz-plane from three days during four years.*

As seen in Figure 6.3 the Cluster orbit is not symmetric about the ecliptic. Between August 1st and September 30th the line of apsides is on average a little tilted below the ecliptic. This tilt angle also increases a little each year. From 2001 until 2004 the mean z-position of the neutral sheet will be slightly above the ecliptic. The displacement of the neutral sheet increases the effect of the asymmetric orbit in SD-coordinates. Hence, Cluster take measurements at positions with larger z-values when the satellites are below the neutral sheet than when they are above the neutral sheet. This will result in a smaller measured thicknesses above the neutral sheet than below it, as illustrated in Figure 6.2. Since it is assumed that the plasma sheet is symmetric about the neutral sheet, this orbital asymmetry only gives a better description of the plasma sheet thickness at a certain x-position.

6. 4. Data preparation

The plasma sheet thickness will now be compared with solar wind parameters during quiet and active geomagnetic periods. The aim is to look for data correlating data, which gives an indication of a direct or indirect coupling between the solar wind and the plasma sheet thickness.

6. 4.1. Geomagnetic activity

The data set is first divided into active and non-active geomagnetic periods. The AE-index is used to decide which category the data will be sorted into. A period with low activity is determine by having a mean AE-index no higher than 50nT and a max AE-index no higher than 100nT. These conditions have to start at least 6 hours before the first PSBL crossing and they have to last until the last PSBL crossing of that orbit. This is to ensure that the system is relatively stable and no longer disturbed by earlier substorms. There are 10 orbits that satisfy this criteria, resulting in 122 measurements of the plasma sheet thickness during low activity. The mean plasma sheet half thickness for quiet periods is found to be $5.0R_E$.

An active day is defined by having an average AE-index higher than 500nT and at least one maximum value higher than 1000nT. There is no limit on when these conditions have to start before the satellite first encounters the PSBL. The criteria are satisfied

during 14 orbits which have a total of 212 measurements. The mean value of the plasma sheet half thickness during active periods is found to be $4.4R_E$. Hence, the plasma sheet thickness is about $0.6R_E$ larger during quiet periods. Since the data error in this project is about $1R_E$ this is not considered to be a significant difference.

6. 4.2. ACE and solar wind data

The solar wind influence on the magnetosphere was discussed in "Chapter 2" . In this chapter the following parameters will be compared with the plasma sheet thickness; the solar wind pressure, P_{sw}, the epsilon parameter, ε , the clock angle, θ , the IMF B_z component and the magnitude of the IMF, |B|. In order to do this, 6 solar wind parameters is then needed; the solar wind speed, V and density, N and also the IMF x- y- and z-component, B_x,B_y and B_z and the magnitude, |B|.

Solar wind data are collected from the ACE satellite. ACE is located near the Lagrange point, L1 (point of gravitational equilibrium) between the Sun and the Earth at about $235R_E$ in x-direction. Because of this large distance from the Earth, the solar wind parameters measured by ACE need to be delayed in time in order to compare with changes in the magnetosphere. The time delay is calculated by finding the distance between ACE and the magnetopause and divide this distance with the solar wind speed.

Eriksson et al. [2001] have investigated how long time it takes before the geomagnetic tail reacts on the changes in the solar wind at the magnetopause. In the study they find the time delay by comparing the IMF B_z with the reconnection electric field (similar to the epsilon parameter) and the ASY-H index (a measure of the equatorial disturbance in the earth magnetic field). They then find the time delay that results in highest correlation between the parameters. This results in two maximum in the correlation, one at 35 minutes and one at 65 minutes. The 35 minute response is explained as a directly driven reaction from the solar wind while the 65 minute response belong to release of energy from the tail.

For each PSBL crossing the corresponding solar wind data are found. Since the calculated time delay might not be precise a time average of the data is made. Taking an average over a short time period also limits the effects of small scale changes and rapid variations in the solar wind. Data taken from 10 minutes before a PSBL is crossed to 10 minutes after the crossing gives a 20 minute interval. Such 20 minute interval is found for all the boundary crossings. For each interval, an average value for each of the 6 solar wind parameters is calculated and stored together with the maximum and minimum values at the same interval. The maximum and minimum values are used to determine the variance in the interval. If this variance is too large the average value is not trusted and eliminated from the analysis. The variance limit is chosen to be the mean value of the variance plus two times the standard deviation.

6. 5. Correlation analysis

Correlation coefficients for high AE (cc_{high}) and low AE (cc_{low}) activity are calculated for each solar wind parameter and are listed in Table 6.1. If the correlation coefficient is 1 or -1 the data have a perfect linear correspondence. A coefficient of 0 indicates that

there is no linear dependence between the two data sets. The correlation coefficient is calculated using standard functions from the MatLab statistical toolbox.

Parameter	cc_{high}	cc_{low}
Pressure	-0.1361	-0.2753
Epsilon	-0.1664	**-0.3094**
IMF |B|	-0.0848	0.2625
IMF B_x	0.0226	0.0800
IMF B_y	0.0575	0.1778
IMF B_z	**0.3092**	**0.4914**
Clock Angle	**-0.3738**	**-0.4210**

Table 6.1: *Correlation coefficients between solar wind parameters and the plasma sheet half thickness. The two columns correspond to high and low geomagnetic activity. In this table a 35 minute time delay between the magnetopause and the tail is used.*

Low geomagnetic activity gives the highest correlation. The reason for this can be that there is a large spread in the plasma sheet thickness during high activity. During low activity the tail is more steady. There is no good correlation between the plasma sheet thickness and IMF |B|, B_x and B_y and the parameters will therefore not be discussed any further.

Solar wind pressure, P

As mentioned in "Chapter 2" the solar wind pressure deform the magnetosphere by compressing the field on the dayside and stretching it into a tail in the nightside. The radius of the geomagnetic tail depends on the solar wind pressure. It is therefore expected that high pressure results in a small plasma sheet half thickness and that low pressure results in large thicknesses (negative correlation).

The solar wind pressure is calculated from the time delayed ACE-data using Equation 2.8. The calculated correlation coefficient for data taken during low magnetic activity is -0.2753 (see Table 6.1). This is a low correlation and indicates a very week linear connection with the plasma sheet thickness. There is no good correlation between the data in the high activity period. This does not mean that there is no connection between the pressure and the plasma sheet thickness, but the data used in this analysis does not indicate a correlation. A possibility is that internal substorm related processes in the tail also have an influence on the plasma sheet thickness.

Epsilon parameter, ε

The epsilon parameter is calculated from Akasofus' formula given in Equation 2.11. Eriksson et al. [2001] use a variant of this parameter to find the time delay between the solar wind outside of the magnetopause and the geomagnetic activity measured on the Earth. After a reconnection on the dayside, energy builds up in the geomagnetic tail. This energy is then released during a substorm. The amount of energy that enters the

magnetosphere during reconnection may therefore have an effect on the shape of the geomagnetic tail. Comparing the plasma sheet half thickness with the amount of energy that enters the magnetosphere on the dayside does not seem to result in any linear correlation during periods with high AE-index. During low geomagnetic activity there is a correlation of -0.3094. By using the statistical toolbox in MatLab a regression line is calculated. The resulting line shows a nearly horizontal linear correlation which does not provide any useful information. The figure is therefor not included in this thesis.

Solar wind magnetic field, B_z

During periods with negative B_z a reconnection on the dayside magnetopause is likely to occur. The solar wind then transports the newly opened field lines from the dayside magnetosphere to the tail. This leads to an increase in the tail magnetic flux and thus a thinner plasma sheet. As negative B_z leads to thinner plasma sheet a positive correlation is expected. The z-component of the solar wind is plotted versus the plasma sheet half thickness in Figure 6.4. The regression line is calculated using the MatLab statistical toolbox and is shown in black in the same figure.

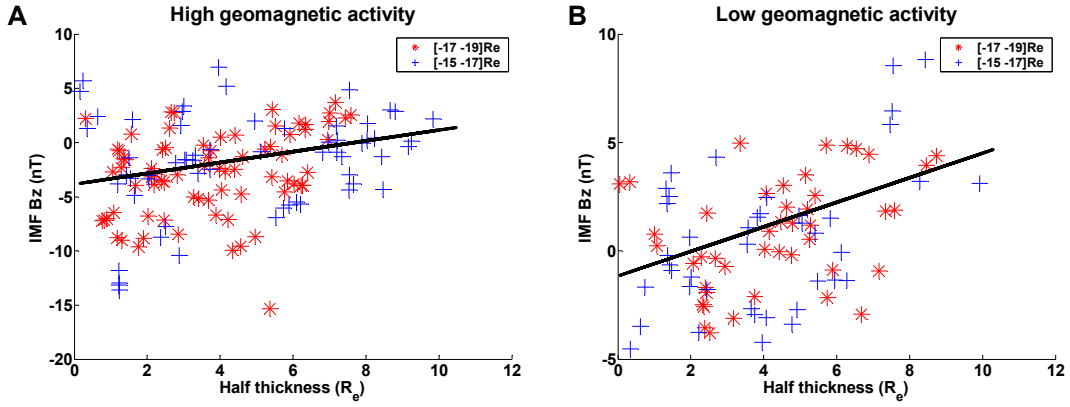

Figur 6.4: *The z-component of the solar wind magnetic field compared with the plasma sheet half thickness*

For low geomagnetic activity the correlation is 0.4914 and for high activity the correlation is 0.3092 (see Table 6.1). The regression line drawn for the high activity period (Figure 6.4a) has a slightly steeper slope than during low activity periods (Figure 6.4b) (note the different scales on the z-axis). The figure shows that the B_z component is more often negative during high magnetic activity. The positive correlation coefficient is in agreement with the expected results. The data will later be divided into positive and negative B_z in addition to the dividing between high and low geomagnetic activity.

Solar wind clock angle, θ

The clock angle is calculated from the B_z and the B_y components of the IMF (see section 2. 3.2). The angle indicates the direction of the magnetic field relative to the GSE z-axis and varies from 0 to 180 degrees. With an angle equal to zero, the magnetic field has no component in y direction and is directed due north along the z-axis. Since the B_z component of the solar wind magnetic field resulted in a relatively good correlation it is

expected that the same is true for the clock angle. Dividing the data into active and non-active periods results in a correlation coefficient of -0.3738 and -0.4210, respectively.

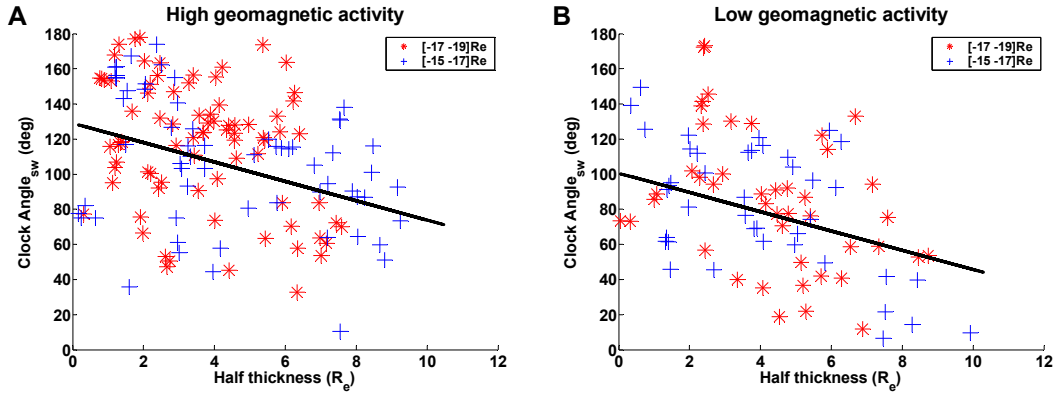

Figur 6.5: *The clock angle of the solar wind magnetic field is compared with the plasma sheet half thickness*

In Figure 6.4a and Figure 6.5a during high geomagnetic activity, the plasma sheet half thickness is smaller at x-positions between -17R_E -19R_E than for x-positions between -15R_E and -17R_E. The measurements taken "outside" the -17R_E range have an upper limit on the plasma sheet half thickness at 7.6R_E. A limit like this can not be observed in the low activity data. This can be understood as periods of low AE are related to northward directed IMF. Less transfer of magnetic flux from dayside to nightside implies less neutral sheet thinning. Also, there appears to be less spread in the data for low AE, which may be consistent with less reconnection/re-configuration

6. 5.1. Positive or negative IMF B_z

As mentioned earlier the data are also divided into positive and negative B_z. During negative B_z the tail is affected by an increase in open magnetic flux and loading of the tail (substorm growth phase). It is therefore expected that measurements with negative B_z have a better correlation than measurements with positive B_z. There is however no evidence of this trend in this data set.

Dividing the positive and negative B_z data further into high and low geomagnetic activity reveals a higher correlation for positive B_z. In Figure 6.6a, the IMF B_z component is plotted against the plasma sheet half thickness measured during periods with low AE-index. The green stars indicate positive IMF B_z and the black ones indicate negative values. The positive IMF B_z show a correlation with the plasma sheet half thickness of 0.3872. Tail flapping causes a large spread in the data and makes it difficult to find better correlation.

After dividing the data into four groups, high and low activity, in addition to positive and negative B_z, a new comparison with the plasma sheet half thickness and the solar wind pressure are preformed. This results in a correlation coefficient of -0.7433 during high activity. A related regression line is drawn in Figure 6.6b. This is the highest correlation found in this thesis. There is also a reason to be careful with the result since calculation

of the correlation is based upon only 12 measurements. If the correlation is true it indicates a strong connection between the solar wind pressure and the plasma sheet thickness when B_Z is positive and the geomagnetic activity is high.

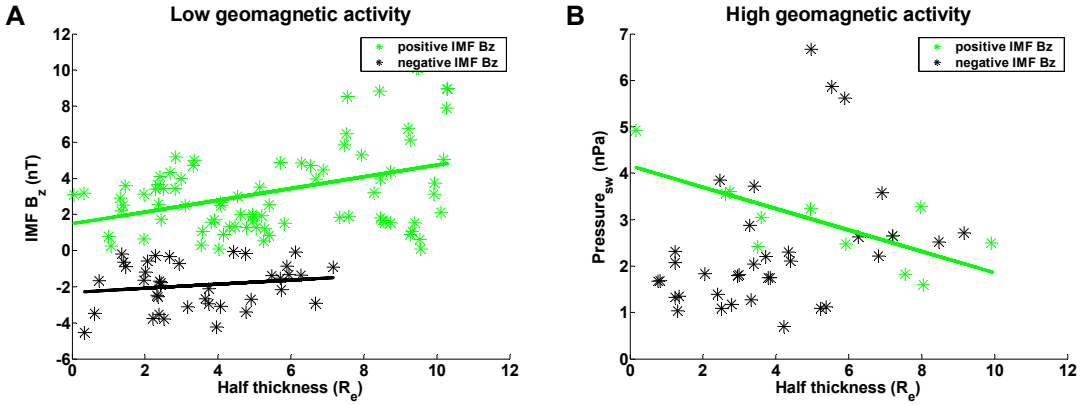

Figur 6.6: *The plasma sheet thickness is divided into periods with positive and negative B_z and is compared with the IMF B_z and the solar wind pressure.*

6. 6. Summary

There has not been done any correction of the data for the current sheet flapping motion. Assuming no flapping gives an error of maximum $1R_E$ which is also the general error in this work.

In this chapter the plasma sheet half thickness has been calculated and the average thickness of $4.73R_E$ has been found. This is a little higher than what has been found in earlier studies [Kaufmann et al., 2001]. A large difference between the thicknesses measured below and above the plasma sheet have been observed and can be explained by the inclination of the Cluster orbit in the GSE xz-plane.

Comparing the plasma sheet thickness with solar wind parameters has revealed a correlation of about 0.5 with the clock angle and the IMF B_Z during both high and low geomagnetic activity. The other parameters do not show any correlation of significance. A possible reason for not finding any higher correlation is that the time delay from the magnetopause to the tail may not be constant. Large variations in the tail configurations and time varying processes can cause a time dependent time delay. The data may therefore not be comparable. It is also possible that there is no direct connection between the solar wind and the plasma sheet configuration. The solar wind may trigger internal processes and which again affects the plasma sheet.

The plasma sheet half thickness have also been divided into positive and negative IMF B_Z and the pressure where again compared with the plasma sheet half thickness. It was expected that the measurements with negative B_Z would give the best correlation but that was not the case. The highest correlation in this thesis was found during high geomagnetic activity for positive B_Z. This correlation was based upon 12 measurements only, which is unreliable.

It was also observed that the plasma sheet half thickness has an upper boundary at x-positions between -17R_E -19R_E than closer to Earth during high activity. This boundary is not present during low geomagnetic activity. A reason may be less current sheet thinning and reconnection in the tail in the low activity periods.

Chapter 7

Summary and conclusions

The aim of this thesis has been to use plasma density and particle measurements from the Cluster spacecraft to identify magnetospheric boundary layers. The intention was to see how magnetospheric boundary layers are influenced by changes in the solar wind.

The spacecraft potential relates to the electron density surrounding the spacecraft. As the spacecraft potential is always being recorded, it is particularly useful for mapping the electron density distribution of the Earth's magnetosphere. Studies making use of the spacecraft potential to measure the plasma density have been carried out earlier, but none of the satellites have been in polar orbit. Cluster has been in orbit since summer 2000 and orbits the Earth in a highly elliptic polar orbit. This has provided the opportunity to obtain data from new regions in the magnetosphere.

First, the relation between the spacecraft potential and the plasma density was established. Thereafter, two and a half years of continuous measurements from the EFW instrument on-board Cluster were collected. The data were sorted into $0.67 \times 0.67 \times 0.67 R_E^3$ volume bins where the number of data samples in each bin varied from 10 to 1000. Representing each data bin with an average value of the plasma density, a 3D image of the density distribution in the magnetosphere was obtained. Even though the EFW instrument can not compete with other particle measurements for accurate determination of the plasma density, it is useful to measure gradients and hence monitor magnetospheric boundaries. For example, the magnetopause is a very distinct boundary, separating high density magnetosheath plasma on open flux from low density magnetospheric plasma on closed field lines. The plasmasphere is also very pronounced as a region. In the tail (from $10R_E$-$20\ R_E$) the plasma sheet stays in contrast to the dilute plasma of the lobe. Cluster also has an ideal orbit for observing the high-latitude cusp and this region has been recognized at $z = 6R_E$-$7R_E$.

In the plasma sheet the EFW instrument encounters a large variability in the plasma density which makes it difficult to distinguish whether the satellite crosses the boundary or encounters a local variation. However, the PSBL layer is very well defined by the ion energy flux measured by CIS. Therefore CIS was used to identify the boundary crossing for estimating the plasma sheet thickness. For each boundary crossing the plasma sheet half thickness can be estimated if the neutral sheet position is known. Thus, a method for finding the neutral sheet position has been established. This method requires two assumptions, namely that the plasma sheet is symmetric about the neutral sheet and that the neutral sheet is a nearly straight line after the hinge point (see Figure 5.5).

A Solar Dipolar Coordinate system (SD) was implemented to account for the movement of the neutral sheet. The SD-coordinate system was then used to find the plasma sheet

half thickness for 921 PSBL crossings, resulting in an average half thickness of $4.73R_E$. This result where then compared with the result in the study of Kaufmann et al.[2001]. From Geotail data they found a plasma sheet half thickness of $2.5R_E$ in the midnight sector (MLT) and a half thickness of $5R_E$ on the tail flanks. The average thickness in this study has been calculated from measurements close to the magnetic midnight and is a little higher than the findings of Kaufmann et al. A reason for this could be the difference in the satellite orbits. The Geotail satellite orbits at x-positions between $10R_E$ and $30R_E$ in this period and Cluster on the other hand takes measurements all the way out to $19R_E$ but no further. This may cause a difference in the measured plasma sheet thickness. However, the methods used are also very different. Since Geotail orbits with only a small inclination to the equatorial plane it rarely crosses the PSBL. In order to measure the plasma sheet thickness, Kaufmann et al. used the β-parameter and the tail current density to estimate the distance from the satellite to the PSBL and the neutral sheet. They also assumed that the plasma sheet is symmetric about the neutral sheet. This method has an uncertainty connected to the position of both the PSBL and the neutral sheet. In the present study the outer boundary of the plasma sheet is measured directly and very accurately by CIS for every satellite crossing. This limits the uncertainty to depend mainly on the uncertainty of the neutral sheet position, which is about +/- $1R_E$.

More interesting than the average value of the plasma sheet thickness is however the large spread of data values as seen from Figure 6.2. The spread indicates a very dynamic system, as anticipated. The thickness between x = $-12R_E$ and $-19R_E$ can take any value between $0R_E$ - $12R_E$. With such a large variability it is not obvious if the average value can be a useful parameter to describe the plasma sheet.

The plasma sheet thickness was then compared with solar wind parameters. First the data were divided into periods with high and low AE-index. This resulted in correlation coefficients with a maximum of 0.4914. The best correlation was found with IMF B_Z and the solar wind clock angle. This is, however, a complex and highly dynamic system, and tail dynamics described by the change in plasma sheet thickness may also be governed by internal processes of the magnetosphere rather than directly driven by the solar wind.

7. 1. Ideas for further work

In order to make it possible to compare the plasma density distribution with solar wind parameters more measurements are needed. When the analysis was carried out, only two and a half years of data were available. This means that many bins just had cover from two different orbits. If there were special conditions during one orbit this would have had great influence on the statistics. This was demonstrated in Chapter 4. Now there exist four and a half years of data which will make a much better material for a statistical study. There has not been time to implement the latest data in this study.

The statistical analysis of the plasma sheet thickness consisted of a relatively large data set. A natural step is to do a detailed inspection of a selection of data to see if the plasma sheet thickness / tail dynamics is directly driven by the solar wind or not. Such a study will make it possible to better understand the dynamic processes in the solar wind-magnetospheric-ionospheric system.

The method for finding the neutral sheet position was controlled by comparing measurements with calculated values. In this method the neutral sheet has been assumed to be parallel to the x-axis beyond the hinge point. A comparison with results from Tsyganenko's and Fairfield's [2004] model would give a indication of how good this assumption is.

A last suggestion for improvements would be to find a model to correct for tail flapping motion to lower the uncertainty. This is not a straight forward task to do and would probably be enough work for a new thesis project.

Bibliography

Akasofu S.-I., (**1981**), Energy coupling between the solar wind and the magnetosphere, *Space Science Review*, 28, p. 121

Arnoldy R.L., (**1971**), Signature in the interplanetary medium for substorms, *J. Geophys. Res.*, 76(22), p. 5189

Asano Y, T.Mukai, M.Hoshino, Y.Saito, H.Hayakawa, T.Nagai, (**2004**), Statistical study of thin current sheet evolution around substorm onset, *J. Geophys. Res*., 109(A05213), doi:10.1029/2004JA010413,

Baker D.N., T.I.Pulkkinen, V.Angelopoulos, W.Baumjohann, R.L.McPherron, (**1996**), Neutral line model of substorms: Past results and present view, *J. Geophys. Res.*, 101(A6), p. 12975

Balogh A., M.W.Dunlop, A.W.H.Cowely, D.J.Southwood, J.G.Thomlinson, K.H.Glassmeier, G.Musmann, H.Lühr, S.Buchert, M.H.Acuña, D.h.Fairfield, J.A.Slavin, W.Reidler, K.Schwingenschuh, M.G.Kivelson, FGM team,(**1997**), The Cluster magnetic field investigation, *Space Science Review*, 79, p. 65

Berchem J., C. T. **Russell**, (**1982**), The Thickness of the Magnetopause Current Layer: ISEE 1 and 2 Observations, *J. Geophys. Res*., 87, p. 2108

Brekke A, (**1997**), The Earth's magnetic field, Physics of the upper polar atmosphere, *John Wiley & sons*, p. 127 - 190

Carroll B.W, D.A.**Ostlie**, (**1996**), The sun, Modern Astrophysics, *Addison-Wesley publishing company*, p. 381 - 436

Chen F.F.,(**1984**), Introduction to plasma physics and controlled fusion - second edition, *Kluwer Academic / Plenum Publishers*, p. 1-17

Cluster-II Project Team, (**2000**), The Cluster-II mission rising from the ashes, *ESA bulletin,* 102(May), p. 46

Coroniti F.V., C.F.**Kennel**, (**1972**), Changes in magnetospheric configuration during the substorm growth phase, *J. Geophys. Res*., 79(19), p. 2811

Cowley S., (**1973**), A qualitative study of the reconnection between the Earth's field and interplanetary field of arbitrary orientation., *Radio Sci.*, 8, p. 903

Daly P.W., (**2002**), Users guide to the Cluster science data system, DS-MPA-TN-0015, [online], Available from: ftp://ftp.estec.esa.nl/pub/csds/task_for/users_guide/csds_guide_1_1.pdf [Accessed 12 May 2005]

Dandouras J.,(**1988**), On the average shape and position of the geomagnetic neutral sheet and its influence on the plasma sheet statistical studies, *J. Geophys. Res.*, 93(A7), p. 7345

Décréau P.E.M., P.Fergeau,V.Krannosels'kikh, M.Lévêque, P.H.Martin, O.Randriamboarison, F.X.Sené, J.G.Trorignon, P.Canu, P.B.Mögensen, Whisper Investigators, (**1997**), WHISPER, A resonance sounder and wave analyzer: performances and perspectives for the Cluster mission, *Space Science Reviews*, 79, p.157

Eriksson S., L.G.Blomberg, N.Ivchenko, T.Karlsson, G.T.Marklund, (**2001**), Magnetospheric response to the solar wind as indicated by the cross-polar potential drop and the low-latitude asymmetric disturbance field, *Ann. Geophysicae*,19, p. 649

Escoubet, C.P., R.Schmidt, M.L.Goldstein, (**1997**), Cluster – science and mission overview, *Space Science Reviews*, 79, p. 11-32

Escoubet C.P.,(**2000**), Cluster-II: Scientific objectives and data dissemination, *ESA bulletin*, 102(May), p. 54

Escoubet, C.P., M,Fehringer, M. Goldstein, (**2001**), The Cluster mission, *Ann. Geophysicae*,19, p. 1179

Fairfield D.H., (**1980**), A statistical determination of the shape and position of the geomagnetic neutral sheet, *J. Geophys. Res*., 85, p. 775

Freedmann R.A., W.J.**Kaufmann** III, (**2001**), Our star, the sun, Universe - sixth edition, *W.H.Freeman*, p. 389 - 418

Haaland S.E., B.U.Ö.Sonerup, M.W.Dunlop, A.Balogh, E.Georgescu, H.Hasegawa, B.Klecker, G.Paschmann, P.Puhl-Quinn, H.Rème, H.Vaith, A.Vaivads, (**2004**), Four-spacecraft determination of magnetopause orientation, motion and thickness: comparison with results from single-spacecraft methods, *Ann. Geophysicae*, 22(4), p. 1347

Hammond C.M.,M.G.Kivelson, R.J.Walker, (**1994**), Imaging the effect of dipole tilt on the magnetotail boundaries, *J. Geophys. Res.*, 99(A4), p. 6079

Hapgood M.A., (**1992**), Space Physics Coordinate Transformations: A User Guide, *Planet. Space Sci., 40 (5)*, p. 711

Hughes W.J., (**1995**), The magnetopause, magnetotail and magnetic reconnection, Introduction to space physics, edited by M.G.Kivelson and C.T.Russel, *Cambridge University Press*, p. 227 - 287

Gustafsson G., R.Bostöm, B.Holback, G.Holmgren, A.Lundgren, K.Stasiewicz, L.Åhlén, F.S.Mozer, D.Pankow, P.Harvey, P.Berg, R.Ulrich, A.Pedersen, R.Schmidt, A.Butler, A.W.C.Fransen, D.Klinge, M.Thomsen, C.-G.Fâlthammar, P.-A.Lindquist, S.Chritenson, J.Holtet, B.Lybekk, T.A.Sten, P.Tanskanen, K.Lappalainen, J.Wygant, (**1997**), The electric field and wave experiment for the Cluster mission., *Space Science Reviews,* 79, p.137

Hundhausen A.J., (**1995**), The solar wind, Introduction to space physics, *Cambridge University Press*, edited by M.G.Kivelson and C.T.Russel, p. 91 - 128

Kaufmann R.L., B.M.Ball, W.R.Paterson, L.A.Frank, (**2001**), Plasma sheet thickness and electric currents, *J. Geophys. Res*., 106(A4), p. 6179

Laakso H., R.Pfaff, P.Janhunen, (**2002**) Polar observations of electron density distribution in the Earths magnetosphere. 2. Density profiles, *Ann. Geophysicae*, 20, p. 1725

Li L., R.L**.Xu**, (**2000**), A neutral sheet surface observed on ISEE-2, IMP-8, AMPTE/IRM, and INTERNBALL satellites, *Geophys. Res. Lett.*, 27, p. 855

Lui A.T.Y., (**1996**), Current disruption in the Earth's magnetosphere: Observations and models, *J. Geophys. Res.*, 101(A6), p. 13067

Manchester W.B., I.V.Tamas, I.Gombosi, I.Roussev, A.Ridley, D.L.DeZeeuw, I.V.Sokolov, K.G.Powell, (**2004**), Modelling a space weather event from the sun to the Earth: CME generation and interplanetary propagation., *J. Geophys. Res*., 109(A2), doi:10.1029/2003JA010150

McPherron, R.L., (**1995**), Magnetospheric dynamics, Introduction to space physics, edited by M.G.Kivelson and C.T.Russel, *Cambridge University Press*, p. 400 - 458

Mitchell D.G.,G.J.Williams, C.Y.Huang, L.A.Frank, C.T.Russell, (**1990**), Current carriers in the near-Earth cross-tail current sheet during substorm growth phase, *Geophys. Res. Lett.*, 17, p. 583

Moore D.S., G.P.**McCabe**, (**1999**), Inference for regression, Introduction to the practice of statistics: 3rd-ed., *W.H.Freeman and Company*, p. 661-710

Murayama T., K. **Hakamada**, (**1975**), Effects of solar wind parameters on the development of magnetospheric substorms, *Planet. Space Sci*., 23, p. 75

Nakamura R., W.Baumjohann, A.Runov, M.Volwerk, T.L.Zhang, B.Klecker, Y.Bogdanova, A.Roux, A.Balogh, H.Rème, J.A.Sauvaud, H.U.Frey, (**2002**), Fast flow during current sheet thinning, *Geophys. Res. Lett.*, 29(23), p. 2140

Ness N.F., (**1965**), The Earth's Magnetic Tail, *J. Geophys. Res*., 70(13), p.2989

Owen C.J., J.A.Slavin, I.G.Richardson, N.Murphy, R.J.Hynds, (**1995**), Average motion, structure and orientation of the magnetotail determined from remote sensing of the edge of the plasma sheet boundary layer with E > 35 keV ions, *J. Geophys. Res*., 100(A1), p. 185

Parker E.N., (**1958**), Dynamics of the interplanetary gas and magnetic fields, A*strophysical journal,* 128(3), p. 664

Pécseli H.L., (**2001**), Magneto-hydrodynamics by brute force, Selected Topics in Plasma Physics - lecture notes, version: Sept. 27 - 2001, p. 85 - 108

Pedersen A., P.Decreau, C.P.Escoubet, G.Gustafsson, H.Laakso, P.-A.Lindqvist, B.Lybekk, A.Masson, F.Mozer, A.Vaivads, (**2001**), Four-point high time resolution information on electron densities by the electric field experiments (EFW) on Cluster., *Annales Geophysicae*, 19(10/12), p. 1483

Peredo, M., J. A.Slavin, E.Mazur, S. A.Curtis, (**1995**), Three-dimensional position and shape of the bow shock and their variation with Alfvenic, sonic and magnetosonic Mach numbers and interplanetary magnetic field orientation, *J.Geophys. Res*., 100(A5), p. 7907

Priest E.R., (**1995**), The sun and its magnetohydrodynamics, Introduction to space physics, edited by M.G.Kivelson and C.T.Russel, *Cambridge University Press*, p. 65 - 90

Pulkkinen T. I., D.N.Baker, D.G.Mitchell, R.L.McPherron, C.Y.Huang, L.A.Frank, (**1994**), Thin current sheets in the magnetotail during substorms: CDAW 6 revisited *J. Geophys. Res*., 99(A4), p. 5793

Rème H., J.M.Bosqued, J.A.Sauvaud, A.Cros, J.Dandouras, C.Aoustin, J.Bouyssou, Th.Camus, J.Cuvilo, C.Martz, J.L.Médale, H.Perrier, D.Romefort, J.Rouzaud, C.d'Uston, E.Möbius, K.Crocker, M.Granoff, L.M.Kistler, M.Popecki, D.Hovestadt, B.Klecker, G. Paschmann, M.Scholer, C.W.Carlson, D.W.Curtis, R.P.Lin, J.P.McFadden, V.Formisano, E.Amata, M.B.Bavassano-Cattaneo, P.Baldetti, G.Belluci, R.Bruno, G.Chionchio, A.Di Lellis, E.G.Shelley, A.G.Ghielmetti, W.Lennartson, A.Korth, H.Rosenbauer, R.Lundin, S.Olsen, G.K.Parks, M.McCarthy, H.Balsiger, (**1997**), The Cluster ion spectrometry (CIS) experiment, *Space Science Review*, 79, p. 303

Russel C.T., (**1995**), A brief history of solar-terrestrial physics, Introduction to space physics, *Cambridge University Press*, edited by M.G.Kivelson and C.T.Russel, p. 1 - 26

Russel C.T., K.I.Broady, (**1967**), Some remarks on the position and shape of the neutral sheet, *J. Geophys. Res.*, 72, p. 6104

Sanny J., R. L.McPherron, C.T.Russell, D.N.Baker, T.I.Pulkkinnen, A.Nishida, (**1994**), Growth-phase thinning of the near-Earth current sheet during the CDAW 6 substorm *J. Geophys. Res.*, 99(A4), p. 5805

Sergeev V., D.G.Mitchell, C.T.Russell, D.J:Williams, (**1993**), Structure of the tail plasma/current sheet at ~11 R_E and its changes in the cause of a substorm, *J. Geophys. Res.*, 98(A10), p. 17345

Sergeev V., A. Runov, W. Baumjohann, R. Nakamura, T. L. Zhang, A. Balogh, P. Louarnd, J.-A. Sauvaud, H.Reme, (**2004**), Orientation and propagation of current sheet oscillations, *Geophys. Res. Lett*., 31, doi:10.1029/2003GL019346

Sibeck D.G., R.E.Lopez, E.C.Roelof, (**1991**), Solar wind control of the magnetopause shape, location, and motion., *J. Geophys. Res.*, 96(A4), p. 5489

Smith E.J., (**2001**), The heliospheric current sheet, *J. Geophys, Res.*, 106(A8), p. 15819

Torkar K.,W.Riedler, C.P.Escoubet, M.Fehringer, R.Schmidt, R.J.L.Grard, H.Arends, F.Rüdenauer,W.Steiger, B.T.Narheim, K.Svenes, R.Torbert, M.André, A.Fazakerley, R.Goldstein, R.C.Olsen, A.Pedersen, E.Whipple, H.Zhao, (**2001**), Active spacecraft potential control for Cluster – implementation and first results, *Ann. Geophysicae*, 19, p. 1289

Tsyganenko N.A., S.B.P.Karlson, S.Kokubun, T.Yamamoto, A.J.Lazarus, K.W.Oglivie, C.T.Russel, (**1998**), Global configuration of the magnetotail current sheet as derived from Geotail, Wind, IMP 8 and ISEE 1/2 data, *J. Geophys. Res*, 103, p. 6827

Tsyganenko N.A., D.H.**Fairfield** (**2004**), Global shape of the magnetotail current sheet as derived from Geotail and Polar data, *J. Geophys. Res*, 109 (A03218), doi:10.1029/2003JA010062

Walker R.J., C.T.**Russell**, (**1995**), Solar wind interaction with magnetized planets, Introduction to space physics, edited by M.G.Kivelson and C.T.Russel, *Cambridge University Press*, p. 164 - 182

Wolf R.A.,(**1995**), Magnetospheric configuration, Introduction to space physics, edited by M.G.Kivelson and C.T.Russel, *Cambridge University Press*, p. 288 - 329

Zeilik M**.,** S.A.**Gregory**, (**1998**), The sun; A model Star, Introductory Astronomy & Astrophysics (4.ed), *Harcourt Brace College Publishers*, p. 200-223

Østgard N., G.Germany, J.Stadsnæs, R.R.Vondrak, (**2002**), Energy analysis of substorms based on remote sensing techniques, solar wind measurements, and geomagnetic indices, *J. Geophys. Res*., 107(A9), doi:10.1029/2001JA002002, p. 1233,

Figure references

Brekke A, (**1997**), The solar wind and the interplanetary magnetic field, Physics of the upper polar atmosphere, *John Wiley & sons*, p. 55

Carroll B.W, D.A.**Ostlie**, (**1996**), The sun, Modern Astrophysics, *Addison-Wesley publishing company*, p. 424

Cluster-II Project Team, (**2000**), The Cluster-II mission rising from the ashes, *ESA bulletin,* 102(May), p. 46

ESA-Cluster, (**2003**), ESA Science and Technology: Artist's impression of the Cluster spacecraft, [online], Available from: http://esamultimedia.esa.int/images/Science/Clusters_Earth2.jpg [Accessed 26 May 2005]

Lang K.R., (**2003**), Nasa's Cosmos: Long Thin Loops Heated from their Base, [online], Tufts University, Available from: http://ase.tufts.edu/cosmos/view_picture.asp?id=155 [Accessed 26 May 2005]

NASA's Cosmicopia (**2005**), The Earth's Magnetosphere, [online], Available from: http://helios.gsfc.nasa.gov/magnet.html [Accessed 26 May 2005]

Pedersen A., P.Decreau, C.P.Escoubet, G.Gustafsson, H.Laakso, P.-A.Lindqvist, B.Lybekk, A.Masson, F.Mozer, A.Vaivads, (**2001**), Four-point high time resolution information on electron densities by the electric field experiments (EFW) on Cluster., *Annales Geophysicae*, 19(10/12), p. 1483

Richard Fitzpatrick, (**2002**), Introduction to Plasma Physics, [online], University of Texas, Available from: http://farside.ph.utexas.edu/teaching/plasma/lectures/node77.html [Accessed 26 May 2005]

SOHO: Pick of the week, (**2002**), A coronal hole streaming solar wind, [online], Available from: http://sohowww.nascom.nasa.gov/pickoftheweek/old/12sep2002/index.html [Accessed 26 May 2005]

SOHO, (**2005**), Best of SOHO Images and Movies, [online], Available from: http://sohowww.nascom.nasa.gov/bestofsoho/ [Accessed 26 May 2005]

Spaceflight Now, (**2005**), Cluster II: Studying the Sun-Earth connection, [online], Pole Star Publications Ltd., Available from: http://spaceflightnow.com/cluster2/000714feature/index5.html [Accessed 26 May 2005]

Abbreviations

ACE - Advanced Composition Explorer
AE - Auroral Electrojet
ASPOC - Active Spacecraft Potential Control
CCI - Cross-field Current Instability
CDA-web - Coordinated Data Analysis-web
CIS - Cluster Ion Spectrometry
CME - Coronal Mass Ejections
CODIF - ion COmposition and DIstribution Function analyzer
EFW - Electron Field and Wave experiment
EDI - Electron Drift Instrument
ESA - European Space Agency
FFT - Fast Fourier Transform
FGM - FluxGate Magnetometer
GSE - Geocentric Solar Ecliptic coordinate system
GSM - Geocentric Solar Magnetic coordinate system
HCS - Heliospheric Current Sheet
HIA - Hot Ion Analyzer
IMF - Interplanetary Magnetic Field
ISEE-1 - International Sun-Earth Explorer
MHD - Magneto Hydro Dynamic
MLT - Magnetic Local Time
NASA - National Aeronautics and Space Administration
NENL - Near Earth Neutral Line
PEACE - Plasma Electron And Current Experiment
PSBL - Plasma Sheet Boundary Layer
SD - Solar Dipolar coordinate system
SOHO -SOlar and Heliospheric Observatory
SSC - Sudden Storm Commencement
STSP - Solar Terrestrial Science Program
WDC - kyoto World Data Centre for geomagnetism
WHISPER - Waves of HIgh frequency and Sounder for
Probing of Electron density by Relaxation

Appendix A

Transformation from GSE to GSM coordinates

To make this transformation a transformation through two other coordinate systems is needed; the GEOgraphic system (GEO) and the Geocentric Equatorial Inertial system (GEI). A MatLab source code that perform the transformations described here is included below.

The rotation matrixes used in this work is taken from M.A.Hapgoods "Space Physics Coordinate Transformations: A User Guide" [1992]. Generally a transformation matrix can be described by a rotation angle and the rotation axis, T = <ζ ,A>;

$$<\theta,X> = \begin{bmatrix} 1 & 0 & 0 \\ 0 & \cos\theta & \sin\theta \\ 0 & -\sin\theta & \cos\theta \end{bmatrix}, <\theta,Y> = \begin{bmatrix} \cos\theta & 0 & \sin\theta \\ 0 & 1 & 0 \\ -\sin\theta & 0 & \cos\theta \end{bmatrix}, <\theta,Z> = \begin{bmatrix} \cos\theta & \sin\theta & 0 \\ -\sin\theta & \cos\theta & 0 \\ 0 & 0 & 1 \end{bmatrix}.$$

To transfer from GSE to GSM coordinates you need one transformation matrix, T_3. The rotation angel, ψ is the angle between the GSE z axis and the projection of the magnetic dipole axis on the yz-plane and the rotation axis is the GSE x-axis.

The transformation from GES to GSM coordinates are given by the rotation matrix $T_3 = \langle \Psi, Z \rangle$, where $\Psi = arc\tan\left(\frac{y_e}{z_e}\right)$.

y_e and z_e are given by the unit vector $Q_e = \begin{bmatrix} x_e \\ y_e \\ z_e \end{bmatrix}$ which describe the dipole axis direction in the GSE coordinate system. This vector is normally given in GEO coordinates and we have to do the transformation via GEO and GEI coordinates. This requires two more rotation matrixes; one to transform from GEO to GEI, T_1^{-1} and then from GEI to GSE, T_2.

The rotation matrix from GEI to GEO is rotated about the z-axis; $T_1 = \langle \theta, Z \rangle$, where $\theta = 100,461 + 36000,770 T_0 + 15,04107 UT$ and $T_0 = \frac{MJD - 51544,5}{36525,0}$.

MJD is the Modified Julian Date which is the time measured in days from 00:00 UT on 17 November 1858 (julian date 2400000.5)

The transformation from GEI to GSE consists of one rotation about the z-axis and one about the x-axis; $T_2 = \langle \lambda_S, Z \rangle \times \langle \varepsilon, X \rangle$ where the angles are given by the following equations:

$\varepsilon = 23,439 - 0,013 T_0$, $\lambda_S = \Lambda + (1,915 - 0,0048 T_0)\sin M + 0,020 \sin(2M)$

The parameters M and Λ are given below:
$M = 357,528 + 35999,050 T_0 + 0,04107 UT$,
$\Lambda = 280,460 + 36000,772 T_0 + 0,04107 UT$ and T_0 is already defined above.

The Q_e vector given in GEO coordinates: $Q_g = \begin{bmatrix} \cos\varphi \cos\nu \\ \cos\varphi \sin\nu \\ \sin\varphi \end{bmatrix}$

where φ and ν can be derived from the first order coefficients of the International Geomagnetic Reference Field (IGRF), g_1^0, g_1^1, h_1^1. Using values given in the IGRF for 1985 we get:

$\varphi = 78,8 + 4,283 \times 10^{-2} \left(\frac{MJD - 46066}{365,25} \right)$ and

$\nu = 289,1 - 1,413 \times 10^{-2} \left(\frac{MJD - 46066}{365,25} \right)$.

We then have that $Q_e = T_2 T_1^{-1} Q_g$ and we can calculate Ψ and then T_3

```
function [x_gsm, y_gsm, z_gsm] = gse2gsm( year, month, day, hh, mm, x_gse, y_gse, z_gse)

%Converting from GSE to GSM coordinates

% All equations used refer to the article written by M.A.Hapgood;
% "Space Physics Coordinate Transformations: A User Guide",
% Planetary and Space Science, 1992, vol.40, nr.5, s.711-717


%Modified Julian Date (days since 00:00 UT 17. Nov. - 1858)
MJD = (year-1859)*365.25 + dat2doy([day,month])-1 + 44;
%Universal Time (in hours)
UT  = hh + (mm/60);

% Equation 3
To = (MJD - 51544.5)/36525.0;             % T_theta

% From equation 8 and 9 (coefficients from IGRF - 1985)
Lambda = 289.1 - 0.01413*((MJD - 46066)/365.25);
Fi = 78.8 + 0.04283*((MJD - 46066)/365.25);

% Chapter 4.1
t = 100.461 + 36000.770*To + 15.04107*UT;    % Theta

% Chapter 4.2
E = 23.439 - 0.013*To;   % Epsilon
M = 357.528 + 35999.050*To +0.04107*UT;    % The Sun's Mean Anomaly
A = 280.460 + 36000.772*To +0.04107*UT;    % The Sun's Mean Longitude

% Equation 5
L = (A + (1.915 - 0.0048*To)*sin(M*pi/180) + (0.02*sin(2*M*pi/180)));

% Equation 2
T_1_inv = [cos(t*pi/180),sin(t*pi/180),0; -sin(t*pi/180),cos(t*pi/180),0; 0,0,1]';
% Equation 4
T_2 = [cos(L*pi/180),sin(L*pi/180),0; -sin(L*pi/180),cos(L*pi/180),0; 0,0,1]...
    *[1,0,0; 0,cos(E*pi/180),sin(E*pi/180); 0,-sin(E*pi/180),cos(E*pi/180)];

Qg = [cos(Fi*pi/180)*cos(Lambda*pi/180); cos(Fi*pi/180)*sin(Lambda*pi/180); sin(Fi*pi/180)];
% Equation 7
Qe = T_2*T_1_inv*Qg;

% Chapter 4.3
Ksi = atan(Qe(2)/Qe(3));

% Equation 6
T_3 = [1,0,0; 0,cos(-Ksi),sin(-Ksi); 0,-sin(-Ksi),cos(-Ksi)];

GSM = T_3 * [x_gse; y_gse; z_gse];

x_gsm = GSM(1);
y_gsm = GSM(2);
z_gsm = GSM(3);
```

Appendix B

The Phoenix

In Greek and Roman legends, the Phoenix is the symbol of immortality and resurrection. It is associated with the Sun god Phoebus (Apollo). Its name "Phoenix" is the Greek word for "red", which links this magical bird to fire and the sun. It is said to resemble an eagle or a peacock.

The Greek believed that the Phoenix lived in Arabia, in a cool well. At dawn, each morning, it sung a beautiful song, so beautiful that the Sun god would stop his chariot to listen. The Phoenix is a unique bird, there may only exist one at a time, which makes it a solitary bird. It does not reproduce, which adds to its loneliness, as only its death will bring on another of its race. When it feels its end approaching (between 500 and 1461 years, depending on the legend), it builds a nest with the finest aromatic woods, sets it on fire, and is consumed by his own flames. From the pile of ashes, a new Phoenix arises, young and powerful. It then embalms the ashes of its predecessor in an egg of myrrh, and flies to the city of the Sun, Heliopolis, where he deposits the egg on the altar of the Sun god.

Figur B.1: *The Phoenix*

The following is a text by a Roman author, Claudian, which tells the story of the Phoenix. This poetic version is translated by Henry Vaughan.

THE PHOENIX
He knows his time is out! and doth provide
New principles of life; herbs he brings dried
From the hot hills, and with rich spices frames
A Pile shall burn, and Hatch him with his flames.

On this the weakling sits; salutes the Sun
With pleasant noise, and prays and begs for some
Of his own fire, that quickly may restore
The youth and vigor, which he had before.
Whom soon as Phoebus[1] spies, stopping his rays
He makes a stand, and thus allays his pains.
He shakes his locks, and from his golden head,
Shoots on bright beam, which smites with vital fire

The willing bird; to burn is his desire.
That he may live again; he's proud in death,
And goes in haste to gain a better breath.
The spice heap fired with celestial rays
Doth burn the aged Phoenix, when straight stays
The Chariot of the amazed Moon; the pole
Resists the wheeling, swift Orbs, and the whole
Fabric of Nature at a stand remains.
Till the old bird anew, young begins again.

[Taken from: http://www.phoenixarises.com/phoenix/legends/greek.htm, 2. mars - 2005]

1. Phoebus, another name for Apollo, but also a poetic word to describe the sun

Appendix C

Data

Time and orbit number for data used to estimate the plasma sheet half thickness. The average plasma sheet half thickness and the average AE-index for each passage is shown. Number of PSBL crossing (#PS) and number of neutral sheet crossings (#NS) for each crossing is also listed. Totally 69 tail passages were used.

Orbit	Time inn			Time out		Thickness	AE-index	# PS	# NS
175	14.08.2001	14:10		15.08.2001	15:20	5,38	216,00	12	2
191	21.09.2001	07:40		22.09.2001	07:40	5,52	57,00	12	1
323	01.08.2002	15:40		02.08.2002	17:00	4,29	500,00	12	7
324	03.08.2002	16:50		05.08.2002	01:00	5,25	190,00	16	4
325	06.08.2002	07:00		07.08.2002	15:00	6,34	70,00	14	2
327	11.08.2002	07:00		12.08.2002	11:00	5,33	220,00	16	2
328	13.08.2002	12:00		14.08.2002	14:00	4,25	160,00	20	2
329	15.08.2002	16:00		17.08.2002	01:50	6,66	500,00	2	
330	18.08.2002	11:30		19.08.2002	13:50	4,56	598,00	20	2
331	20.08.2002	15:10		21.08.2002	12:00	2,38	806,00	16	2
333	25.08.2002	15:10		26.08.2002	08:40	2,79	165,00	10	2
334	27.08.2002	17:40		28.08.2002	20:00	4,63	158,00	24	4
336	01.09.2002	19:00		02.09.2002	09:20	3,29	300,00	2	
339	08.09.2002	10:40		09.09.2002	11:40	5,05	206,00	8	1
340	11.09.2002	01:40		12.09.2002	02:00	5,11	392,00	24	2
341	13.09.2002	11:10		14.09.2002	08:40	3,28	280,00	12	2
342	15.09.2002	23:00		17.09.2002	01:20	5,67	100,00	28	1
343	18.09.2002	07:00		19.09.2002	08:00	3,96	170,00	20	2
344	20.09.2002	12:00		21.09.2002	15:00	3,73	50,00	24	2
345	23.09.2002	04:00		24.09.2002	05:00	6,77	30,00	18	1
346	25.09.2002	05:00		26.09.2002	05:00	3,61	45,00	14	1
347	28.09.2002	00:00		29.09.2002	06:00	5,78	50,00	22	1
349	02.10.2002	09:00		03.10.2002	07:00	4,19	270,00	8	1
476	31.07.2003	14:00		01.08.2003	18:00	6,37	500,00	8	1
477	02.08.2003	21:00		04.08.2003	05:00	6,96	350,00	10	1
479	07.08.2003	19:00		09.08.2003	06:00	7,14	600,00	20	3
480	10.08.2003	10:00		11.08.2003	10:00	5,54	90,00	18	1
482	14.08.2003	19:10		15.08.2003	18:00	4,72	294,00	16	1
483	17.08.2003	10:50		18.08.2003	07:00	3,24	658,00	12	2
484	19.08.2003	18:00		20.08.2003	14:40	4,86	160,00	10	1
485	22.08.2003	00:30		23.08.2003	05:30	5,90	634,00	16	1
486	24.08.2003	11:50		25.08.2003	10:50	3,55	525,00	8	3
487	26.08.2003	17:40		27.08.2003	12:30	4,60	170,00	2	3
488	29.08.2003	10:50		30.08.2003	05:20	3,96	562,00	8	1
489	31.08.2003	14:30		01.09.2003	13:00	5,40	216,00	6	7
490	03.09.2003	05:10		03.09.2003	17:40	4,95	200,00	2	
493	10.09.2003	00:20		11.09.2003	08:00	6,38	215,00	36	1
494	12.09.2003	10:10		13.09.2003	05:10	2,69	248,00	24	3
495	15.09.2003	03:40		15.09.2003	12:10	3,84	50,00	2	1
496	17.09.2003	03:50		18.09.2003	07:10	5,72	640,00	20	3
497	19.09.2003	14:40		20.09.2003	08:10	3,36	681,00	16	3
498	21.09.2003	20:00		23.09.2003	02:00	6,21	280,00	26	1
499	24.09.2003	06:00		25.09.2003	07:00	4,91	550,00	22	3

630	31.07.2004	12:30		01.08.2004	15:10	7,69	200,00	6	3
631	02.08.2004	17:20		04.08.2004	02:10	7,78	90,00	6	9
632	05.08.2004	08:00		06.08.2004	07:50	5,26	115,00	14	7
633	07.08.2004	13:40		08.08.2004	10:30	3,79	90,00	12	7
634	09.08.2004	18:50		10.08.2004	16:10	3,17	500,00	16	1
635	12.08.2004	12:40		13.08.2004	05:40	5,09	140,00	10	3
636	14.08.2004	15:50		15.08.2004	12:30	2,75	120,00	16	1
638	19.08.2004	10:20		20.08.2004	05:30	4,17	170,00	12	1
640	24.08.2004	01:20		24.08.2004	22:50	4,71	85,00	12	1
641	26.08.2004	12:10		27.08.2004	10:00	3,47	110,00	14	1
642	28.08.2004	21:20		29.08.2004	17:50	5,30	90,00	22	1
643	31.08.2004	05:50		01.09.2004	07:40	5,36	300,00	18	1
644	02.09.2004	12:30		03.09.2004	11:50	4,39	70,00	14	-
648	12.09.2004	08:50		12.09.2004	22:00	3,26	70,00	6	-
649	14.09.2004	11:20		15.09.2004	09:10	3,39	670,00	16	-
650	16.09.2004	16:10		17.09.2004	12:20	3,46	360,00	16	-
651	19.09.2004	09:20		19.09.2004	22:10	3,30	200,00	16	-
652	21.09.2004	18:10		22.09.2004	11:30	4,77	50,00	16	-
653	24.09.2004	00:20		24.09.2004	15:30	4,89	190,00	18	-
654	26.09.2004	09:10		27.09.2004	08:50	4,19	15,00	14	-
655	28.09.2004	23:00		29.09.2004	09:50	2,64	20,00	8	-
656	01.10.2004	07:30		01.10.2004	19:20	4,94	20,00	6	-

Appendix D

Source Code

MatLab source codes that were developed and used in this thesis is included here:

Cluster_main - Main program that reads the data files, prepare data and call functions to execute binning of data, to calculates densities and to plot the data.
Boxing - Function that take care of the binning of data.
Plotdata_xy - Transform data into plasma densities, create 2D plots out of a 3D matrix. Similar function for plotting in the xz- and yz-plane was also used.
Path_plot - Plots the satellite path and the density measured along it.
Corr_plot - Sort data after geomagnetic activity and x-position, calls correlation routine to calculate correlation coefficients and regression coefficients.
Correlation - Calculating correlation coefficients and regression coefficients.

```
function [] = Cluster_main();

% Main program that treats data from many days.

%%%%%%%%%%%%%%%%%%%
% Initialization %
%%%%%%%%%%%%%%%%%%%
clear all
X_max = 20;     % Max earth radii in x-direction
X_min = -20;    % Min earth radii in x-direction
Y_max = X_max;  % Max earth radii in y-direction
Y_min = X_min;  % Min earth radii in y-direction
Z_max = X_max;  % Max earth radii in z-direction
Z_min = X_min;  % Min earth radii in z-direction
N = 60;         % Number of boxes

% Find interval length
dX = ((X_max - X_min)/N);   % Size of boxes in x-direction
dY = ((Y_max - Y_min)/N);   % Size of boxes in y-direction
dZ = ((Z_max - Z_min)/N);   % Size of boxes in z-direction

% Create vectors with
% Vector containing position of boundaries in x_direction for the boxes
X_vector = [X_min:dX:X_max];
% Vector containing position of boundaries in y_direction for the boxes
Y_vector =[Y_min:dY:Y_max];
% Vector containing position of boundaries in z_direction for the boxes
Z_vector = [Z_min:dZ:Z_max];

%%%%%%%%%%%%%%%
% Read data  %
%%%%%%%%%%%%%%%
Data_potential = load CDA_potential_2003.mat %Data_potential: doy, time, V;
Data_position  = load CDA_position_2003.mat %Data_position: doy, time, #, X, Y, Z;
```

```
Data_position(find(Data_position == -1.0000e+31)) = NaN;
Data_potential(find(Data_potential == -1.0000e+31)) = NaN;

D1(:,1) = (Data_potential(:,1)*24*3600) + Data_potential(:,2); %D1: time, V;
D1(:,2) = Data_potential(:,3);  %D1: time, V;

D2(:,1) = (Data_position(:,1)*24*3600) + Data_position(:,2); %D2: time, #, X, Y, Z;
D2(:,2:5) = Data_position(:,3:6);   %D2: time, #, X, Y, Z;

% Put the two data-matrices together
A = (D1(:,1)-24*3600)/60+0.5;  %Index-vector for potential
B = (D2(:,1)-24*3600)/60+0.5;  %Index-vector for position

Data_total = zeros((366*24*60),6)+ NaN;
Data_total(round(A),1:2) = D1(:,1:2);
Data_total(round(B),[1,3:6]) = D2(:,1:5);

%Data_total: time, V, #, X, Y, Z;
Data_total = Data_total(find(~isnan(sum(Data_total,2))),:);

Data(:,1:2) = Data_total(:,1:2); % Data: time, V, X, Y, Z;
Data(:,3:5) = Data_total(:,4:6); % Data: time, V, X, Y, Z;

%%%%%%%%%%%%%%%%%%
%  Boxing data  %
%%%%%%%%%%%%%%%%%%
% Boxing data from all days
[Pot_sum, count] = Boxing(Data,X_vector,Y_vector,Z_vector,N);


function [Pot_sum,count] = Boxing (Data, X_vector, Y_vector, Z_vector, N)

% Put data into boxes and calculate the mean value for one day

% Find which box the data will fit into.
% When the correct box is found the data is added to the old value (initialized to zero)
% At last the value in each box are divided on numbers of times a value have been added.
% (mean value for each box for on day)
% If data belongs on the inner edge of the sphere, they will not be added to any boxes

% Initialize boxes
Pot_sum = zeros(N, N, N);
count = zeros(N, N, N);
no_box = 0;

for i = 1:(length(X_vector)-1)
   for j = 1:(length(Y_vector)-1)
      for k= 1:(length(Z_vector)-1)
         line_nr = find( ( (Data(:,3)> X_vector(i) & Data(:,3) < X_vector(i+1)) &...
                     (Data(:,4)> Y_vector(j) & Data(:,4) < Y_vector(j+1)) ) &...
                     (Data(:,5)> Z_vector(k) & Data(:,5) < Z_vector(k+1))    );
         if isempty(line_nr)
            no_box = no_box + 1;
            Pot_sum(i,j,k) = 0;
            count(i,j,k) = 0;
         else
            Pot_sum(i,j,k) = sum(Data(line_nr,2));
            count(i,j,k) = length(line_nr);
         end
         [i j k]
      end
   end
end
```

```
function [] = Plotdata_xy(X_max, X_min, Y_max,Y_min,dX,dY, Pot_sum,count,Data)

% Plot the data in 2D (similar program for plot in xz and yz)

% Sum over all Z-position-boxes to make a 2 dimensional matrix. Calculate
% the mean value and plot this together with the satellite path, the earth
% and axis in the middle of the figure. Print the figure to file as both
% PostScript- and JPG- image
% Some difficulties with colorbar-limits because of spikes in the data which
% create higher values than expected.

% Initialize matrixes
V_sum = zeros(size(Pot_sum,1),size(Pot_sum,2));
C_sum = zeros(size(Pot_sum,1),size(Pot_sum,2));
Pot_sum(find(isnan(Pot_sum))) = 0; % puts NaN = 0

for a = 1:size(Pot_sum,3)
   A = Pot_sum(:,:,a);
   B = count(:,:,a);
   V_sum = V_sum + A;
   C_sum = C_sum + B;
end

%Used to make a cross section through the third axis
%    g = 6;
%    h = 7;
%    i = 6;
%    j =8;
%    % Sum over all Z-position-boxes => 2 dimensions
%    index1 = find(Z_vector > g & Z_vector < h );
%    index2 = find(Z_vector > i & Z_vector < j);
%    index = [index1;index2];
%    for a = 1:length(index)
%       A = Pot_sum(:,:,index(a));
%       B = count(:,:,index(a));
%       V_sum = V_sum + A;
%       C_sum = C_sum + B;
%    end

% calculate the mean value of the potential
V = V_sum./C_sum;
% Converting to density (26.03.05)
Density = (200*exp(V/0.9))+(100*exp(V/2.1))+(2*exp(V/12));
V_mean = Density;

%%%%%%%%%%%%
% Plot data %
%%%%%%%%%%%%
figure;
% Plotting mean of SC-Potential
% Using X_min+dX/2 instead of just X_min because when plotting the boxes
% are displaced by dX/2
imagesc([(X_min+dX/2) (X_max-dX/2)],[(Y_min+dY/2) (Y_max-dY/2)],log10(V_mean)');

% Axis limit
axis([X_min, X_max, Y_min, Y_max]);
set(gca,'XDir','reverse','YDir','reverse','FontSize',25,'FontWeight', 'bold');

% Colorbar and limits
map = colormap(jet);
```

```
map(1,1:3)= [1,1,1]; % white color for data = NaN
colormap(map);
cb = colorbar;
set(cb,'FontSize', 25,'FontWeight', 'bold');

% Title and label on the axis
xlabel('X (# Re)','FontSize', 25,'FontWeight', 'bold');
ylabel('Y (# Re)','FontSize', 25,'FontWeight', 'bold');
gca;
text(1.37,.5,'Density (log)','Units','normalized','HorizontalAlignment',...
   'center','VerticalAlignment','middle','Rotation',-90, 'FontSize', 25,'FontWeight', 'bold');
hold on;

% Drawing Earth and axis in figure
t = [0:pi/200:2*pi];
T = [0:-pi/100:-pi];
x = [X_min:dX:X_max];
y = [Y_min:dY:Y_max]';
plot(sin(t),cos(t),'k'); % earth
fill(sin(T),cos(T),'k'); % night side
plot(x,zeros(size(x)),'k','LineWidth',1); % x-line
plot(zeros(size(y)),y,'k','LineWidth',1); % y-line

% Properties
axis square
grid on;
hold off;
set(gcf, 'PaperType','A4','PaperUnits', 'normalized',...
   'PaperPosition',[0 0 1 1],'PaperOrientation','landscape');

% Printing
print(gcf,'-dmeta','Density_xy.emf');



function [] = Path_Plot(Data,X_min,X_max,dX,Y_min,Y_max,dY,Z_min,Z_max,dZ)

%Plotting the spacecraft-potential along the satellite path

% Declaration of variables
T = Data(:,1); % time array
V = Data(:,2); % SC-Potential array
X = Data(:,3); % GSE_X array
Y = Data(:,4); % GSE_Y array
Z = Data(:,5); % GSE_Z array

t = [0:pi/200:2*pi]; % array to earth-plotting
T = [0:-pi/100:-pi]; % array to filling earth
x = [X_min:dX:X_max]; % Array for making axis
y = [Y_min:dY:Y_max]; % Array for making axis
z = [Z_min:dZ:Z_max]; % Array for making axis

a = -20:20/64:0; % Limits for colorbar

%%%%%%%%%%%%%%%%%%%%%%%%%%%
% Plotting xz-direction %
%%%%%%%%%%%%%%%%%%%%%%%%%%%
figure;
% Controlling scale on colorbar
fill(0,0,0);
caxis([a(1) a(end)]);
cb = colorbar;
map = colormap('jet');
```

```
hold on;
% Plotting Earth and axis
plot(sin(t),cos(t),'k'); % earth
fill(sin(T),cos(T),'k'); % night side
plot(x,zeros(size(x)),'k','LineWidth',2); % x-line
plot(zeros(size(z')),z','k','LineWidth',2); % y-line

% Plotting data lower than colorlimit_min
index = find(V<a(1));
if ~isempty(index)
   plot(X(index),Z(index),'.','MarkerFaceColor',map(1,:),'MarkerEdgeColor',map(1,:));
end
% Plotting data higher than colorlimit_max
index = find(V>a(end));
if ~isempty(index)
   plot(X(index),Z(index),'.','MarkerFaceColor',map(end,:),'MarkerEdgeColor',map(end,:));
end
% Plotting all other data
for i = 1:length(map)
   index = find(V>=a(i) & V<a(i+1));
   if ~isempty(index)
      plot(X(index),Z(index),'.','MarkerFaceColor',map(i,:),'MarkerEdgeColor',map(i,:));
   end
end

% Axis properties
set(gca,'XDir','reverse','YDir','normal');
text(1.3,0.5,'Volts','Units','normalized','HorizontalAlignment',...
   'center','VerticalAlignment','middle','Rotation',-90, 'FontSize', 12);
xlabel('X (# R_E)', 'FontSize', 12);
ylabel('Z (# R_E)', 'FontSize', 12);
axis square
grid on;
hold off;
set(gcf, 'PaperType','A4','PaperUnits', 'normalized');


function [] = Corr_plot(Tja)

% Removing data more than 2 standard deviations from the mean value
tja = Tja(:,3)-Tja(:,1);
var_lim = round(nanmean(tja)+(2*nanstd(tja)))
Tja(find(tja > var_lim),2) = NaN;

% sorting data after high and low activity
T1 = T(high,:);
T2 = T(low,:);
P1 = Tja(high,2);
P2 = Tja(low,2);

%Sorting high activity data after x-position
a1 = find(T1(:,2)<= -17);
hm = find(T1(:,2)<= -15);
b1 = hm(find(T1(hm,2)> -17));
c1 = find(T1(:,2)> -15);

%Sorting low activity data after x-position
a2 = find(T2(:,2)<= -17);
hm = find(T2(:,2)<= -15);
b2 = hm(find(T2(hm,2)> -17));
c2 = find(T2(:,2)> -15);
```

```
% Finding correlation and regression coefficients
[rxya1,aa1,ba1,resa1,pa1] = correlation(T1(a1,1),P1(a1));
[rxyb1,ab1,bb1,resb1,pb1] = correlation(T1(b1,1),P1(b1));
[rxya2,aa2,ba2,resa2,pa2] = correlation(T2(a2,1),P2(a2));
[rxyb2,ab2,bb2,resb2,pb2] = correlation(T2(b2,1),P2(b2));
[rxy1,AA1,BB1,res1,p1] = correlation(T1(:,1),P1);
[rxy2,AA2,BB2,res2,p2] = correlation(T2(:,1),P2);

% Calculating regression line
ya1 = aa1 + (ba1*T1(a1,1));
yb1 = ab1 + (bb1*T1(b1,1));
ya2 = aa2 + (ba2*T2(a2,1));
yb2 = ab2 + (bb2*T2(b2,1));
y1 = AA1 + (BB1*T1(:,1));
y2 = AA2 + (BB2*T2(:,1));

% Plotting
figure
hold on
%plot(T1(a1,1),P1(a1),'*r','MarkerSize',25) % High activity , 17-19
%plot(T1(b1,1),P1(b1),'+b','MarkerSize',25) % High activity , 15-17
plot(T2(a2,1),P2(a2),'*r','MarkerSize',25) % Low activity , 17-19
plot(T2(b2,1),P2(b2),'+b','MarkerSize',25) % Low activity , 15-17
%plot(T1(:,1),y1,'-k','LineWidth',5) % Regression line, High activity
plot(T2(:,1),y2,'-k','LineWidth',5) % Regression line, Low activity

hold off
l = legend('[-17 -19]Re','[-15 -17]Re',1);
set(l,'FontSize', 20,'FontWeight','bold')
xlabel('Half thickness (R_e)','Fontsize',25,'FontWeight','bold');
ylabel('Pressure_{sw} (nPa)','Fontsize',25,'FontWeight','bold');
set(gca,'XLim',[0 12],'FontSize', 25,'FontWeight','bold')
set(gcf, 'PaperPositionMode', 'manual', 'PaperType','A4',...
    'PaperOrientation','landscape','PaperUnits','normalized',...
   'PaperPosition',[.4 .7 1 1]);

print(gcf,'-dmeta','Pressure_low.emf');


function [rxy,a,b,res,pxy]  = correlation(x,y)

% Regression coefficients
X = [ones(length(x),1) x];
[B,Bint,R,Rint,Stats]  = regress(y,X);

a = B(1); % gradient
b = B(2); % interception point
res = R; % residuals

% Correlation
te = isnan(x);
x1 = x(~te);
y1 = y(~te);
te = isnan(y1);
x2 = x1(~te);
y2 = y1(~te);
[r,p] = corrcoef([x2, y2]);

rxy = r(2,1); % correlation coefficient
pxy = p(2,1);
clear te x1 x2 y1 y2 r
```